QSIT Quantum Science and Technology

National Centre of Competence in Research

NCCR QSIT Junior Meeting 2016

Passugg, 13-15 June, 2016

FNSNF

Swiss National Science Foundation

Contact

Robin D. Buijs
ETH Zürich
Institute for Solid State Physics
Tel.: +41 44 633 31 16
E-Mail: robindbuijs@phys.ethz.ch

Andreas Landig
ETH Zürich
Institute for Solid State Physics
Tel.: +41 44 633 77 10
E-Mail: alandig@phys.ethz.ch

Cover image: With kind permission of Chur Tourismus (www.churtourismus.ch)

Contents

1 Programme

QSIT's Junior Meeting is an opportunity for junior scientists to try their hand at presenting a scientific topic and get familiar with the various QSIT groups and their work. The meeting primarily targets doctoral students before their first publication, who have most to gain from it.

Each participant is scheduled for an introductory talk on their research project. More in-depth discussion is possible between the sessions and during the poster session. In addition, the meeting stimulates less formal discussions during the social events on Tuesday afternoon and evening.

	13.06.2016	14.06.2016	15.06.2016
8:00		**Breakfast**	**Breakfast**
9:00		Martin Buchacek	Lujun Wang
9:20		Marc-Dominik Kraß	Ephanielle Verbanis
9:40		Martin Héritier	Kilian Sandholzer
10:00		Maciej Malinowski	Misael Caloz
10:20		**Coffee break**	**Coffee break**
10:50		Jean-Claude Besse	Christopher Mittag
11:10		Elisa Bäumer	Kevin Roux
11:30		Luca Alt	Marc-Olivier Renou
11:50		Chi Zhang	Thibaud Ruelle
12:15	**Arrival/Lunch**	**Lunch**	**Lunch**
13:20	**Registration/Welcome**		
13:30			Robin Oswald
13:50	Oliver Wipfli		Jonas Roch
14:10	Christoph Fischer		Johannes Kölbl
14:30	Riccardo Pisoni	**Rope park / Hike**	Tomislav Damjanovic
		or	
14:50	**Coffee break**	**Brewery / Bouldering**	**Coffee break**
15:20	Jan Scharnetzky	**City Tour**	Simon Ragg
15:40	Alberto Boaron		Matthias Löbl
16:00	Gianni Buser		Rozenn Diehl
16:20	Nikolaus Flöry		Closing remarks
16:30			**Departure**
17:30	**Dinner**		
19:30	**Poster Session**	**Conference dinner**	

2 Abstracts

Optically Trapping Ions in a Build-Up Cavity: Controlling the Ion-Ion Spacing

O. Wipfli,[1] C. Fischer,[1] M. Marinelli,[1] M. Grau,[1] and J. P. Home[1]

[1] *Institute of Quantum Electronics, ETH-Hönggerberg, CH-8093, Zürich, Switzerland*

We are building an experiment that traps ions in an optical lattice created by the strong light field of an optical build-up cavity. While the trapping lattice has a period of half an optical wavelength $\lambda/2 = 266\,\mathrm{nm}$, the ions will only sparsely populate the lattice at an ion-ion spacing $d_{\mathrm{ion-ion}} \gg \lambda/2$, which enables site resolved quantum state manipulation. In this talk I will present two possible methods to control the ion-ion spacing. They are based on position-selective transfer of atoms to an unconfined electronic state, which removes unwanted atom from the lattice.

I. INTRODUCTION

The dynamics of many-body quantum systems are often too difficult to solve with analytical calculations and simulating them on a classical computer would often take too long because of the exponential growth of the Hilbert space in system size. Quantum simulation is an alternative approach to solving such problems. The idea is to use a well controllable quantum many-body system to mimic the dynamics of some other system of interest. For example trapped ions were used to simulate the dynamics of the transverse Ising model[1].

While trapped ions are an ideal candidate for many-body quantum simulation there are major technical difficulties associated with the way they are conventionally confined. In radio frequency Paul traps, ions that are not located exactly in a pseudo-potential minimum will experience micromotion[2]. Also the motional mode density increases the more ions occupy the same trap so that addressing motional states becomes harder.

To overcome the scaling limitations of radio frequency Paul traps we are working on a new experiment that confines ions purely optically. Two mirrors will be used to form an optical Fabry-Perot cavity. In the cavity a standing wave light field creates an optical lattice that will trap ions based on AC Stark shifting of electronic states. A single cavity will form a one dimensional optical lattice. Higher dimensional lattice geometries are accessed by crossing two or three cavities. The chosen atomic species for this experiment is ^{25}Mg because both the ground state of the neutral atom and the ion can be optically trapped with 532 nm light[3].

While the trapping lattice has a period corresponding to half an optical wavelength ($\lambda/2 = 266\,\mathrm{nm}$), ions would not be confined at such a short spacing because Coulomb repulsion dominates over the trapping forces. We expect a lattice depth of 400 mK for a cavity finesse of 10000 and an input light power of 8 W. With these parameters a stable lattice is realized when the ion-ion distance is 7 μm or more according to our simulations. Imaging ions with such a separation on the ^{1}S to ^{1}P transition at 280 nm wavelength will be site resolved already if we use an imaging system with a moderate numerical aperture of 0.4. Thanks to the large ion separation we will not only be able to image site by site but also focused laser beams can manipulate ion by ion. This experiment will lead to a many-body quantum simulator with the ability to image, address, and manipulate each ion individually.

Initially the lattice will be completely filled with neutral atoms. The first step is to prepare the lattice such that atoms are only on sites separated by the ion-ion distance (Figure 1b). Here, we present two possible methods that can be used to control the filling of the lattice.

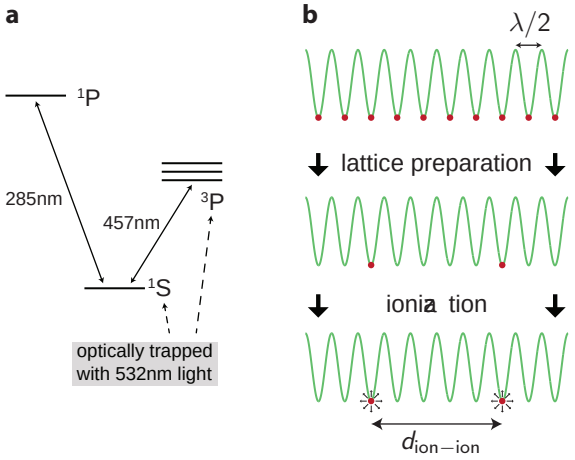

FIG. 1: **a** Level diagram of ^{25}Mg. The ^{1}P state is not optically trapped by 532 nm light. **b** Initially neutral atoms are trapped in the optical lattice with a spacing of $\lambda/2 = 266\,\mathrm{nm}$. For typical lattice well depths, the strength of the Coulomb force prevents ions from being closer than 7 μm. Preparing a stable population of ions in the optical lattice requires first spacing the neutral atoms by $d_{\mathrm{ion-ion}} \gg \lambda/2$ before ionizing.

II. LATTICE PREPARATION METHODS

The basic working principle of the two lattice preparation methods is that atoms are position-selectively transferred to the ^{1}P state, which is not confined optically (Figure 1a). Atoms in this state experience a repulsive force and are ejected from the lattice. In order to remove the unwanted atoms, first all atoms are placed in the ^{1}S state and the following three operations are performed:

1. Apply a spatially varying differential energy shift to the ^{3}P and ^{1}S states. The transition between

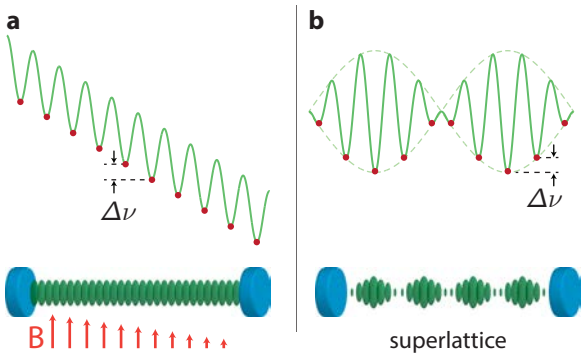

FIG. 2: Two possible lattice preparation methods. **a** A magnetic field gradient creates a spatially varying Zeeman shift. If the splitting between neighbouring sites $\Delta\nu$ becomes larger than the width of a narrow atomic transition, sites can be individually addressed by changing the laser frequency. **b** The beat note pattern of two laser wavelengths creates a superlattice. This results in a potential where the longer period corresponds to the target ion-ion spacing $d_{\mathrm{ion-ion}}$. Again, the splitting between neighbouring sites has to be larger than the atomic transition linewidth and the laser linewidth.

these states has a wavelength of $\lambda = 457\,\mathrm{nm}$ and a natural linewidth of $\Gamma/2\pi = 40\,\mathrm{Hz}$.

2. The desired atoms are then transferred from the ground ^{1}S state to the $^3\mathrm{P}_1$ state. This state is optically trapped and has a lifetime of 4 ms.

3. The remaining unwanted atoms in the ground state are transferred to the untrapped ^{1}P state using 285 nm laser light.

In the first method the frequency of the 457 nm transition between the ^{1}S and ^{3}P state is changed depending on position by applying a magnetic field gradient along the cavity axis (Figure 2a). The magnetic field creates a spatially varying Zeeman shift. In order to use the laser frequency to resolve adjacent lattice sites, the Zeeman shift between sites $\Delta\nu$ must be larger than the transition linewidth. Moreover, the laser that drives this transition has to be narrower than the frequency separation between neighbouring sites, which can be achieved by filtering the 457 nm laser light with a narrow-band cavity. With an acusto-optical modulator the frequency of the laser can be tuned to be resonant with a certain site which pumps its population to the $^3\mathrm{P}_1$ state. The laser frequency can then be abruptly changed such that it is resonant with atoms in a well at the target ion-ion distance. Iterating this along the cavity axis will lead to the desired lattice filling.

The second possible method to prepare the lattice is based on a dual color superlattice (Figure 2b). Here, the cavity inhabits two standing wave light fields at two different wavelengths. From both fields the atoms will experience an AC Stark shift, and if the relative intensities are appropriately tuned, the total potential landscape will be a beat note pattern where the long-period corresponds to the target ion-ion spacing $d_{\mathrm{ion-ion}}$. As before a narrow-band 457 nm laser is now used to transfer atoms in the target sites, i.e. the sites with the deepest trapping potential, to the ^{3}P state.

III. OUTLOOK

We are working on a new experiment that traps ions with optical forces. Ions will be spaced by several micrometers in a standing wave light field of an optical cavity, which is key to prepare, manipulate, and measure the quantum state of each individual ion in the lattice. It is still an open question how the ion-ion spacing will be controlled, but here we present two methods that have the potential to solve this issue. A first method is based on a magnetic field gradient, and a second uses a superlattice potential created by two intracavity fields. While both methods are in principle feasible, the decision which one to choose will include estimating the technical efforts and costs that each one involves.

Acknowledgments

This project is founded by a Consolidator Grant of the Swiss National Science Foundation.

[1] K. Kim, S. Korenblit, R. Islam, E. E. Edwards, M.-S. Chang, C. Noh, H. Carmichael, G.-D. Lin, L.-M. Duan, C. C. J. Wang, et al., *Quantum simulation of the transverse ising model with trapped ions*, New Journal of Physics **13**, 105003 (2011).

[2] D. J. Berkeland, J. D. Miller, J. C. Bergquist, W. M. Itano, and D. J. Wineland, *Minimization of ion micromotion in a paul trap*, Journal of Applied Physics **83**, 5025 (1998).

[3] M. Marinelli, *Master thesis: High finesse cavity for optical trapping of ions* (2014).

Optical trapping of ions

Christoph Fischer,[1] Oliver Wipfli,[1] Matteo Marinelli,[1] Matthew Grau,[1] and Jonathan P. Home[1]
[1]*Institute of Quantum Electronics, ETH-Hönggerberg, CH-8093, Zürich, Switzerland*

We propose an experiment for trapping magnesium ions in a far off-resonant optical without the use of any radio-frequency fields. This setup will not only allow dissipative and coherent manipulation of the electronic and motional states of the ions, it also naturally offers scalability in two and three dimensions. Here we present our reasoning for choosing magnesium as our atomic species and show how cold ions can be prepared in a high finesse build-up cavity.

I. INTRODUCTION

One of the major challenges of simulating quantum systems using ions is the scalability of the trap structure. Linear Paul traps can confine ions only in one-dimensional strings and micro-structured potentials generated by two-dimensional arrays of rf electrodes are difficult to fabricate using lithographic techniques. On the other hand, two- and three-dimensional lattices based on optical potentials are widely used in neutral atom experiments[1].

Recent work has shown that trapping of ions in tightly focused, far off-resonant beams is possible[2] but the lifetime of the trap was limited to several milliseconds due to scattering of lattice photons.

The purpose of our new experiment is to trap arrays of $^{25}Mg^{+}$ ions in a far off-resonant optical lattice which will enable us to simulate the dynamics of strongly interacting quantum systems in two-dimensions. By carefully selecting our atomic species we will be able to cool and coherently manipulate the ions while they are confined by optical potentials only. The use of a ultra-high vacuum (UHV) system will us further allow lifetimes of several minutes, mainly limited by collisions with residual background atoms[3].

This paper focuses on the choice of magnesium as our atomic species and the experimental apparatus required to prepare cold atoms in a deep optical trap. In sec. II the theory of optical dipole trapping (ODT) is reviewed and we argue why ^{25}Mg is an ideal atomic species for our experiment and sec. III gives an overview of the experimental setup as well as an outlook on the further steps.

II. MAGNESIUM IN AN OPTICAL FIELD

The interaction of a two-level atom with a far-detuned laser can be treated as a second-order perturbation of the energy levels[1]

$$\Delta E = \pm \frac{3\pi c^2}{2\omega_0^3}\frac{\Gamma}{\Delta} I(r,z), \tag{1}$$

where the positive sign corresponds to the shift of the ground state. Here ω_0 is the unperturbed splitting between the states, Γ denotes the spontaneous emission rate and $\Delta = \omega_0 - \omega_L$ is the detuning between the atomic transition and the laser with intensity

$$I(r,z) = \frac{2P}{\pi w^2(z)} \exp\left(-2\frac{r^2}{w^2(z)}\right). \tag{2}$$

For a negative (red) detuning of the laser the ground state experiences a negative shift while the upper level is shifted upwards by the same amount. The Gaussian intensity profile of the laser beam thus leads to a confining potential well for the ground state, centered at the focus of the laser. Since the ratio of trap depth and photon scattering is[1]

$$\frac{U_{\mathrm{dip}}}{\Gamma_{\mathrm{sc}}} = \frac{\Delta}{\hbar\Gamma}, \tag{3}$$

a large detuning is preferable in order to reduce photon recoil heating.

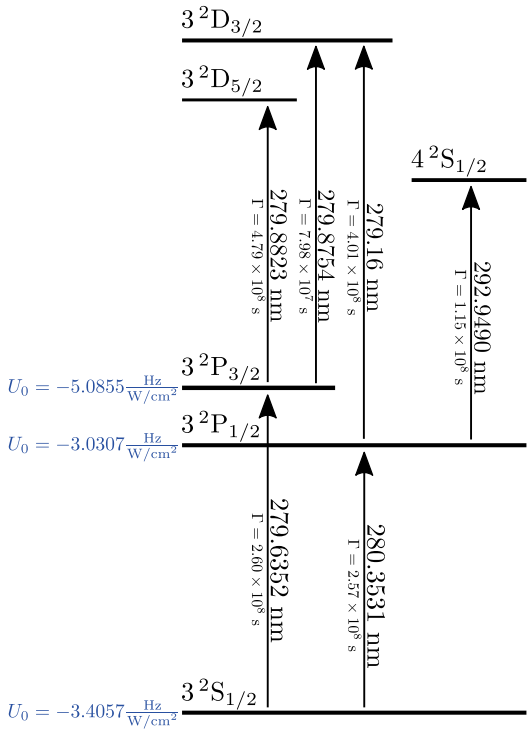

FIG. 1: Reduced energy level diagram of $^{24}Mg^{+}$. Light shifts are given for a dipole trap laser wavelength of $\lambda = 532\,\mathrm{nm}$. The scattering rate is $1.7 \times 10^{-5}\,\mathrm{s}^{-1}$ for the ground state.

In the case of real atoms light shifts due to all transitions have to be considered and an effective shift for each

energy level can be derived. In the case of the Mg^+ ion this leads to an interesting situation. As shown in fig. 1 not only the $3\,^2S_{1/2}$ ground state experiences a negative shift, also the two P states are pushed down by a laser at a wavelength of $\lambda = 532\,\mathrm{nm}$. This effect is caused by the transitions to the $3\,^2D$ levels which are also red detuned with respect to the trapping laser and overcompensate the positive shift arising the ground state.

Therefore we will be able to drive laser-induced transitions between the $3\,^2S_{1/2}$ and $3\,^2P_{3/2}$ states which can be used for cooling the ion to its motional ground state in the optical potential. Furthermore, the use of the fermionic isotope $^{25}Mg^+$ allows coherent operations between long-lived states in the hyperfine manifold of the ground state required for quantum simulation and quantum information experiments.

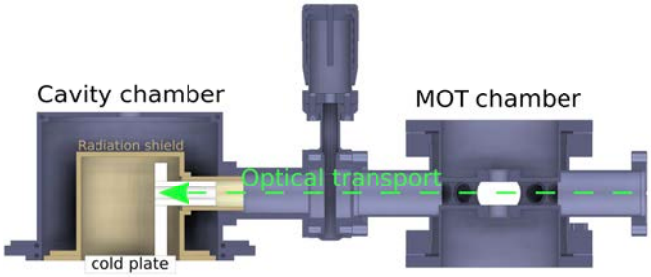

FIG. 2: Schematic view of the experimental setup. Atoms are prepared in the MOT chamber and then transfered into a cryostat where they are loaded into an optical lattice.

III. EXPERIMENT

The planned setup, depicted in fig. 2, will consist of two vacuum chambers. In the first an isotope selective magneto-optical trap (MOT) will serve as a reservoir of cold ^{25}Mg atoms. These will be shuttled into the science chamber containing where they are loaded into an optical lattice. The setup aims to maintain ultra-high vacuum throughout the experiment and operation of the science chamber at cryogenic temperatures will be desirable to reduce background gas collisions[3]. To increase the depth of the optical potential and thereby reduce the ion-ion spacing, a build-up cavity will be used, allowing for intra-cavity power of several kilowatts.

Transport of atoms between the two chambers is achieved in a running-wave dipole trap. Changing the focus of the trapping laser using a focus-tunable lens will allow us to continuously shift the trap center while heating and losses are kept at a minimum[4].

Loading magnesium atoms from a MOT into a dipole trap has been demonstrated[5] and is limited by the Doppler-temperature T_D of the MOT. If thermal equilibrium is reached, the number of atoms trapped in the dipole trap can be estimated by calculating the overlap of the traps in phase-space[6]

$$N_T = \pi^{3/2} w_0^2 R n_0 q \int_0^1 \ln(v)\,[1 - \exp(qv)]\,\mathrm{d}v. \qquad (4)$$

For typical magnesium MOT parameters[7] (peak density $n_0 = 1.8 \times 10^{10}\,\mathrm{cm}^{-3}$, MOT radius $R = 0.1\,\mathrm{mm}$) approximately $N_T \approx 150$ atoms can be loaded, assuming a relative trap depth of $q = U_0/k_B T_D \approx 0.75$ and a waist of the dipole trap of $w_0 = 10\,\mu m$.

For first experiments the number of trapped atoms is sufficient and could be increased by using a second cooling stage[5] and an optimized loading process[8].

Overlapping the transport trap with the optical mode of the build-up cavity will allow us to load the final trap. By using a site-resolved, near-resonant two-photon ionization, excess kinetic energy will be reduced and correct ion-ion spacing can be ensured.

Acknowledgments

We acknowledge support from the Swiss National Science Foundation.

[1] R. Grimm, M. Weidemüller, and Y. B. Ovchinnikov, *Optical dipole traps for neutral atoms*, Adv. At., Mol., Opt. Phys. **42**, 95 (1999).

[2] T. Huber, A. Lambrecht, J. Schmidt, L. Karpa, and T. Schätz, *A far-off-resonance optical trap for a Ba+ ion.*, Nat. Commun. **5**, 5587 (2014).

[3] K. M. O'Hara, S. R. Granade, M. E. Gehm, T. A. Savard, S. Bali, C. Freed, and J. E. Thomas, *Ultrastable CO2 laser trapping of lithium fermions*, Phys. Rev. Lett. **82**, 4204 (1999).

[4] J. Léonard, M. Lee, A. Morales, T. M. Karg, T. Esslinger, and T. Donner, *Optical transport and manipulation of an ultracold atomic cloud using focus-tunable lenses*, New J. Phys. **16**, 093028 (2014).

[5] M. Riedmann, H. Kelkar, T. Wübbena, A. Pape, A. Kulosa, K. Zipfel, D. Fim, S. Rühmann, J. Friebe, W. Ertmer, et al., *Beating the density limit by continuously loading a dipole trap from millikelvin-hot magnesium atoms*, Physical Review A - Atomic, Molecular, and Optical Physics **86**, 043416 (2012).

[6] K. M. O'Hara, S. R. Granade, M. E. Gehm, and J. E. Thomas, *Loading dynamics of CO2 laser traps*, Phys. Rev. A **63**, 1 (2001).

[7] F. Y. Loo, A. Brusch, S. Sauge, M. Allegrini, E. Arimondo, N. Andersen, and J. W. Thomsen, *Investigations of a two-level atom in a magneto-optical trap using magnesium*, J. Opt. B, Quantum Semiclassical Opt. **6**, 81 (2004).

[8] M. S. Hamilton, A. R. Gorges, and J. L. Roberts, *Influence of optical molasses in loading a shallow optical trap*, Phys. Rev. A **79**, 1 (2009), 0811.0410.

Tunneling Spectroscopy of Andreev states in Graphene

Riccardo Pisoni,[1] Joel I-J. Wang,[2] Landry Bretheau,[2] Kenji Watanabe,[3] Takashi Taniguchi,[3] and Pablo Jarillo-Herrero[2]

[1]*Solid State Physics Laboratory, ETH-Hönggerberg, CH-8093, Zürich, Switzerland*
[2]*Department of Physics, Massachusetts Institute of Technology, Cambridge, Massachusetts 02138, USA*
[3]*Advanced Materials Laboratory, National Institute for Materials Science, 1-1 Namiki, Tsukuba 305-0044, Japan*

We have performed tunneling spectroscopy of graphene connected to two superconducting electrodes, in a SQUID geometry that enables us to vary the phase difference between the order parameters of the two superconductors. The measured energy spectra are consistent with a continuum of Andreev bound states modulating with phase with energies smaller than the superconducting gap. Interestingly, out of gap modulation is also observed and can be interpreted as Andreev scattering states.

I. INTRODUCTION

Although not intrinsically superconducting, graphene (G) can inherit electronic properties of a superconductor (S) placed in good contact with it[1]. This proximity effect originates from the formation in the graphene of entangled electron-hole states, the Andreev states[2]. In an S-G-S geometry, the Andreev states energies depend on the difference between the order parameter phases of the two superconductors. Such a phenomenon is usually probed by measuring the dissipationless Josephson supercurrent carried by Andreev states[3]. Here instead, we have performed a direct tunneling spectroscopy of graphene connected to two superconducting electrodes, in a SQUID geometry that enables us to vary the phase difference[4]. Tunneling spectroscopy is a powerful tool to study the electronic properties of materials, as it has the capability of probing the electronic density of states at energies away from the Fermi level (FIG 1 **(a)**).

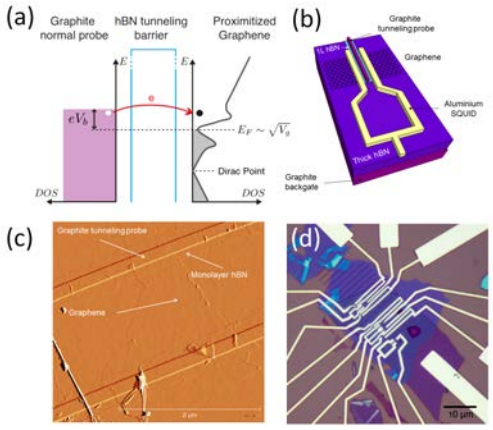

FIG. 1: **(a)** Electron tunneling. Density of states is plotted horizontally vs. energy vertically. **(b)** Sketch of the device. **(c)** AFM (amplitude signal) of the two junctions that we mostly investigated, before Al-contact evaporation. **(d)** Optical image of the device.

II. EXPERIMENT

In order to perform tunneling spectroscopy of proximitized graphene, we fabricated, by means of a polymer-based dry pick-up and transfer technique[5], a full Van der Waals heterostructure. The device, shown in FIG.1, is made of, from top to bottom, graphite tunneling probe/monolayer hexagonal Boron Nitride (hBN)/monolayer graphene/hBN substrate/graphite backgate on a SiO_2 substrate. The ultra thin hBN acts as both a tunneling barrier and an encapsulation overlayer to protect the graphene from polymer residues coming from the nanofabrication process. The graphene gets proximitized by evaporating aluminium superconducting leads, in the shape of a SQUID, directly in contact with the graphene flake. All the measurements are carried in a cryo-free dilution refrigerator at a base temperature of 20 mK. FIG 2 **(b)** shows the differential conductance as a function of the bias voltage (V_b), at a constant gate voltage (V_g). It exhibits an induced BCS-like DOS in graphene. From the position of the two divergences, one can extract a gap of 168 μeV, which is in good agreement with the Aluminium superconducting gap ($\sim$180 μeV). When varying the magnetic field, the DOS varies, as shown by the different colors in FIG 2 **(b)**. FIG 2 **(a)** presents the DOS as a function of both V_b and B, displaying a periodic ($\sim$350 μT) oscillation with the magnetic field. By evaluating the surface of the SQUID loop we extract that the modulation is periodic in unit of the magnetic flux quantum. We therefore observe a continuum of Andreev Bound States (ABS) modulating altogether with phase. This can be qualitatively understood with the presence of lots of conduction channels, having different coupling to the superconducting leads. FIG 2 **(c)** displays a larger magnetic field range. At high magnetic field one can observe that the modulation of the superconducting gap becomes blurred. As the magnetic field increases, more magnetic flux quanta are enclosed in the superconducting loop, and a finite phase gradient develops in the graphene. Therefore the ABS *feel* different phase differences across the weak link, and destructive interferences blur the superconducting gap modulation.

FIG 3 **(a)** shows that for certain gate voltage values, we observe out of gap oscillations. These oscillations are

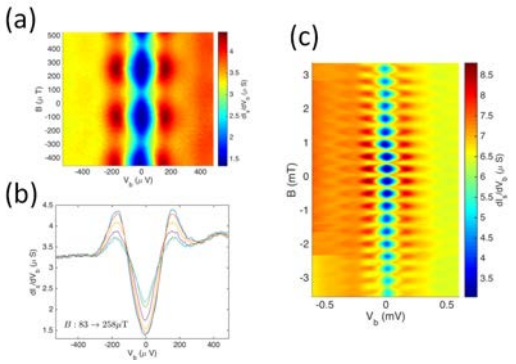

FIG. 2: **(a)** dI_s/dV_b, proportional to the DOS, modulated as a function of the applied magnetic field, measured at V_g=0.89V. **(b)** Line-cuts, covering a period of the modulation, of the dI_s/dV_b colormap shown in **(a)** . **(c)** dI_s/dV_b colormap measured as a function of B and V_b at V_g=2.4V. At high magnetic field the phase gradient in graphene blurs the induced superconducting gap.

more visible when we subtract the average signal along one of the axis (FIG 3 **(b)**). We believe this signal is related to Andreev scattering states. As sketched in FIG 3 **(c)**, it is indeed possible to form Andreev states at energies larger than the superconducting gap. The Andreev reflection amplitude is still finite for energies above the superconducting gap (FIG 3 **(d)**). To our knowledge, this is the first experimental proof of the existence of Andreev scattering states. To conclude, we observed that graphene gets proximitized by the neighboring superconductors, with the formation of a continuum of ABS. We therefore observe Andreev scattering states that, together with the ABS, are responsible for carrying the supercurrent in a non superconducting material such as graphene.

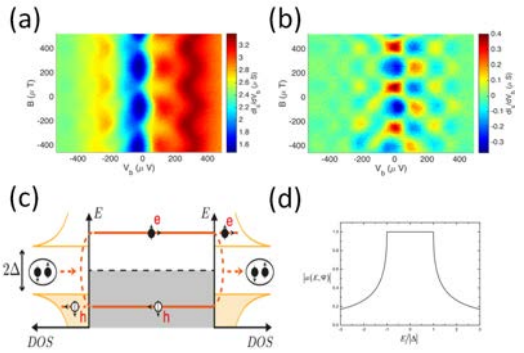

FIG. 3: **(a)** Andreev states above the superconducting gap. dI_s/dV_b measured as a function of B and V_b at V_g=0.41V. **(b)** Subtracted signal. **(c)** At energies above the superconducting gap, the electron or hole composing the Andreev bound state has a finite probability of escaping from the junction by transmitting over the superconducting gap. **(d)** Amplitude of the Andreev reflection probability.

III. OUTLOOK

In May 2016 I joined Prof. Ensslin's group at ETH. The project will focus on a different topic compared to what I worked on at MIT. I will not strictly deal with graphene anymore but with 2D TMDCs. The final goal is to develop quantum dots for quantum computing applications.

[1] P. G. De Gennes, *Boundary effects in superconductors*, Reviews of Modern Physics (1964).

[2] A. F. Andreev, *Thermal conductivity of the intermediate state of superconductors*, Soviet Physics Jetp (1965).

[3] B. D. Josephson, *Possible new effects in superconductive tunnelling*, Physics Letters (1962).

[4] J.-D. Pillet, *Andreev bound states in supercurrent-carrying carbon nanotubes revealed*, Nature Physics (2010).

[5] J. I.-J. Wang, *Electronic transport of encapsulated graphene and wse2 devices fabricated by pick-up of prepatterned hbn*, Nano Letters (2015).

Structured back-gates for high mobility two-dimensional electron systems in III-V semiconductor heterostructures

Jan Scharnetzky,[1] Matthias Berl,[1] Lars Tiemann,[1] and Werner Wegscheider[1]

[1] *Solid State Physics Laboratory, ETH Zurich, CH-8093, Zürich, Switzerland*

Ion implanted back gates were recently introduced by our group for high mobility applications. We showed that the quality of the two dimensional electron system is not affected during processing. After giving a short explanation on the fabrication of the ion implanted back gates, we will give an outlook on recent experiments and possible applications for the back gate structures.

I. INTRODUCTION

Gating of semiconductor heterostructures allows to control the charge carrier density of a two-dimensional electron/hole system. Structured gates are used to locally modify the charge carrier density which is essential for many experiments. While the fabrication of top gates by standard photo-lithography and metal evaporation is relatively straight forward, various attempts have been made to fabricate reliable back gates. Thinning the wafer and evaporating metal on the backside is one tested technique[1]. Drawbacks are the large distance between gate and 2DES and the very thin samples which are difficult to handle. Another technique uses etching of a gate into the GaAs surface before epitaxial growth of the heterostructure, reducing the distance between gate and sample[2]. However, the quality of the 2DES was drastically reduced by the surface roughness, not allowing high mobility 2DES.
The technique recently introduced for high mobility 2D electron systems by our group[3] uses standard photolithography and ion implantation to create insulating regions in a n-doped layer of gallium arsenide.
Ion implantation, the backbone of silicon based technology[4], is used to introduce n- and p-type dopants into semiconductors. Activation of the dopants and defect annihilation are performed by annealing. However, the conditions for defect removal vary drastically for different materials. In amortized silicon, complete disorder removal can be achieved at annealing temperature of 600°C while in III-V semiconductors the temperatures can exceed 1400°C[5]. In general the defect removal and dopants activation in III-V materials is more complex due to the binary nature of the lattice[6].
This short abstract will explain in more detail the fabrication of back gates using ion implantation, followed by an outlook on future developments.

II. ION IMPLANTED BACK GATES

In Fig. 1 the process steps for the fabrication of the ion implanted back gates are shown: In the first step metal organic chemical vapour deposition (MOCVD) is used to create a 100nm thick silicon doped gallium arsenide layer. In the next steps standard photolithography and oxygen implantation are used to create insulating regions in the n-doped GaAs. Prior to the molecular beam epitaxy growth, a special cleaning process is required to remove residues from the wafer. A mesa is wet-chemically etched and the sample is then contacted as shown in the figure. The spatial separation between Ohmic contacts and patterned back gates avoid shorts, which is a common problem in planar (i.e. full area) back gates.
The creation of the insulating region in the n-doped GaAs has been done by implanting oxygen ions, without a subsequent annealing procedure. Therefore, the insulation can both result from crystal defects due to the implantation as well as from the creation of mid-bandgap states (DX centers). Knowledge of the underlying insulation mechanism would open up new opportunities for multi ion implant structures requiring annealing for dopants activation.
To investigate which effect is dominant, the oxygen implantation is compared with gallium ion implantation. The introduction of gallium ions in GaAs should only create crystal defects. A simulation of the ion range, as well as the damage along their trajectory are shown in Fig. 2. The simulation is done with the "stopping and range of ions in matter" (SRIM) tool which is based on a Monte Carlo simulation method[7]. For the oxygen implantation two different energies are used, namely 20keV and 50keV, in order to have a constant oxygen ion distribution across the silicon doped region. The damage

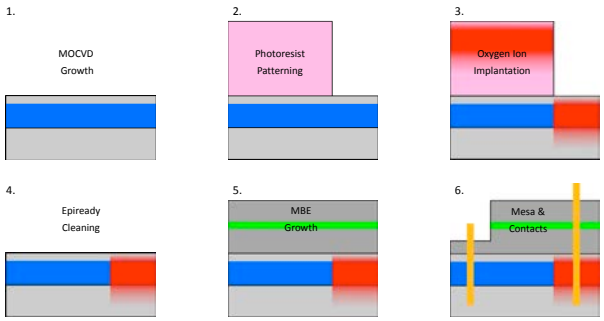

FIG. 1: The six step process to fabricate ion implanted, patterned back gates is shown. Details included in the text, figure from Ref. 6.

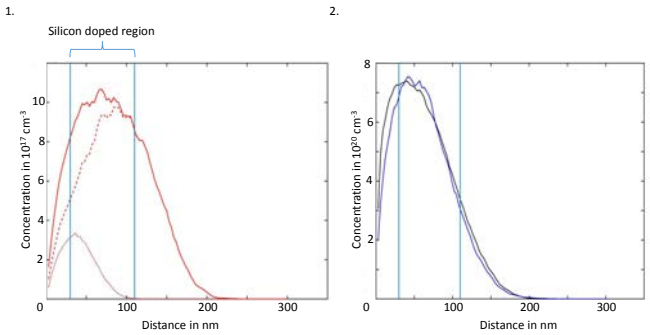

FIG. 2: Simulation of the Oxygen ion concentration (1.) and the vacancy distribution (2.). The oxygen ion implantation is simulated with $1.2 \cdot 10^{13}\mathrm{cm}^{-2}$ Ions with 50keV energy (dashed line) and $2.0 \cdot 10^{12}\mathrm{cm}^{-2}$ Ions at 20keV (dotted line). The red line indicates the two added oxygen implantations. The gallium implantation is simulated for $2.1 \cdot 10^{12}\mathrm{cm}^{-2}$ Ions at 180keV. The black line corresponds to the vacancies induced by the oxygen ion implantation, while the blue line corresponds to the vacancies induced by the gallium ion implantation.

distribution (Fig. 2.2) across the silicon doped region is very similar for both the gallium (blue line) and the oxygen implantation (black line). By comparing the conductance of the two differently implanted samples for various annealing conditions, one can determine whether the insulation is induced by physical damage or by a chemical effect of the oxygen.

III. OUTLOOK

Depending on the previous results direct implantation of donors into Gallium arsenide is planned. Activation and removal of defects during annealing may result in higher 2DES mobility after epitaxial growth compared to the usage of oxygen implantation where the defects remain in the crystal during MBE growth. Additionally, the technique will be transfered to indium/gallium antimonide.

There is a variety of applications for structured back gates: For double layer 2DES, it would be advantageous if each 2DES has a gate to control the charge carrier density without loss in quality of the 2DES from the wet-chemically etched back gates. Additionally, for any surface sensitive application, such as scanning probe microscope on III-V heterostructures back gates are required. Another application are cleaved edge overgrowth (CEO) structures where presently top gates are being used.

Acknowledgments

The authors acknowledge financial support by the Swiss National Science Foundation (SNF) and the NCCR QSIT (National Competence Center in Research Quantum Science and Technology). We thank Emilio Gini (ETH-FIRST cleanroom staff) for providing us with n-doped MOCVD substrates.

[1] J. Eisenstein, L. Pfeiffer, and K. West, *Independently contacted two-dimensional electron systems in double quantum wells*, Applied Physics Letters **57**, 2324 (1990).

[2] M. Grimshaw, D. Ritchie, J. Burroughs, and G. Jones, *Effect of the proximity of an ex situ patterned interface on the quality of two-dimensional electron gases at gaas/algaas heterojunctions*, Journal of Vacuum Science & Technology B **12**, 1290 (1994).

[3] M. Berl, L. Tiemann, W. Dietsche, H. Karl, and W. Wegscheider, *Structured back gates for high-mobility two-dimensional electron systems using oxygen ion implantation*, Applied Physics Letters **108**, 132102 (2016).

[4] Y. Nishi and R. Doering, *Handbook of semiconductor manufacturing technology* (CRC Press, 2000).

[5] J. Williams, *Ion implantation of semiconductors*, Materials Science and Engineering: A **253**, 8 (1998).

[6] S. Pearton, *Ion implantation in iii–v semiconductor technology*, International Journal of Modern Physics B **7**, 4687 (1993).

[7] J. F. Ziegler and J. P. Biersack, *Treatise on Heavy-Ion Science: Volume 6: Astrophysics, Chemistry, and Condensed Matter* (Springer US, Boston, MA, 1985), chap. The Stopping and Range of Ions in Matter, pp. 93–129.

Rapid realization of the Detector-device-independent quantum key distribution

Alberto Boaron,[1,*] Boris Korzh,[1] Raphael Houlmann,[1,2] Gianluca Boso,[1] Charles Ci Wen Lim,[3] Anthony Martin,[1] and Hugo Zbinden[1]

[1] *Group of Applied Physics (GAP), University of Geneva, Chemin de Pinchat 22, CH-1211 Geneva 4, Switzerland*
[2] *ID Quantique SA, 3 Ch. de la Marbrerie, 1227 Carouge/Geneva, Switzerland*
[3] *Quantum Information Science Group, Computational Sciences and Engineering Division, Oak Ridge National Laboratory, Oak Ridge, TN 37831-6418, US*

We present a rapid realization of the detector-device-independent quantum key distribution protocol. This protocol features improved security compared to a standard prepare and measure protocol. Our high-speed implementation allows to exchange 1 kbps of secret keys over 40 km and is still efficient at more than 90 km.

Quantum key distribution (QKD) enables the secure establishment of a random cryptographic key between two users, Alice and Bob[1]. Its security depends only on the principles of quantum physics and can be proven to be information-theoretically secure. However, one still has to be prudent about potential side-channel attacks in the practical implementation that may lead to security failures. For example, it has been shown that with detector blinding techniques, it is possible to remotely hack the measurement unit of some QKD systems[2]. Although it is possible to implement appropriate countermeasures for specific attacks, one may be wary that the adversary could devise new detector control strategies, unforeseen by the users.

To prevent all known and yet-to-be-discovered detector side-channel attacks, a measurement-device-independent QKD (mdiQKD) protocol was proposed[3]. In this scheme, Alice and Bob each randomly prepare one of the four Bennett & Brassard (BB84) states and send it to a third party, Charlie, whose role is to introduce entanglement between Alice and Bob via a Bell-state measurement (BSM). Alice and Bob do not have to trust Charlie since any other non-entangling measurement would necessarily introduce some noise between them. Unfortunately, with mdiQKD, achievable secure key rates (SKR) are significantly lower compared to conventional prepare and measure (P&M) QKD systems[4,5]. Furthermore, the technological complexity of mdiQKD is greater due to the use of two-photon interference, requiring both photons to be indistinguishable in all degrees of freedom (DOFs): temporal, polarization and frequency.

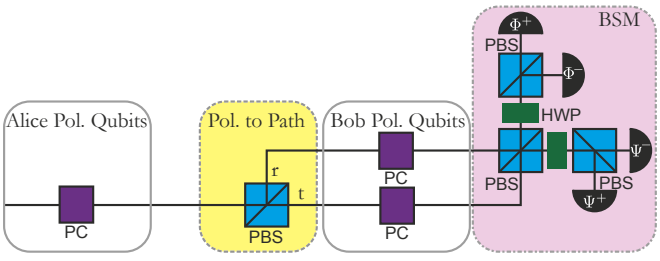

FIG. 1: Conceptual setup. PC: polarization controller; PBS: polarizing beam splitter; HWP: half-wave plate; BSM: Bell state measurement; FR: Faraday rotator.

We have recently proposed a QKD scheme that overcomes the aforementioned limitations but is still secure against detector side-channel attacks[6]. Our scheme, referred to as detector- device-independent QKD (ddiQKD), essentially follows the idea of mdiQKD, however, instead of encoding separate qubits into two independent photons, we exploit the concept of a two-qubit single-photon (TQSP). This scheme has the advantage that it requires only single-photon interference. Furthermore, it is expected that in the finite-key scenario the minimum classical post-processing size is similar to that of P&M QKD schemes.

The conceptual setup is presented in Fig. 1. Alice encodes a qubit $|\psi_A\rangle = \alpha_A \left|\tilde{H}\right\rangle + \beta_A \left|\tilde{V}\right\rangle$ in the polarization DOF of a single-photon and sends it to Bob. At the input of Bob a polarizing beam splitter (PBS) converts the polarization modes into spatial modes such that the qubit of Alice is converted to a state of the form $|\psi_A\rangle = \alpha_A |r\rangle + \beta_A |t\rangle$, where r and t represent the transmitted and reflected path of the PBS, respectively. Then, Bob encodes a qubit $|\psi_B\rangle = \alpha_B |H\rangle + \beta_B |V\rangle$ in the polarization DOF of the photon. The same polarization state needs to be encoded in the two paths. The state of the photon is then $|\psi_A\rangle \otimes |\psi_B\rangle$.

A BSM is performed by recombining the two spatial modes via a PBS and applying a projection in the basis $\{|+\rangle; |-\rangle\}$ on both output arms using two additional PBSs. $|+\rangle$ and $|-\rangle$ correspond to $\frac{|H\rangle+|V\rangle}{\sqrt{2}}$ and $\frac{|H\rangle-|V\rangle}{\sqrt{2}}$, respectively. A click in one of the four outputs corresponds to a projection into one of the following Bell states:

$$\left|\Phi^{\pm}\right\rangle = 1/\sqrt{2}\left[|r\rangle|H\rangle \pm |t\rangle|V\rangle\right] \quad (1)$$

$$\left|\Psi^{\pm}\right\rangle = 1/\sqrt{2}\left[|r\rangle|V\rangle \pm |t\rangle|H\rangle\right]. \quad (2)$$

In order to exchange secret keys, the protocol is the following. Alice and Bob independently encode states randomly chosen out of the four following BB84 states $(|H\rangle; |V\rangle; |+\rangle; |-\rangle)$. After sifting, one can not determine the bit sent by Alice only from the knowledge of which detector has clicked. Both the result of the BSM and the

Bob	$\|\Phi^+\rangle$	$\|\Phi^-\rangle$	$\|\Psi^+\rangle$	$\|\Psi^-\rangle$
H	0	0	1	1
V	1	1	0	0
+	0	1	1	0
-	1	0	0	1

TABLE I: Truth table used by Bob to extract the bit values.

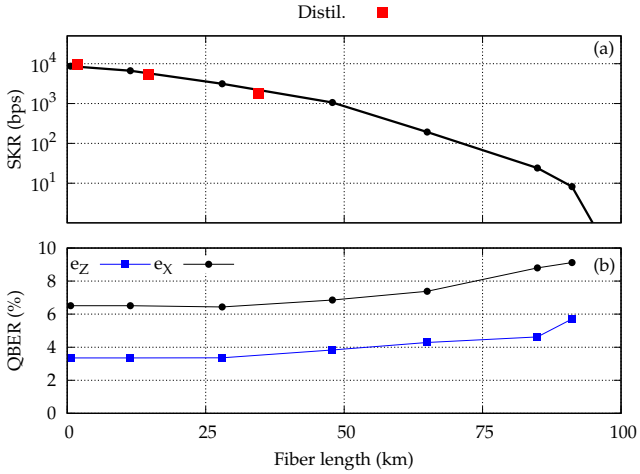

FIG. 2: (a) SKR as a function of the distance for different configurations. The red squares correspond to complete distillation of a secret key. The black curve corresponds to the SKRs measured without taking into account the finite key statistics. (b) QBER in Z and X basis as a function of the distance.

state Bob has encoded are necessary to retrieve the bit of Alice, using Tab. I. From this table, we can clearly see that knowing which detector clicks gives no information about the state encoded by Alice. Furthermore, there is no correlation between which detector clicks and the choice of Bob. Therefore, an eavesdropper cannot influence the choice of Bob by changing the detection efficiency of the detectors.

We performed an exchange of secret keys with complete distillation - i.e. including finite key analysis and privacy amplification - at three different distances simulated with a variable attenuator. The result are depicted in Tab. II. We obtained a SKR of 1.8 kbps for an attenuation of 6.8 dB corresponding to a distance of 34 km.

We also performed exchange of secret keys for additional distances without taking into account the finite key analysis. The corresponding SKRs and QBERs as a function of the attenuation (converted into fiber distance considering losses of 0.2 dB/km) between Alice and Bob are plotted in Fig. 2. We obtained a SKR of 8.2 bps at 91 km.

Attenuation [dB]	SKR [kbps]
0.28	9.7
2.8	5.3
6.8	1.8

TABLE II: SKR obtained at the output of the system after distillation of block size of 10^7 bits for different attenuations.

In summary, the ddiQKD protocol overcomes the main disadvantages of the mdiQKD protocol whilst offering an improved level of security compared to standard P&M protocols. We realized an implementation of ddiQKD using a platform capable of high speed operation in real-time using state of the art low-noise In-GaAs/InP detectors ideal for long distance QKD.

Acknowledgments

We would like to acknowledge Jesús Martínez-Mateo for providing the error correction code. We thank the Swiss NCCR QSIT and the European EMPIR MIQC2 for financial support.

* Electronic address: alberto.boaron@unige.ch

[1] C. H. Bennett and G. Brassard, *Quantum Cryptography: Public Key Distribution and Coin Tossing*, Proc. IEEE Int. Conf. Comput. Syst. Signal Process. Bangalore, India p. 175 (1984).

[2] L. Lydersen, C. Wiechers, C. Wittmann, D. Elser, J. Skaar, and V. Makarov, *Hacking commercial quantum cryptography systems by tailored bright illumination*, Nat. Photonics **4**, 686 (2010).

[3] H.-K. Lo, M. Curty, and B. Qi, *Measurement-Device-Independent Quantum Key Distribution*, Phys. Rev. Lett. **108**, 130503 (2012).

[4] N. Walenta, A. Burg, D. Caselunghe, J. Constantin, N. Gisin, O. Guinnard, R. Houlmann, P. Junod, B. Korzh, N. Kulesza, et al., *A fast and versatile quantum key distribution system with hardware key distillation and wavelength multiplexing*, New J. Phys. **16**, 013047 (2014), ISSN 1367-2630, 1309.2583, URL http://stacks.iop.org/1367-2630/16/i=1/a=013047?key=crossref.67d93c8c06267e9ca8c64b7bd7ff240e.

[5] B. Korzh, C. C. W. Lim, R. Houlmann, N. Gisin, M. J. Li, D. Nolan, B. Sanguinetti, R. Thew, and H. Zbinden, *Provably secure and practical quantum key distribution over 307 km of optical fibre*, Nat. Photonics **9**, 163 (2015).

[6] C. C. W. Lim, B. Korzh, A. Martin, F. Bussières, R. T. Thew, and H. Zbinden, *Detector-device-independent quantum key distribution*, Appl. Phys. Lett. **105**, 221112 (2014).

Dipole-trapped atoms at high optical depth for atom-light quantum interfaces

Gianni Buser,[1] Lucas Béguin,[1] Aline Faber,[1] Andreas Jöckel,[1] Thomas Karg,[1] and Philipp Treutlein[1]

[1] *Department of Physics, University of Basel, Klingelbergstrasse 82, CH-4056 Basel, Switzerland*

Far-off-resonance optical dipole traps, or FORTs, can hold dense and elongated atom clouds, and are thus an excellent way to produce atomic ensembles with high on-axis resonant optical depth (OD). We discuss the design and characterisation of a FORT at 1064 nm added to an existing magneto-optical trapping setup (MOT). After optimisation we trap over 20 million ^{87}Rb atoms with a final temperature around 30 μK, in a cloud approximately 28 μm wide and over 1 cm long. From there we can load a 1D optical lattice maintaining these desirable properties. This upgrade to our atom-light quantum interface represents one side of our efforts to increase the coupling strengths in our atom-x hybrid systems.

I. INTRODUCTION

Independent advances in the quality of and control over diverse quantum systems, be they atoms, high Q-factor membranes, various impurities in crystals, quantum dots, or other kinds of engineered solid state devices, have lead naturally to attempts to couple these different systems. A hybrid system may transfer the advanced control schemes available for one of its constituents to the other. In our lab, for instance, we have sympathetically cooled a Si_3N_4 membrane by coupling it to an ultracold atomic ensemble[1]. Alternatively, a "best-of-both-worlds" hybrid system aims to take advantage of each subsystem's superior properties. Another concrete example our lab is working on is that of an atomic quantum memory for single photons from a GaAs quantum dot[2,3].

It has been shown that the efficiency of a Λ-type quantum memory using atoms depends on the OD of the atomic cloud[4]. Furthermore, a simple 1D-model gives the coupling strength of the atom-light interaction as $g^2 = \alpha_0\eta$, where α_0 is the optical depth and η is the integrated spontaneous emission rate, and while some amendments must be made to get accurate quantitative results for real atomic ensembles the figure of merit describing the coupling remains the OD for all but the most extreme cases[5]. As might be naively expected, in a light mediated atom-membrane hybrid system the effective atom-membrane coupling strength depends on the light-atom and light-membrane coupling strengths,[6] again scaling with OD. All these considerations motivated the design and construction of an optical dipole trap optimised to achieve high OD, and thus high coupling strengths.

II. MODELING

The optical dipole potential[7] is generally given as $U = -\frac{1}{2}\langle \mathbf{pE} \rangle$ for an induced dipole moment $\mathbf{p}$ in a driving field $\mathbf{E}$. Eq. 1 gives the expanded form for the case of a trapping beam at 1064 nm with an intensity profile given by I:

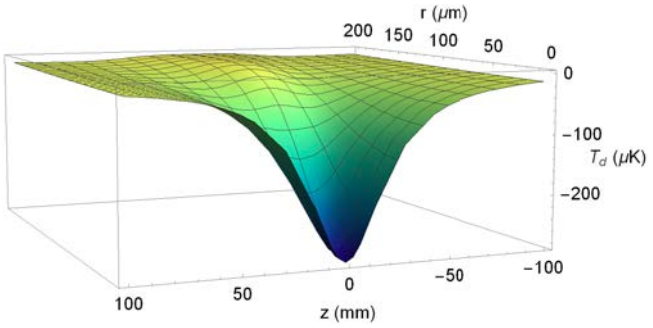

FIG. 1: The shape of the dipole trap potential is plotted with the measured parameters $P = 21$ W, $w_0 = 86\,\mu$m. This yields a trap depth $T_\mathrm{d} = U(r = 0, z = 0)/k_\mathrm{B}$ of 285 μK.

$$U = -\frac{3\pi c^2}{2}\sum_{i=1,2} f_{Di}\frac{\Gamma_{Di}}{\omega_{Di}^3}\left(\frac{1}{\omega_{Di}-\omega}+\frac{1}{\omega_{Di}+\omega}\right) I. \quad (1)$$

Here the f_{Di}s, Γ_{Di}s, and ω_{Di}s are the oscillator strengths, linewidths, and frequencies of the rubidium D1 and D2 lines, ω is the frequency of the trapping laser and c is the speed of light. The detuning is so large that the commonly made rotating wave approximation results in a significant error, and therefore the counterrotating terms have also been included. For a focused Gaussian beam we have:

$$I(r,z) = \frac{2P}{\pi w^2(z)} e^{-\frac{2r^2}{w^2(z)}},\ w^2(z) = w_0^2\left(1+\frac{z^2}{z_R^2}\right), \quad (2)$$

where P is the power, w_0 is the beam waist at the focus, and z_R is the Rayleigh range. The potential is plotted for our experimental parameters in Fig. 1.

III. CHARACTERISATION AND LATTICE

The dipole trap is loaded by continuously overlapping it with the MOT. Our MOT initially loads a large ball of warm atoms which is then compressed and cooled via optical molasses. Parameters like the intensity of

FIG. 2: Absorption image of the dipole trap taken from the side after 1 ms time-of-flight. In this image the cloud is 0.7 mm wide and fills all 2 cm of our field-of-view. The colour maps to OD, with the darkest colours corresponding to $\alpha_0 = 2$.

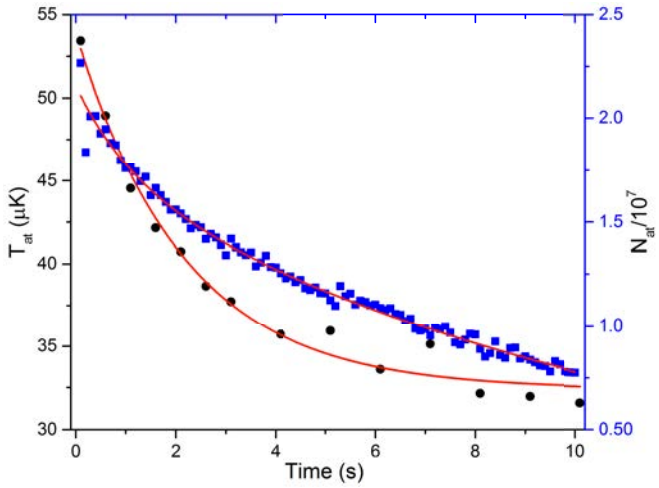

FIG. 3: The number of trapped atoms (square data points) is fit with 2 exponential decay processes to represent evaporation (1.2 s lifetime) and loss through background gas collisions (12 s lifetime). The temperature of the atoms (circular data points) is fit by a single exponential with a lifetime of 2 s.

the repumper beams are optimised to load the maximal amount of atoms into the dipole trap. The final temperature after this process is about 100 μK. Then all beams but the dipole trap are switched off. The resultant atomic cloud is shown in Fig. 2, and the development of the number of trapped atoms and their temperature over time is shown in Fig. 3. The trap depth is measured via the light shift to be 279 μK. The transverse trap frequency is measured independently to be 610 Hz.

For the measured parameters after 100 ms the on-axis resonant optical depth can be calculated to be around 6500. Unfortunately, the highest measurable value for the optical depth with our absorption imaging setup is around 1000, so the most quantitative empirical statement we can make about the on-axis OD is that it is higher than 1000.

We have since successfully loaded and recharacterised the optical lattice we use for our atom-membrane coupling experiment. Temperature and light shift measurements indicate that we manage to load atoms into the lattice's deep troughs. By parametric heating of the lattice we measured a reference scale of axial atomic frequencies in good agreement with theory. The first atom-membrane coupling experiments with the new setup show a resonance in the sympathetic cooling rate. Expected when the axial frequency of the atoms in the lattice matches the membrane's frequency around 276 kHz, we measure a significant shift of this resonance to higher lattice frequencies, which we are still investigating.

IV. OUTLOOK

Challenges and nuances remain in coupling membranes to atomic motion. We are currently preforming upgrades on the membrane side of the experiment, introducing a cryogenic setup and a second generation of membrane design. Additionally, we are looking into the possibility of coupling to internal states of the atomic ensemble[8].

[1] A. Jöckel, A. Faber, T. Kampschulte, M. Korppi, M. T. Rakher, and P. Treutlein, *Sympathetic cooling of a membrane oscillator in a hybrid mechanical-atomic system*, Nature Nanotech. **10**, 55 (2014).

[2] M. T. Rakher, R. J. Warburton, and P. Treutlein, *Prospects for storage and retrieval of a quantum-dot single photon in an ultracold ^{87}Rb ensemble*, Phys. Rev. A **88**, 053834 (2013).

[3] J.-P. Jahn, M. Munsch, L. Béguin, A. V. Kuhlmann, M. Renggli, Y. Huo, F. Ding, R. Trotta, M. Reindl, O. G. Schmidt, et al., *An artificial Rb atom in a semiconductor with lifetime-limited linewidth*, Phys. Rev. B **92**, 245439 (2015).

[4] A. V. Gorschkov, A. André, M. D. Lukin, and A. S. Sorensen, *Photon storage in λ-type optically dense atomic media. II. Free-space model*, Phys. Rev. A **76**, 033805 (2007).

[5] J. H. Müller, P. Petrov, D. Oblak, C. L. Garrido Alzar, S. R. de Echaniz, and E. S. Polzik, *Diffraction effects on light-atomic-ensemble quantum interface*, Phys. Rev. A **71**, 033803 (2005).

[6] K. Hammerer, K. Stannigel, C. Genes, P. Zoller, P. Treutlein, S. Camerer, D. Hunger, and T. W. Hänsch, *Optical lattices with micromechanical mirrors*, Phys. Rev. A **82**, 021803 (2010).

[7] R. Grimm, M. Weidemller, and Y. B. Ovchinnikov, *Optical dipole traps for neutral atoms* (Academic Press, 2000), vol. 42 of *Advances In Atomic, Molecular, and Optical Physics*, pp. 95 – 170.

[8] B. Vogell, T. Kampschulte, M. T. Rakher, A. Faber, P. Treutlein, K. Hammerer, and P. Zoller, *Long distance coupling of a quantum mechanical oscillator to the internal states of an atomic ensemble*, New Journal of Physics **17**, 043044 (2015).

Two-dimensional heterostructures for light harvesting and detection

Nikolaus Flöry,[1] Achint Jain,[1] Palash Bharadwaj,[1] Markus Parzefall,[1]
Takashi Taniguchi,[2] Kenji Watanabe,[2] and Lukas Novotny[1]

[1]*Photonics Laboratory, ETH-Hönggerberg, CH-8093, Zürich, Switzerland*
[2]*National Institute for Material Science, 1-1 Namiki, Tsukuba, 305-0044 Japan*

We present heterostructures made from several two-dimensional crystals that show a strong light-matter interaction. Vertical stacking of multiple materials with distinct electrical and optical properties is a promising route towards the fabrication of novel optoelectronic devices. Electrical characterization as well as spectral and spatial photocurrent measurements provide direct insights into the mechanisms that are relevant for efficient photodetection and light harvesting.

I. INTRODUCTION

Transition metal dichalcogenides (TMDs) in their two-dimensional (2D) form have emerged as a promising class of materials for future optoelectronic devices. Their unique electrical and optical properties include layer dependent band-gaps in the visible spectrum, resulting from quantum confinement effects, as well as strong light-matter interaction due to Van Hove singularities in their density of states[1]. The latter leads to efficient light absorption of 5 – 10 % in a TMD monolayer of less than 1 nm thickness[2] and motivates the use of TMDs for photodetection and photovoltaic applications.

Apart from semiconducting TMDs, the family of 2D crystals that have been studied so far also include insulating hexagonal boron nitride (h-BN) and the well known semimetallic graphene. Multiple layers of different 2D materials can be stacked on top of each other to create heterostructures, held together by van der Waals forces. While this allows for the engineering of novel devices with tailored electrical and optical properties, the physical processes that govern charge generation and transport in such hybrid crystals still require further experimental understanding.

II. SAMPLE FABRICATION

Fabrication of our devices is done using a dry transfer technique developed by Wang *et al.*[3] TMD, h-BN and graphite crystals are mechanically exfoliated onto doped silicon substrates with a thermally grown oxide layer on top and subsequently picked up and placed onto each other in the desired order with a polymer stack (PPC and PDMS). The final heterostructures are deposited on transparent glass substrates and electrical contacts are made using e-beam lithography and evaporation of metal.

III. VERTICAL HETEROSTRUCTURES

A TMD based diode, which is one of the key building blocks for all kind of (opto-)electronic devices, is fabricated by forming a heterojunction between two different TMD flakes, which results in a staggered (type II) band alignment. Figure 1a shows such a device consisting of WSe_2 and $MoSe_2$ (3-layers each) forming an overlapping

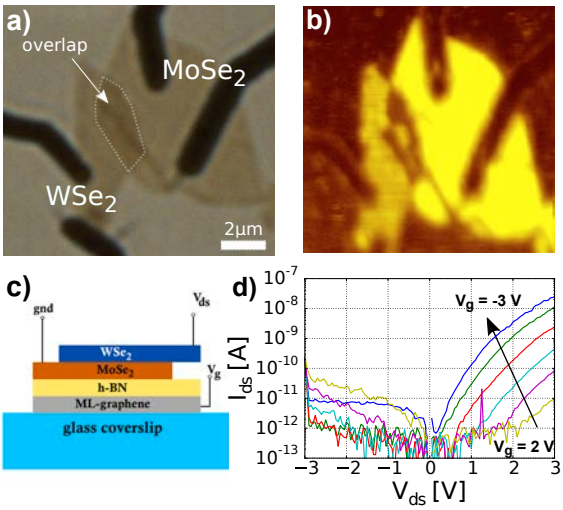

FIG. 1: **a)** Optical micrograph and **b)** PL map of a WSe_2-$MoSe_2$ heterostructure. PL from the overlapping region is strongly quenched compared to the isolated flake regions. **c)** Schematic of the device on a transparent glass substrate utilizing a ML-graphene and h-BN layer as the gate electrode and dielectric layer, respectively. **d)** I – V curves for different gate voltages showing a strong, gate-tunable, rectification.

region. As can be seen in the photoluminescence (PL) map in figure 1b, the PL from the overlapping region is strongly quenched, which is attributed to ultrafast charge separation into opposite bands upon illumination and indicates the formation of a vertical junction. Electrical characteristics, as displayed in Figure 1d, reveal excellent current rectification with on/off ratios greater than 10^4. Furthermore, the drain-source current (I_{ds}) can be tuned by a gate voltage (V_g) applied to the underlying multilayer (ML) graphene gate, separated by an h-BN flake, as illustrated in Figure 1c.

The photocurrent produced by such a heterostructure is predominantly limited by the mobility of charge carriers, both in the TMD flakes and at the metal-semiconductor interfaces. The former issue can be addressed by exploiting the remarkable conductivity of graphene, which can be integrated into vertical heterostructures as transparent electrodes (Figure 2c). This drastically reduces the effective path-length that photoexcited carriers need

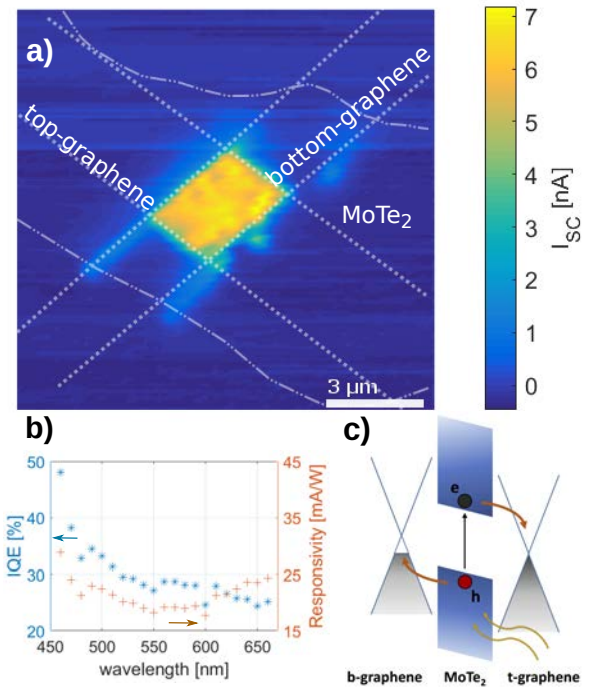

FIG. 2: **a)** Photocurrentmap of a $MoTe_2$ photodetector using graphene as the electrodes. A strong photoresponse is observed where the graphene layers overlap. **b)** IQE and responsivity spectrum measured at a constant power $P_{opt} = 200\,nW$. **c)** Schematic band diagram for a gr-$MoTe_2$-gr heterostructure with built-in field.

to travel through the TMD channel. Figure 2a shows a photocurrent map of a photodetecting device consisting of a 3-layer $MoTe_2$ flake, the absorbing material, sandwiched between two graphene electrodes. The short circuit current (I_{SC}) was measured while illuminated ($\lambda = 650\,nm$, $P_{opt} = 4\,\mu W$) at zero bias ($V_{ds} = 0\,V$). The largest photoresponse originates from the region of the overlap of all three materials, confirming that photoexcited charges in $MoTe_2$ are efficiently separated into the graphene electrodes. The built-in field in this device results from an asymmetry in the workfunctions of the two graphene flakes and can be further increased by applying a source-drain bias voltage (V_{ds}). Recent studies observed a picosecond photoresponse in similar devices, limited mostly by the thickness of the TMD channel[4]. Thus, reducing the TMD thickness to only a mono- or few-layer flake, as in the presented device, leads to a faster photoresponse; however, recombination losses start to play a significant role in such thin devices. Consequently, the internal quantum efficiency (IQE), which provides a direct measure of how many electrons are generated per absorbed photon, is reduced. The IQE for a given wavelength λ is defined by

$$\mathrm{IQE}(\lambda) = \frac{1}{\mathrm{A}(\lambda)}\mathrm{EQE}(\lambda) = \frac{1}{\mathrm{A}(\lambda)}\frac{\mathrm{I_{ph}}}{\mathrm{q}}\frac{\mathrm{hc}}{\mathrm{P_{opt}}\lambda}, \qquad (1)$$

where EQE is the external quantum efficiency (number of generated electrons per incident photon), $A(\lambda)$ is the effective absorption, q is the charge of an electron and I_{ph} and P_{opt} are the measured photocurrent and the incident optical power, respectively. Figure 2b shows the IQE and photoresponsivity for different wavelengths, measured at a constant power of $P_{opt} = 200\,nW$. The photoresponsivity varies between $18 - 29\,mAW^{-1}$, which can be partially attributed to a wavelength dependent material absorption. The IQE, however, nearly doubles towards smaller wavelengths (higher energy photons). This indicates a different carrier relaxation pathway with reduced recombination losses, the origin of which we are currently investigating.

IV. CONCLUSION AND OUTLOOK

We have shown that the vertical assembly of such 2D-materials is ideal to study the physical processes that govern charge generation and transport in optoelectronic applications. In our prototypical devices we were able to observe strong rectification and a pronounced photoresponse. More complex structures can be fabricated by stacking several absorbing TMD layers between graphene electrodes in order to extend the absorption spectrum and to enhance the overall EQE.

Acknowledgments

This work was supported by the NCCR- QSIT program (grant 51NF40 160591) and the Swiss National Science Foundation (grant 200021 149433).

[1] L. Britnell, R. M. Ribeiro, A. Eckmann, R. Jalil, B. D. Belle, A. Mishchenko, Y.-J. Kim, R. V. Gorbachev, T. Georgiou, S. V. Morozov, et al., *Strong light-matter interactions in heterostructures of atomically thin films.*, Science **340**, 1311 (2013).

[2] M. Bernardi, M. Palummo, C. Grossman, and R. Scienti, *Extraordinary Sunlight Absorption and One Nanometer Thick Photovoltaics Using Two-Dimensional Monolayer Materials.*, NanoLetters **13**, 3664 (2013).

[3] L. Wang, I. Meric, P. Y. Huang, Q. Gao, Y. Gao, H. Tran, T. Taniguchi, K. Watanabe, L. M. Campos, D. a. Muller, et al., *One-dimensional electrical contact to a two-dimensional material.*, Science **342**, 614 (2013).

[4] M. Massicotte, P. Schmidt, F. Vialla, K. G. Schädler, a. Reserbat-Plantey, K. Watanabe, T. Taniguchi, K. J. Tielrooij, and F. H. L. Koppens, *Picosecond photoresponse in van der Waals heterostructures.*, Nature Nanotechnology **11**, 1 (2015).

Thermal creep of vortices within strong pinning theory

M. Buchacek,[1] R. Willa,[1] V.B. Geshkenbein,[1] and G. Blatter[1]

[1] *Institute for Theoretical Physics, ETH Zürich, 8093 Zürich, Switzerland*

We study pinning and flow (creep) of vortices in type-II superconductors in presence of low density of strong defects. Extending the strong pinning theory to account for thermal fluctuations, we develop a quantitative treatment of vortex creep and calculate the current-voltage (force-velocity) characteristic. We find that the pinning force may be enhanced due to thermally enlarged trapping region of the defect, in which case the charactersitic crosses the $T = 0$ curve.

I. INTRODUCTION

The discovery of high-temperature superconductivity has opened a possibility of physical and experimental realisation of systems of interacting vortices, or more generally interacting elastic springs. Most high-temperature superconductors are type II and develop a vortex phase for intermediate magnetic fields. Unlike in the Meissner phase characterised by complete expulsion of the magnetic field, the superconductor in the vortex phase is penetrated by magnetic field $\mathbf{B}$ through localised vortices, each carrying a flux quantum $\Phi_0 = hc/(2e)$. In the ideal case, vortices are aligned in a triangular lattice of lattice constant $a_0 \propto (\Phi_0/B)^{1/2}$.

Upon applying an external current $\mathbf{j}$, vortices start moving due to the Lorentz force $\mathbf{F}_L = \mathbf{j} \times \mathbf{B}/c$ opposed by the viscous dissipative forces $\mathbf{F}_d = -\eta \mathbf{v}$. This motion produces an electric field parallel to the applied current, which leads to the dissipation of energy. The superconducting property characterised by dissipation-free current flow can be restored by inserting defects to the superconductor, which attract vortices and exert the *pinning* force $F_{\rm pin}$ on the vortex lattice (Fig. 1). As long as the driving force does not exceed the maximal (critical) pinning force F_c, vortices don't move and dissipation is prevented. The velocity is $v = (F_c - F_L)/\eta$ for higher driving forces, which results in linear current-voltage (equivalent to force-velocity) characteristic (Fig. 2).

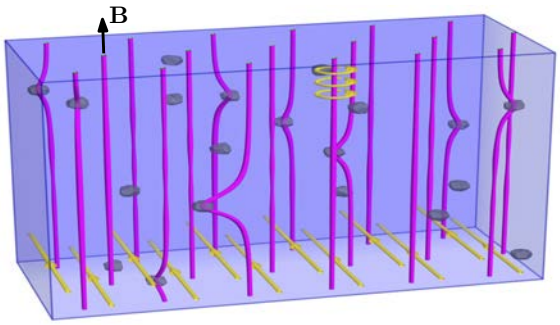

FIG. 1: Vortices of magnetic field in type-II cuperconductors pinned to strong defects.

We study the strong pinning scenario in which single strong defect is able to induce finite force on the lattice. The microscopic theory of strong pinning[1] could be used to calculate the pinning force and hence the maximal (critical) current j_c that we can apply to the superconductor without losing the dissipationless current flow. The aim of our research is to extend the theory to account for thermally activated *creep*, in which vortices hop from one pinning site to another. Our approach is quantitative and thus different from the weak pinning (pinning force arises due to local density fluctuations of weak defects) where only phenomenological arguments for the vortex creep are known[1].

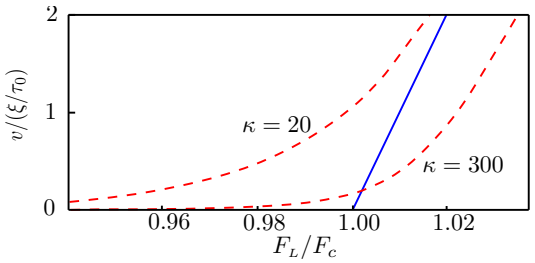

FIG. 2: Solid line: force-velocity characteristic of a generic type-II superconductor without thermal fluctuations. Dashed curves: calculated force-velocity characteristic at small temperatures $T/U_{\rm max} = 10^{-2}$ in presence of defects modelled by the Lorentzian pinning potential $e_p(r) = U_{\rm max}/(r^2 + \xi^2)$ and for different pinning strengths κ. If the pinning is very strong, the characteristic crosses the $T = 0$ curve.

II. STRONG PINNING

Presence of strong defects results in plastic deformations of the vortex lattice. We consider single defect in the origin interacting with the nearest vortex at distance x. The energy of such system takes an effective form[2] containing elastic and potential energy contributions

$$e_{\rm pin}(x; r) = \frac{1}{2}\bar{C}(x - r)^2 + e_p(r). \qquad (1)$$

We use r for the position of the vortex tip. The scaling form for the elastic constant $\bar{C}$ is known from the elasticity theory[3]. The bare pinning potential $e_p(r)$ describes the interaction of the vortex core with the pinning centre decaying on the coherence length ξ (corresponding to the vortex core radius). The equlibrium position $r_{\rm eq}(x)$ of the vortex tip is derived from minimising the effective energy (1),

$$\bar{C}(x - r_{\rm eq}) = f_p(r_{\rm eq}). \qquad (2)$$

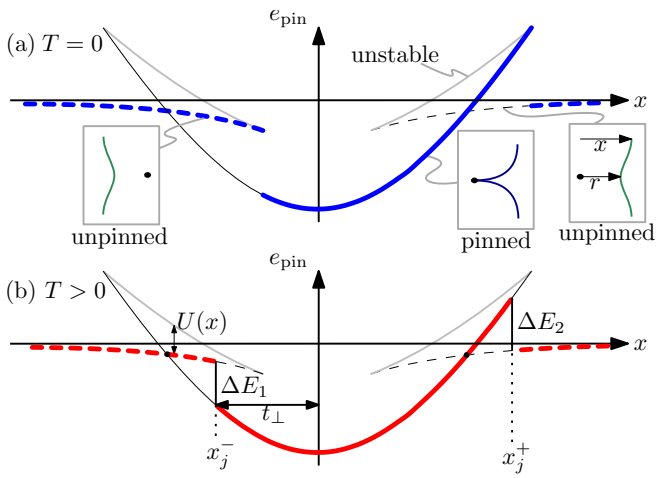

FIG. 3: Multivalued energy landscape with pinned (solid) and unpinned (dashed) branches. (a) Occupation of branches (thick) for $T = 0$ and qualitative illustration of pinned and unpinned vortices. (b) Occupation for $T > 0$ (thick) determined by the rate equation.

In the regime of strong pinning potentials or weak elasticity (more precisely if $\max f_p'(r) > \bar{C}$), the equilibrium equation (2) admits multivalued solutions $r_{\rm eq}(x)$. This defines the *strong pinning* regime and leads to a multivalued energy landscape $e_{\rm pin}(x; r_{\rm eq})$ (Fig. 3) with pinned and unpinned branches. The two branches are energetically separated by a finite barrier $U(x)$ derived from the unstable solution of (2) maximising (1).

III. THERMAL EFFECTS

The key information needed to find the force-velocity characteristic of the vortex phase is the occupation of branches. We find this by applying the Kramer's rate theory[4], which at non-zero low temperatures $T \ll U$ leads to the rate equation

$$\frac{dn}{dx} = \frac{n_{\rm eq} - n}{v\tau(x)}. \qquad (3)$$

Here $n(x)$ denotes the fraction of vortices in the pinned branch, which becomes $n_{\rm eq}(x)$ in the thermal equilibrium. Vortices moving with velocity v accross the pinning centre need time $\tau(x) = \tau_0 e^{U(x)/T}$ to reach the equilibrium. Exact calculation shows that $n(x)$ changes rapidly between $n = 1$ (all vortices are pinned) and $n = 0$ (all vortices unpinned) at points $x_j^{\pm}(v, T)$ (Fig. 3)

The average pinning force is obtained by integrating $f_{\rm pin}(x) = -de_{\rm pin}/dx$ over the occupied branches (denoted by $f^o_{\rm pin}$). The integral can be approximated by the height of two 'jumps' between branches in the energy landscape.

$$F_{\rm pin}(v, T) = \left| \frac{1}{a_0} \int_{-a_0/2}^{a_0/2} f^o_{\rm pin}(x)\, dx \right| = \frac{\Delta E_1 + \Delta E_2}{a_0}. \quad (4)$$

IV. RESULTS

We identify three velocity regimes with different scaling of the average pinning force $F_{\rm pin}(v, T)$ (Fig. 4).

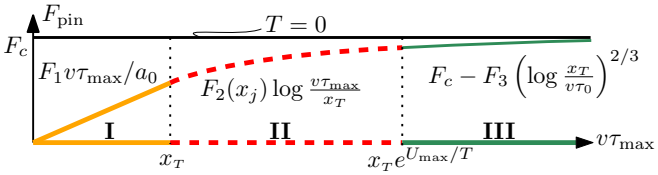

FIG. 4: Scaling regimes of the pinning force for velicities varied over an exponentially large scale. The thermal scale is $x_T \sim \xi(T/U_{\max})$ (I and II) but becomes $x_T \sim \xi(T/U_{\max})^{2/3}$ in (III). The constants F_0, F_3 and the slowly-varying function $F_2(x_j)$ can be derived from the microscopic theory. The maximal waiting time is denoted by $\tau_{\max} = \tau_0 e^{U_{\max}/T}$. The pinning force for $T = 0$ is independent of the velocity.

The results mentioned above describe only interactions of one vortex. The macroscopic pinning force experienced by the whole lattice is reduced by a factor $t_\perp/a_0$ denoting the fraction of vortices experiencing a particular defect. The trapping distance $t_\perp$ is enhanced compared to $T = 0$ ($t_\perp$ corresponds to the left jump in occupation on Fig. 3). This may lead to an overall enhancement of the pinning force beyond the $T = 0$ value and may result in the crossing of the linear force-velocity characteristic (Fig. 2).

The strong pinning can be quantified using the *Labusch parameter* $\kappa = \max f_p'/\bar{C}$. However, the analysis for the common model of pinning potential $e_p(r) = e_0/(r^2 + \xi^2)$ shows that the pinning force enhancement can be realised only at experimentally inaccessible values of $\kappa \approx 150$. We are currently developing an analytic approach to understand properties of the maximal pinning force. Our aim is also to design pinning potentials able to maximise this effect and realize it for more realistic values of κ.

[1] G. Blatter, M. V. Feigel'man, V. B. Geshkenbein, A. I. Larkin, and V. M. Vinokur, *Vortices in high-temperature superconductors*, Review of Modern Physics **66**, 1125 (1994).

[2] J. A. G. Koopmann, V. B. Geshkenbein, and G. Blatter, *Peak effect at the weak to strong pinning crossover*, Physica C **404**, 209 (2004).

[3] R. Willa, V. B. Geshkenbein, and G. Blatter, *Probing the pinning landscape in type-II superconductors via Campbell penetration depth*, Phys. Rev. B **93**, 064515 (2016).

[4] P. Hänggi, P. Talkner, and M. Borkovec, *Reaction-rate theory: fifty years after Kramers*, Rev. Mod. Phys. **62**, 251 (1990).

Magnetic resonance force microscopy of influenza virus

Marc-Dominik Kraß,[1] Urs Grob,[1] Hiroki Takahashi,[1] Brad Moores,[1] and Christian Degen[1]

[1]*Department of Physics, ETH Zurich, Otto Stern Weg 1, 8093 Zurich, Switzerland*

Magnetic resonance force microscopy (MRFM) is a scanning probe microscopy based technique to mechanically detect forces between a nanomagnet and the magnetic moments in a nanometer-scale sample. Using ultrasensitive micromechanically fabricated silicon cantilevers 3D-imaging of nanoscale objects with a spatial resolution better than 10 nm can be achieved.[1]

I. INTRODUCTION

Related to the nuclear magnetic resonance (NMR) spectroscopy MRFM measured the spatial distribution of nuclear magnetic moments in a sample. Placing the sample in a strong magnetic field produces a Zeeman splitting between the nuclear spin states. Applying rf-radiation at the Larmor frequency of the spins induces transitions between the spin states. By flipping the spins in the sample the sign of the magnetic force between the sample and the nanomagnet close to it is changed resulting in a bending of the mechanical force sensor. Inducing these spin flips periodically with the cantilever's resonance frequency leads to a resonant excitation of the cantilever. The oscillation amplitude is proportional to the number of excited spins.[2]

Due to the magnetic field gradient produced by the sharp nanomagnet the magnetic resonance condition is only met within a thin hemispherical slice around the magnet for a given rf-frequency. The spatial resolution is determined by the width of this slice respectively by the magnetic field gradient. By scanning the magnet with respect to the sample the spatial distribution of nuclear spins in the sample can be reconstructed.

II. EXPERIMENTAL SETUP

In our setup the sample is fixed at the end of a mechanical force detector which is placed close to a nanomagnet in an external field. Single influenza viruses are attached on a nanorod produced by focused ion beam milling (FIB). This nanorod is glued on a micromechanically fabricated soft cantilever ($k \approx 1 \times 10^{-4}$ N/m, $f_0 \approx 3$ kHz). The nanomagnet made of dysprosium is deposited on a stripline which is used to apply rf-pulses to the sample. A fiber-optic interferometer is used to measure the cantilever deflection directly. The whole setup is placed in a cryostate at 4 K an in high vacuum below 10^{-6} mbar to reduce drift, thermal noise, and damping of the cantilever. Quality factors of 40 000 and more can be achieved.

III. RESULTS

Interactions between the cantilever and a substrate can lead to a significant change in the cantilever's resonance frequency. By using a feedback loop to excite the cantilever always at its resonance frequency tthe frequency shift can be tracked. This can be used to perform different imaging modes to precharacterize the sample an to align the sample and the nanomagnet.

FIG. 1: Touchmap of the end of a nanorod with influenza viruses attached (white bumps). The noisy gray areas are artifacts due to frequency instabilities.

A. Touch maps

In this mode the frequency shift is recorded as a function of the z-piezo displacement, comparable to force-distance curves in atomic force spectroscopy. The surface is defined as the position where the frequency shift exceeds a certain threshold. Performing this measurement for every pixel of an images gives the topography of a sample. Figure 1 shows a so-called touch map of the nanorod at the end of the cantilever performed on a sharp silicon tip on the substrate. To resolve a structure with this method the radius of curvature of the used tip must be smaller than the structure itself.

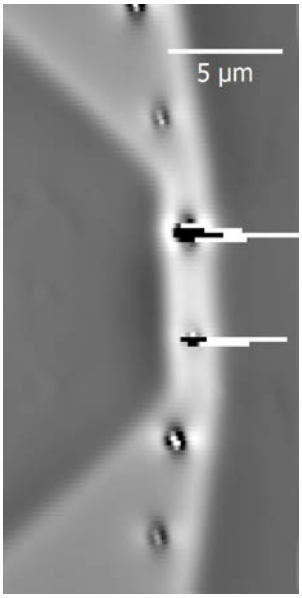

FIG. 2: Frequency map of the stripline with six nanomagnets on it. There is a clear contrast between the substrate (dark gray) and the stripline (light gray). The two magnets on the narrow part are larger than the other ones and therefore induce a higher frequency shift.

B. Frequency maps

The frequency shift can also be recorded as a function of the scanning position at a constant z-piezo displacement. This imaging mode is much faster than the touch map and provides contrast for different heights and materials. Due to this the interpretation of these images is not as straight forward as for the touch maps but for the alignment of the stripline it can be sufficient. As usual in constant height scanning modes the cantilever tip can be damaged on rough surfaces.

Figure 2 shows a frequency map of the stripline with six magnets on it. There is a clear contrast between the substrate and the stripline made of gold. Close to the nanomagnets the frequency shifts can be very high.

IV. OUTLOOK

In the next step 3D-images of an influenza virus will be recorded. Since imaging with a high resolution is a time-consuming task recently developed techniques like phase multiplexing can be used to reduce data acquisition times.[3]

To demonstrate a chemical contrast a ^{13}C labeled influenza virus could be imaged. With the help of phase multiplexing both signals can be acquired at the same time.

[1] C. L. Degen, M. Poggio, H. J. Mamin, C. T. Rettner, and D. Rugar, *Nanoscale magnetic resonance imaging*, Proceedings of the National Academy of Sciences **106**, 1313 (2009).
[2] M. Poggio and C. L. Degen, *Force-detected nuclear magnetic resonance: recent advances and future challenges*, Nanotechnology **21**, 342001 (2010).
[3] B. A. Moores, A. Eichler, Y. Tao, H. Takahashi, P. Navaretti, and C. L. Degen, *Accelerated nanoscale magnetic resonance imaging through phase multiplexing*, Applied Physics Letters **106**, 213101 (2015).

Towards single nuclear spin detection using magnetic resonance force microscopy

M. Héritier,[1] Y. Tao,[1] U. Grob,[1] M.-D. Krass,[1] A. Eichler,[1] and C. Degen[1]

[1] *Institute of Solid State Physics, ETH-Hönggerberg, CH-8093, Zürich, Switzerland*

We aim to detect a single nuclear spin using magnetic resonance force microscopy (MRFM). MRFM merges nuclear magnetic resonance (NRM) detection with scanning probe microscopy (SPM) enabling to reach much better spatial resolution than conventional NMR. We present the key parameters of the sensitivity of such setup and how we plan to improve them in order to get a sufficient signal-to-noise ratio to detect a single nuclear spin.

I. INTRODUCTION

Magnetic resonance force microscopy (MRFM) is a technique combining chemical sensitivity of nuclear magnetic resonance (NMR) and the high spatial resolution of scanning probe resolution. Similarly to conventional NMR imaging, the spins of the sample of interest are inversed back and forth and the fluctuating magnetization is measured. Instead of using a pick-up coil, the sample is placed on the tip of a cantilever. If the sample lies in a magnetic field gradient, a net force is excerted on the cantilever, causing it to be bent. Inverting the spins of the sample will inverse the force. Therefore, if the rate corresponds to the resonance frequency of the cantilever, it will drive it efficiently. Similarly to an atomic force microscope (AFM), the cantilever displacement is measured by a laser interferometer. A schematics of a typical MRFM setup is shown in figure 1 a). This approach to magnetic resonance has enabled to detect a single electron spin[1] and to get magnetic resonance imaging resolution down to below ten nanometers[2]. The aim of this project is to improve the state-of-the-art components of the MRFM to detect a single nuclear spin. This correspond to an improvement of the sensitivity roughly by a factor 100.

II. SENSITIVITY OF THE MRFM SETUP

In the present case (statistical- and not thermal polarization of the spins), the single-spin signal-to-noise ratio (SNR) writes

$$SNR = \frac{(\mu G)^2}{S_F}\sqrt{t \cdot \tau_m}\,, \tag{1}$$

where μ is the magnetic moment of the nucleus, G is the magnetic field gradient, S_F is the spectral density of the force noise, τ_m is the spin lifetime of the sample (intrinsic) and t is the total experimental averaging time. It is directly seen from this equation that a sample with τ_m reasonably long must be chosen. Furthermore, the force noise spectral density writes

$$S_F = \frac{4k_BT}{Q}\sqrt{k \cdot m}\,, \tag{2}$$

where Q is the mechanical quality factor of the cantilever, k its spring constant and m its effective mass. The quality factor is a measure of how well can the cantilever store energy: it is proportional to the ratio of the energy stored to the energy lost during one cycle.

III. PROPOSED IMPROVEMENTS FOR THE SENSITIVITY

TABLE I: Comparison of the parameters defining the SNR between state-of-the-art and aimed ones in this project. (The expected SNR is given for a measurement with 8 hours of averaging and for $\tau_m = 0.1$ s.)

	State-of-the-art	This project
Q	$10'000$	$130'000$
k	90 μN/m	0.7 μN/m
m	60 pg	3.7 pg
T	4 K	0.3 K
expected S_F	7 aN/$\sqrt{\text{Hz}}$	0.08 aN/$\sqrt{\text{Hz}}$
G	4.6 MT/m	28 MT/m
expected SNR	0.06	$1'200$

From these considerations, the sensitivity of the MRFM setup can be improved if

- the temperature T is decreased,
- the magnetic field gradient G is increased,
- the mechanical properties of the cantilever are improved such that the quality factor Q is increased and the spring constant k and the effective mass m are reduced.
- Furthermore, a strong non-contact friction appears due the large end radius of conventional cantilevers (~ 1 μm) which reduces as well the force sensitivity.

Decreasing the temperature will be done using a dilution fridge. For the magnetic field gradient improvement, write head of a commercial hard drive will be used. Besides the high gradient of 28 MT/m reported[3], it has the great advantages over nanomagnets of having a really flat surface ($<$ 1 nm smoothness) and can be rapidely switched on and off. A stripline will then need to be fabricated via lithography on the write head

surface in order to have a radio-frequency antenna used to manipulate the sample's spins. A schematics of a write pole integrated into an MRFM setup is pictured in figure 1 b).

In order to improve the Q factor, chemical surface passivation is used to remove the native surface oxide. Then the surface is protected against rapid oxide formation in air via various chemical terminations, such as oxygen- or fluorine termination[4]. Furthermore, to reduce effects of the non-contact friction on the quality factor, single-crystal diamond nanowire tips are used. They have a 10 nm end radius and experience no friction down to 10 nm distance between the tip and the surface[5]. SEM images of diamond nanowire tips are shown in figure 1 c).

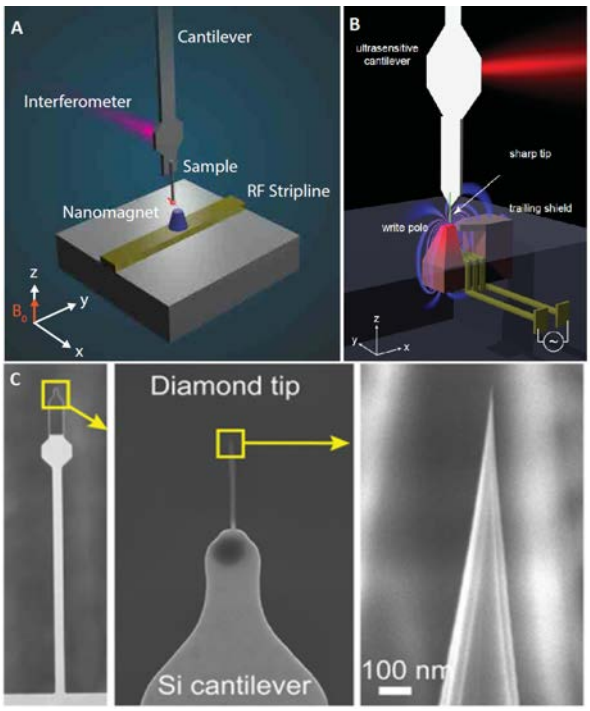

FIG. 1: a) Scheme of a conventional MRFM setup. A nanomagnet used to produce a magnetic field gradient is placed on top of a radio-frequency stripline that enables to manipulate the spins of the sample. The sample is placed at the end of a cantilever whose motion is detected by a laser interferometer. b) Scheme of an MRFM setup where the nanomagnet has been replaced by a hard drive write head. The stripline is not seen here but is lithographed on top of the write head. c) SEM pictures of the diamond nanowire tips that will be used in this project[5].

Finally, in the effort to reduce the spring constant k and the effective mass m of the cantilever, we are currently testing nanoladder cantilevers made out of diamond. While k and m should be reduced, the longitudinal stiffness should be maintained, so that snap-in-to-contact is prevented when the cantilever is approached very close to the surface. Table I summaries the state-of-the-art key parameters and compares them to the ones aimed in this project.

IV. OUTLOOK

If a single nuclear spin can be detected with the MRFM setup, this would enable to image and to locate spatially individual atoms in molecules. Besides that, if the SNR is sufficiently big, the nuclear spin state could be readout. This would be really interesting for quantum readout experiments as their lifetime at cryogenic temperatures can be really long.

[1] D. Rugar et al., Nature **430**, 329 (2005).
[2] C. L. Degen, M. Poggio, H. J. Mamin, C. T. Rettner, and D. Rugar, Proc. Natl Acad. Sci. USA **106**, 1313 (2009).
[3] Y. Tao, A. Eichler, T. Holzherr, and C. L. Degen, arXiv:1512.03185 (2015).
[4] Y. Tao, J. M. Boss, B. A. Moores, and C. L. Degen, Nature Communications **5**, 3638 (2014).
[5] Y. Tao and C. L. Degen, Nano Letters **15**, 7893 (2015).

Quantum computing with enlarged Hilbert spaces

Maciej Malinowski,[1] Florian Leupold,[1] Joseba Alonso,[1] Chi Zhang,[1] and Jonathan Home[1]

[1] *Institute for Quantum Electronics, ETH-Zürich, 8093 Zürich, Switzerland*

While most experimental implementations of quantum gates operate on qubits, using higher-dimensional states, such as qutrits, can be both advantageous and experimentally feasable. We show how a single $^{40}Ca^{+}$ ion in a Paul trap can be used as an 3–level system that can be easily manipulated and read-out. Such a qutrit is used to violate the KCBS inequality, proving contextuality of hidden-variable theories of quantum mechanics. In a two-qutrit system it is possible to generate entanglement, as well as engineer various different spin-spin couplings.

I. INTRODUCTION

One of the most promising platforms for constructing a universal quantum computer is by using trapped ions. In such a system, singly-ionised atoms are held in an electromagnetic trap inside a vacuum chamber, and are thereby very well decoupled from the environment. Resonant laser pulses allow us to cool the ions down to the quantum ground state, which offers a starting point for quantum state manipulation and control.

Inside a trapped ion computer, information is stored as a superposition of different electronic energy levels. We then require that these orbitals do not have a fast decay channel, so that many coherent operations can be performed. Typically, two energy levels are selected, allowing to store quantum information as *qubits*. However, the dimension of available Hilbert space is not limited to 2. We will see how a single trapped $^{40}Ca^{+}$ ion allows us to store quantum information in a higher-dimensional structure, such as a *qutrit* (3-level system). Laser pulses allow us to achieve full control over this Hilbert space via single- and two-ion gates.

There is a range of interesting phenomena this allows us to study. For example, using higher-dimensional systems together with qubits allows to reduce the number of steps necessary to create Toffoli gates[1]. Another interesting application is the simulation of spin lattice systems, where increased size of Hilbert space means we can study more complex interactions[2]. Finally, systems with 3 or more levels are useful for foundational quantum mechanics, such as disproving non-contextual hidden-variable (HV) theories by violating the Klyachko-Can-Binicioglu-Shumovsky (KCBS) inequality[3]. We have recently demonstrated such a violation.

II. EXPERIMENTAL SETUP

Our experiments are conducted inside a 4 K cryostat on $^{40}Ca^{+}$ ions trapped in a harmonic potential 50 um above the surface of a chip trap. The electronic structure of $^{40}Ca^{+}$ is shown in Figure 1. Couplings necessary for state preparation are provided by laser light at 397 nm (state read-out and laser cooling), 866 nm (repumping) and 854 nm (reset). State manipulation is performed by applying 729 nm radiation resonant with desired transitions within Zeeman sub-levels of $S_{1/2}$ and $D_{5/2}$ manifolds. Laser frequencies can be fine-tuned within a range of approximately 30 MHz by using Acousto-Optic Modulators (AOMs). Sequences of pulses are applied by switching the AOMs on or off with direct digital synthesisters (DDS's), which are controlled via a FPGA.

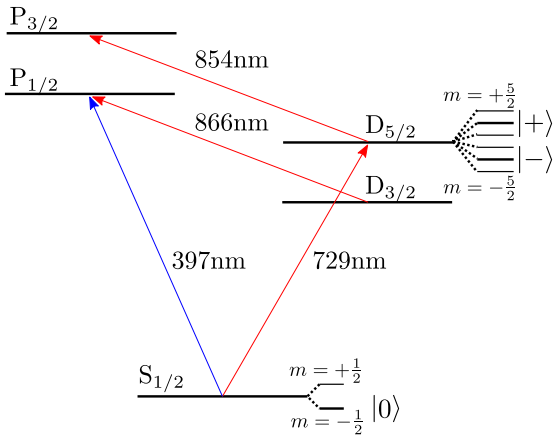

FIG. 1: Energy level scheme of $^{40}Ca^{+}$. Shown in detail are the Zeeman sub-levels that can be used for implementing a qutrit.

In order to implement quantum information with high-dimensional systems, several features are required. First of all, we need to have access to several long-lived quantum states. These are provided by the sub-levels of the $D_{5/2}$ manifold, which can only decay via a dipole-forbidden transition to the $S_{1/2}$ ground state. With an external B-field of 4 G, the transitions are spaced far enough for levels to be addressed spectrally, but close enough to all be accessible by tuning the frequency of a single laser beam with AOMs.

Finally, we need the ability to measure the system precisely. We can detect population in $S_{1/2}$ by applying the read-out beam at 397 nm and observing fluorescence. Since this beam does not couple to the $D_{5/2}$ state, our measurements preserve the populations and coherence within the $D_{5/2}$ manifold. By performing multiple detection events separated by a coherent inversion between the relevant $S_{1/2}$ and $D_{5/2}$ states, we can therefore perform a high-fidelity read-out of the complete state of the system.

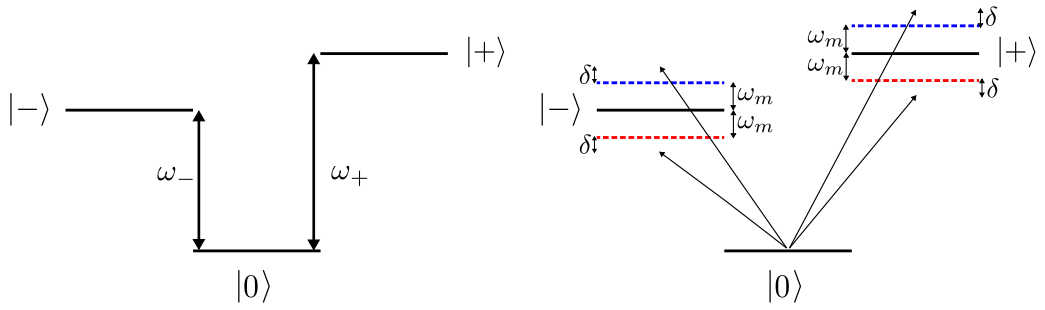

FIG. 2: Left: Qutrit system implemented in $^{40}Ca^+$. State $|0\rangle$ is a Zeeman sub-level of $S_{1/2}$ manifold. States $|\pm\rangle$ are Zeeman sub-levels of $D_{5/2}$ manifold. Right: Mølmer-Sørensen-type interaction for a qutrit.

III. QUANTUM LOGIC

Consider a qutrit as shown in figure 2. A complete set of single-ion logic can be achieved by applying in sequence multiple pulses at frequencies ω_+ and ω_-. Furthermore, by applying pulses at both frequencies simultaneously, we can perform a gate that couples $|+\rangle$ and $|-\rangle$.

In order to create conditions for performing universal computation as well as quantum simulations we need to have means of generating entanglement between two ions. We think this should be possible by employing Mølmer-Sørensen-type schemes, where multiple pulses near-resonant with motional sidebands create entangling couplings. For example, by simultaneously applying four pulses at frequencies $\omega_+ \pm (\omega_m + \delta)$, $\omega_- \pm (\omega_m + \delta)$, we can generate an effective Hamiltonian $H_{\text{eff}} \sim S_x \otimes S_x$, where $S_x = \frac{1}{2}(S_+ + S_-)$ is the sum of spin raising and lowering operators for a spin-1 system. By exploring similar means, we can generate $S_x \otimes S_z$ couplings, as well as generate maximally entangled states. We believe that these methods will allow for creating high-quality entanglement of qutrits despite anomalously large heating rates observed for our single trapped ions. This can be for example achieved by choosing ω_m to be the frequency of normal mode that is only sensitive to differential electric field noise on both ions (fields affecting ion strings are to first order homogenous, so this greatly reduces noise).

IV. CONTEXTUALITY TESTS

Somewhat surprisingly, higher-dimensional quantum states are relevant for answering questions in foundational quantum mechanics. We say that quantum theory is contextual if a measurement outcome depends on what other compatible measurements it is conducted together with. The Kochen-Specker (KS) theorem states that if the dimension of Hilbert space is 3 or bigger, any HV theory explaining the measurements must be contextual. Thus, by using a single qutrit, one can place contraints on HV theories without referring to non-locality or entanglement. Just as it is the case of Bell inequalities, contextuality tests can be conducted by measuring the values of correlators of subsequent measurements.

Our setup provides a clean platform for studying this problem. For measurements following the ones described in literature[3], we obtain a correlator value of $\langle\chi\rangle = -3.92(6)$. This violates the KCBS inequality $\langle\chi\rangle \geq -3$ and is also very close to the quantum mechanical bound of -3.944. We hope that reaching a value even closer to the quantum-mechanical limit may provide useful insights into theoretical understanding of quantum foundations. Furthermore, we are looking into the possibility of performing contextuality measurements on a pair of entangled qutrits.

V. CONCLUSIONS

$^{40}Ca^+$ ions trapped in a harmonic well form a good system for quantum manipulations not only for qubits, but for higher-dimensional states as well. By driving transitions between an $S_{1/2}$ state and different sub-levels of $D_{5/2}$ manifold, we can perform single-ion rotations and state readout of qutrits. One application of single-qutrit operations is to prove contextuality of HV theories, and correlation measurements on such systems can be interesting from the point of view of foundational quantum physics. Two-ion interactions are achieved by simultaneously shining multiple frequencies of light, and these can be used to obtain different effective Hamiltonians, and in turn generate entanglement.

[1] B. P. Lanyon et al., *Simplifying quantum logic using higher-dimensional hilbert spaces*, Nature Physics **5**, 134 (2009).
[2] C. Senko et al., *Realization of a quantum integer-spin chain with controllable interactions*, Phys. Rev. X. **5**, 021026 (2015).
[3] M. Jerger et al., *Contextuality without nonlocality in a superconducting quantum system* (2016), (arXiv:1602.00440 [quant-ph]).

Single photon on-chip microwave switch

Jean-Claude Besse,[1] Marek Pechal,[1] and Andreas Wallraff[1]

[1]*Department of Physics, ETH Zurich, CH-8093 Zurich, Switzerland*

An on-chip switch, capable of routing classical as well as quantum microwave signals from one input to any of two inputs within less than 10 ns is reported. Our sample is designed to be fully compatible with standard superconducting technology, and is based on interference to perform with close to no loss. We characterize its operation at the single photon level on superpositions of Fock states $|0\rangle$ and $|1\rangle$.

I. INTRODUCTION

Superconducting circuit quantum electrodynamics is a promising technology towards the realization of a quantum computer[1]. While the number of qubits placed on a chip scales with improving nanofabrication technology, the number of output lines is often limited by the dilution fridge characteristics. The ability to route at will microwave photons, without suffering from slow switching speeds, high dissipations and/or requiring a change in fabrication technology to be integrated with superconducting circuits, could solve that scaling problem and has been demonstrated previously[2,3]. However these designs only route the signal to a single output or reflect it towards the input, and have been tested only with coherent classical signals. Here we present a switch design based on superconducting circuits that has the ability to send a highly quantum state to any of two outputs.

II. WORKING PRINCIPLE OF THE SWITCH

Our switch, shown in Fig. 1, is based on two $\pi/2$ hybrid couplers connected by two tunable coplanar waveguide resonators. The signal at position "in" will be split equally between positions "a" and "b", but with a 90 degrees phase difference imprinted in the amplitude. Depending on the state of the resonators (resonant or off-resonant with the frequency of the signal, chosen by the external magnetic flux through the SQUID loops at the center of the resonators), the microwave components at positions "a" and "b" will be either transmitted to "c" and "d" or reflected. Due to interferences at the hybrid couplers, the signal will then be either fully recomposed at port 2 (in the off-resonant case) or port 3 (in the resonant case). Using the flux lines to bias the SQUID loops, microwave signals can be routed on our chip in less than 10 ns switching time with almost no dissipation (manuscript in preparation).

In order to demonstrate the operation of the switch with purely quantum input states, we placed a transmon qubit at the input, acting as a single photon source. We can excite it with a coherent drive from its weak coupling with port 1, while it decays rapidly with a typical time constant of 90 ns to the waveguide labeled "in".

The sample is a 7x4 mm substrate of sapphire coated on top with a niobium film, patterned using photolithography to define the coplanar waveguides and capacitances. Josephson junctions for the SQUID loops and the photon source are written using electron-beam lithography and shadow evaporation of aluminium.

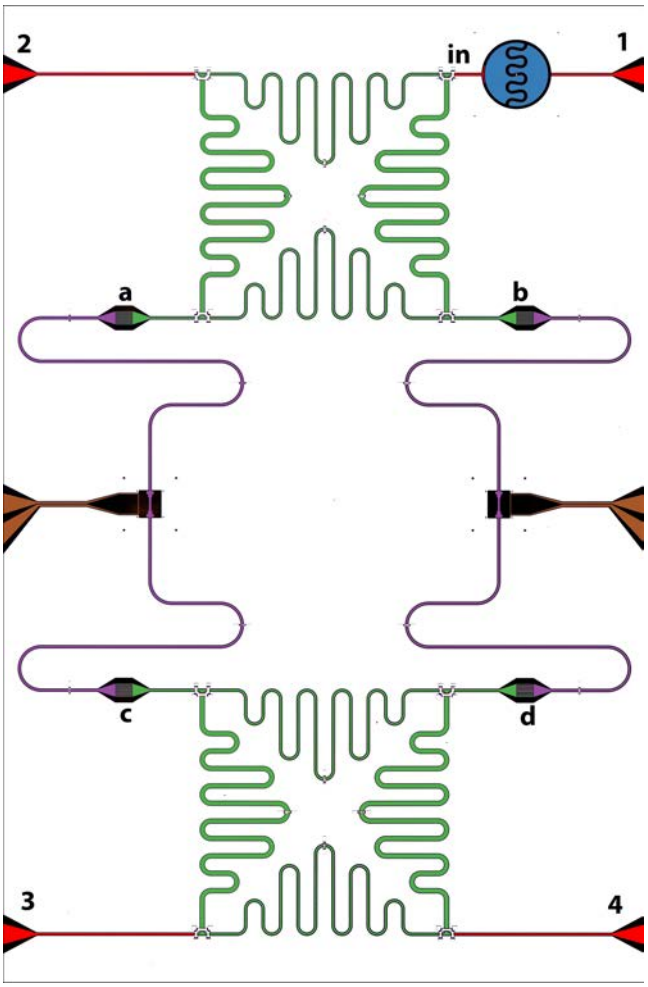

FIG. 1: False color micrograph of the sample, of size 7x4 mm, with the in-/out-puts lines shown in red, the transmon-based single photon source in blue, the hybrids in green, the resonators interrupted by SQUID loops in purple, and the flux lines in brown (color online).

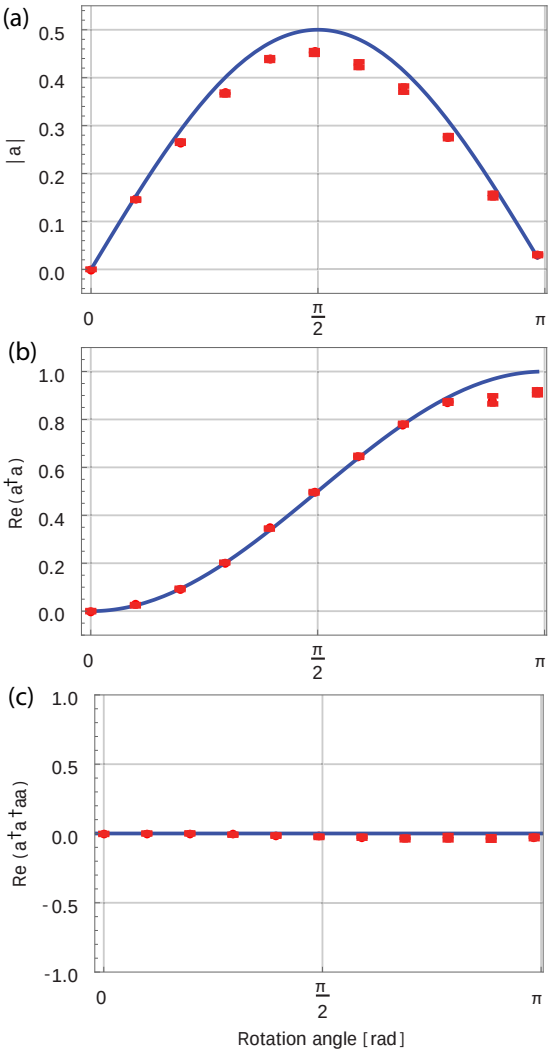

FIG. 2: Chosen moments of the output field at port 3 as a function of the preparation rotation angle. Red points show data with statistical error bars, blue curves indicate theoretically expected values (color online).

III. QUANTUMNESS OF THE SWITCHED SIGNAL

By varying the strength of a short (10 ns) coherent pulse sent to input 1, we prepare the microwave field emitted by the qubit as a superposition of Fock states $|0\rangle$ and $|1\rangle$, that we define uniquely by its rotation angle θ:

$$|\psi\rangle = \cos(\theta/2)\,|0\rangle + \sin(\theta/2)\,|1\rangle\,. \qquad (1)$$

Moments of the photon mode a are deduced by analyzing single-shot voltage measurements with and without the presence of the signal[4]. For our input state, we expect the moments $\langle a\rangle = \sin(\theta/2)\cos(\theta/2)$ and $\langle a^\dagger a\rangle = \sin^2(\theta/2)$. Our results, plotted against theoretical curves in Fig. 2(a,b), show reasonable agreement with our expectations. The slightly lower values of $|a|$ obtained are consistent with our estimates of dephasing of the single photon source due to flux noise. We don't have an explanation for the lower than expected last two values of Fig. 2(b) at this time.

Of particular interest is the fact that all (normally ordered) moments containing more than one a operator will vanish. As a check we look at the (zero-time) second order coherence function $g^{(2)} = \langle a^\dagger a^\dagger a a\rangle / \langle a^\dagger a\rangle^2$, which goes to zero for all of our input states, while any classical state would have a value of at least 1. We plot the numerator of $g^{(2)}$ in Fig. 2(c) and verify that it is indeed very close to zero. The slight deviation towards negative values (we obtain $g^{(2)} = -0.03 \pm 0.01$ for the state $|1\rangle$) can be explained by a thermal population of the qubit excited state of the order of 0.01, roughly consistent with our fridge temperature (40 mK) and operating frequency (7.1 GHz). This leads to a slight overestimate of the noise in the measurement without the signal.

IV. CONCLUSION

We demonstrated operation at the single photon level of an on-chip microwave switch, capable of sub 10 ns switching times, that can be readily integrated with current superconducting nanofabrication technology. Contrary to previously reported devices, we can route signals from one output to any two outputs, thus distinguishing easily an intentionally diverted signal from spurious reflections in the sample. We expect our device to prove very useful for applications such as scaling the number of elements in circuit quantum electrodynamics chips.

[1] M. Devoret and R. J. Schoelkopf, *Superconducting circuits for quantum information: An outlook*, Science **339**, 1169 (2013).

[2] B. J. Chapman, B. A. Moores, E. I. Rosenthal, J. Kerckhoff, and K. W. Lehnert, *General purpose multiplexing device for cryogenic microwave systems*, arXiv:1603.02716 (2016), URL `http://arxiv.org/abs/1603.02716`.

[3] O. Naaman, M. O. Abutaleb, C. Kirby, and M. Rennie, *On-chip josephson junction microwave switch*, Applied Physics Letters **108**, 112601 (2016), URL `http://scitation.aip.org/content/aip/journal/apl/108/11/10.1063/1.4943602`.

[4] C. Eichler, D. Bozyigit, and A. Wallraff, *Characterizing quantum microwave radiation and its entanglement with superconducting qubits using linear detectors*, Phys. Rev. A **86**, 032106 (2012), URL `http://pra.aps.org/abstract/PRA/v86/i3/e032106`.

Quantum Work Fluctuations

Martí Perarnau-Llobet,[1] Elisa Bäumer,[1,2] Karen Hovhannisyan,[1] Marcus Huber,[3,1] and Antonio Acín[1,4]

[1] *ICFO — The Institute of Photonic Sciences, Mediterranean Technology Park, 08860 Castelldefels (Barcelona), Spain*
[2] *Institute for Theoretical Physics, ETH Zurich, 8093 Zürich, Switzerland*
[3] *Departament de Física, Universitat Autònoma de Barcelona, 08193 Bellaterra, Spain*
[4] *ICREA-Institució Catalana de Recerca i Estudis Avançats, Lluis Companys 23, 08010 Barcelona, Spain*

Work is one of the most fundamental quantities in thermodynamics. While classically there is consensus on the definition of work, it remains an open question how to define and especially how to measure work in the quantum case. Ideally one would like to construct a measurement scheme that can provide the fluctuations of work of any process, including those that involve quantum coherence. Seeing that the standard approach, the so-called two projective measurement, fails, motivates us to consider new measurement schemes, for which we impose two minimal requirements: Firstly, the average over the emerging probability distribution should satisfy the first law of thermodynamics and, secondly, in absence of quantum coherence classical statistics shall be recovered. The incompatibilty of these two requirements is proven, but also some possibilities for improvement by making use of global measurements on many copies were found.

I. INTRODUCTION

In phenomenological thermodynamics we describe the behaviour of macroscopic systems in equilibrium and thus have one definite value for each quantity. In statistical mechanics we consider fluctuations and therefore look at the different microstates compatible with some macroscopic variables. While in the microcanonical ensemble we assume that each microstate of a system has the same probability to occur, in the canonical ensemble the system is in thermal equilibrium with a heat bath and thus has a fixed temperature T. Here, the internal energy is given by the Gibbs-Boltzmann distribution, i.e. the probability to be in a microstate with energy E_k is given by $p_k = e^{-\beta E_k}/Z$ with $\beta = 1/k_B T$, where k_B is the Boltzmann constant and $Z = \sum_k e^{-\beta E_k}$ is the partition function. This induces the fluctuations we consider in statistical thermodynamics.

According to the law of large numbers, the mean value of a quantity converges to its expectation value for large systems. Since thermodynamics deals with systems containing a large number of particles, statistical thermodynamics yields in the thermodynamic limit the same results as what we would expect from phenomenological thermodynamics. In fact, in statistical thermodynamics we can formulate the laws of thermodynamics to hold for the average values of the probability distributions. If we look at finite size systems the laws of thermodynamics must not always hold, but only if we consider average quantities.

As the name suggests, quantum thermodynamics deals with small quantum systems, sometimes even with single quantum systems. Here, we try to apply our knowledge about the behaviour of large thermodynamic systems to small quantum systems by allocating a probability distribution according to the distribution we would get in statistical thermodynamics. Of course, for such small systems the fluctuations are very relevant.

In quantum physics, fluctuations have two different origins. Classical fluctuations are induced by our lack of control, or ignorance, on the state of the system. For example, the noise induced by a thermal environment creates uncertainty on the state of the system, which then can be described by a Gibbs-Boltzmann probability distribution. On the other hand, quantum fluctuations, induced by quantum coherence, are present even if one has perfect knowledge on the state of the system. Focusing our attention on energy fluctuations, states with classical uncertainty are diagonal in the basis of the Hamiltonian, $\rho = \sum_i p_i |i\rangle\langle i|$, and we therefore refer to them as *classical states*. In the general case with off-diagonal elements, the so-called quantum coherence, we will talk about *quantum states*. While it is known how to measure the classical fluctuations of work, measuring the fluctuations when dealing with quantum coherence is still an open question. Our main goal was to find a measurement scheme for these quantum fluctuations.

II. THEORY

From classical thermodynamics[1] we know that the work performed on the system is defined as the energy added to the system via a reversible process. In general processes, the change of internal energy dU equals the sum of the infinitesimal work δW and the non-reversible part δQ, called the added heat, leading to the *first law of thermodynamics*: $dU = \delta Q + \delta W$. In the case of a thermally isolated system, i.e. a system where $\delta Q = 0$, the work performed on the system equals the change of internal energy, $\delta W = dU$. Thus the work performed on the system only depends on the initial and final state, such that it can be easily determined by measuring the internal energy of the initial state and subtract if from the internal energy of the final state.

As mentioned before, if we approach these laws from the statistical mechanics' point of view and consider fluctuations, these laws need to hold for the average values, in this case $\langle W \rangle = \langle \Delta U \rangle$.

Looking at the quantum case, it is not that clear anymore

how to define and especially measure work. When measuring the energy of the state ρ, it collapses into one of its eigenstates $|i\rangle\langle i|$ with probability p_i. Thus, the post-measurement state can be written as $\rho' = \sum_i p_i |i\rangle\langle i|$. If there is only classical uncertainty, i.e. if our initial state ρ is diagonal, the probability distribution of the post-measurement state equals the initial state before the measurement and we get the correct statistics. If we have quantum coherence though, any measurement destroys it, as the post-measurement state is still diagonal in the basis of the Hamiltonian and thus can not account for the quantum uncertainty we had before. The evolution of the state after the measurement would then lead to different results than without measuring before. This prevents us from applying a measurement scheme analogous to the classical case.

Given a density matrix ρ and a Hamiltonian $\mathcal{H}$ we can calculate the internal energy by $U = \mathrm{tr}(\rho\mathcal{H})$, which corresponds to the average internal energy $\langle U\rangle$ in the classical case. This means that instead of the single trajectories of the change of internal energy, only the average change of internal energy is operationally well defined. Thus, the probability distribution describing the fluctuations of work is not well defined, but only its average value is. Our goal is to find a feasible probability distribution that describes the work performed on a system while undergoing a thermally isolated process, that gives the classical results for classical states and that satisfies the first law of thermodynamics.

One widely known approach is to define work via the so-called *two projective measurement* (TPM) scheme[2]. Here, analogously to the classical case, our state is measured twice, once in the beginning and once in the end. Starting in any initial quantum state ρ_i, we begin with a measurement that makes our state collapse into one of its eigenstates ρ_i' with energy ε_k. We then apply the unitary U and afterwards measure our final state ρ_f' with energy ε_l' giving us the work values $w = \varepsilon_l' - \varepsilon_k$. The probability distribution we get using this TPM scheme is then given by:

$$p(w) = \sum_{k,l} \delta(w - (\varepsilon_l' - \varepsilon_k))\rho_{kk}|u_{lk}|^2, \qquad (1)$$

where $\rho_{kk} := \langle k|\rho|k\rangle$ is the probability to collapse during the first measurement into the eigenstate with energy ε_k and $u_{lk} = \langle l'|U|k\rangle$ is the probability to go from the eigenstate with energy ε_k to another eigenstate with energy ε_l'.

However, the unitary evolution will be applied to the already collapsed state ρ_i', which is in general different to our initial state ρ_i and thus, for general states: $\rho_f' = U\rho_i'U^\dagger \neq \rho_f = U\rho_i U^\dagger$. This indicates that the average work might not comply with the change of internal energy we would expect according to the application of a unitary U. Indeed, when calculating the average work

$$\langle W\rangle_{TPM} = \sum_w wp(w) \qquad (2)$$

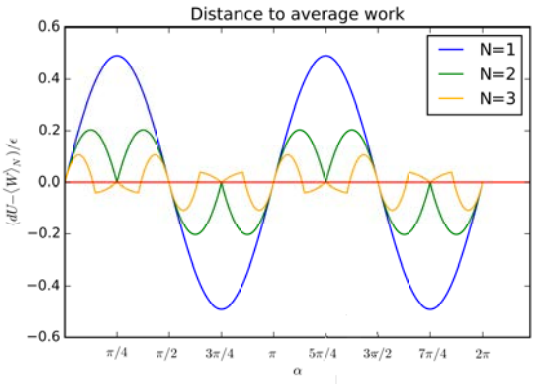

FIG. 1: Difference between the average work according to the first law and the average work we would get according to our POVMs constructed for one, two and three copies, respectively, for an initial state with maximal coherence that is undergoing a unitary evolution U(α).

using (1), the TPM scheme does in general not recover the average work value given by the first law of thermodynamics.

III. RESULTS

In our corresponding article[3] we have shown that it is impossible to find a measurement scheme for the quantum fluctuations of work that agrees with the first law of thermodynamics and gives us the classical results in the case of a state that has no quantum coherence. However, if we consider global measurements on N copies, we were able to construct measurement schemes for a small number N that lead to an average work that is closer to the change of internal energy, while the TPM constraints were fully satisfied. Unfortunately, we did not find a construction for arbitrary N yet. We believe that for many qubits with $N \to \infty$ we would get the perfect improvement, i.e. our requirements would become compatible, but we were not able to prove that conjecture yet.

[1] R. Renner, Lecture notes *Theorie der Wärme FS 2013*. URL `https://www1.ethz.ch/demoitp/education/fs13/tdw/tdw2013`

[2] P. Talkner, E. Lutz, P. Hänggi, Phys. Rev. E **75**, 050102(R) (2007)

[3] M. Perarnau-Llobet, E. Bäumer, K. Hovhannisyan, M. Huber, A. Acín *Quantum Fluctuations of Work and Generalised Quantum Measurements* (in preparation)

Quantum Wires defined by Cleaved Edge Overgrowth - Challenges & Future Goals

Luca Alt,[1] Stefan Riedi,[1] Matthias Berl,[1] Christian Reichl,[1] Werner Dietsche,[1] and Werner Wegscheider[1]

[1]*Solid State Physics Laboratory, ETH-Hönggerberg, CH-8093, Zürich, Switzerland*

We investigate the one dimensional (1D) physics of Cleaved Edge Overgrowth (CEO) quantum wires (QWR) using AlGaAs/GaAs Molecular Beam Epitaxy (MBE). Those very pure and atomically precise quantum systems are expected to reveal new physics of 1D Luttinger Liquids. Especially we are interested in the creation of separately gatable coupled QWRs and experiments inducing topological superconductivity in a wire due to the proximity effect and the influence of a magnetic field. The first step towards this goal is the fabrication of AlGaAs/GaAs-quantum wires, grown epitaxially with molecular beam expitaxy (MBE), using the cleaved edge overgrowth (CEO) technique.

I. INTRODUCTION

First experiments using the cleaved edge overgrowth (CEO) technique date back to 1990, when L. Pfeiffer and co-workers successfully fabricated a two-dimensional electron gas (2DEG) by overgrowing a in-situ cleaved edge (110) of a GaAs wafer (100) with molecular beam epitaxy (MBE)[1]. This was the foundation of ballistic 1D quantum wires created by MBE. In the following decade several studies investigated the magneto-transport of electron[2,3] and hole[4] systems in 1D QWR created by CEO.

In contrast to 2D or 3D systems, where electron-electron interaction can be neglected (Fermi-liquid model), in a 1D system this interaction is dominant (Luttinger liquid[5]). CEO QWR are the ideal host to study strong electron-electron interaction due to the long transport mean free path resulting from the high sample purity and the atomically precise epitaxy.

Even though the CEO technique was invented over twenty years ago, only few groups managed to successfully create such wires. This is due to various technical difficulties, which will be discussed in the next section.

II. EXPERIMENTAL REALISATION

The concept of a quantum wire fabrication using the CEO technique is shown in Fig. 1. We start with a AlGaAs/GaAs heterostruture growth along the (001) direction (Fig. 1 a). Then we define top gate structures on top of our sample by standard optical lithography and metal deposition (Fig. 1 b), before we reintroduce the sample into the MBE chamber. The sample is cleaved along the (110) direction (Fig. 1 c) in the ultra high vacuum environment of the MBE chamber, followed by a second MBE growth along the cleaved (110) plane (Fig. 1 d). Thus we can grow heterostructures along two crystal directions without contaminating the interface in between. The quantum wire forms at the interface between the heterostructures by careful gate depletion (Fig. 1 e). At a certain voltage (V_D), the 2DEG is depleted, but due to the additional doping in the (110) growth direction, electrons will remain on the interface, i.e., a quantum wire, tunable in it‘s 1D modes by further careful gate voltage depletion, is formed. The length of the quantum wire is given by the width of the top gate. The 2DEG is contacted on each side of the gate, which allows for four-terminal transport measurements.

As mentioned in section I, processing a wire by CEO is technologically challenging. Since a atomically flat surface is needed, the cleaving has to take place within the MBE right before the growth, in order to avoid oxidation and contamination. To get a good cleave, a well adjusted cleaving apparatus is needed within the MBE-chamber. To improve the cleave the waver has to be thinned from the backside[6] to about 100 μm. The smoothness of the (110) surface after the cleave is crucial.

Since GaAs cleaves best on (110) lattice planes, the second growth is in (110) direction. The high quality growth of AlGaAs/GaAs heterostructures along the (001) direction is much better studied. Due to the non-polar nature of the (110) surface, As_4 does not stick to it very well and the growth is more challenging[6]. For the (110) growth an arsenic overpressure is used.

To avoid contamination of the MBE chamber while performing the second growth, the sample has to be cleaned to be free of any material that may desorb in vacuum or when the sample is heated. This limits the variety of materials one can use as top gate.

III. EXPERIMENTAL APPLICATIONS

Our first goal is to build such a wire in an high mobility AlGaAs/GaAs system. Once this is achieved the development of separately gateable AlGaAs/GaAs quantum wires will be of interest. Within the first MBE growth illustrated in Fig 1, a second AlGaAs/GaAs/AlGaAs stack will be grown. This will create a second wire which will be gated using structured back gates created by oxygen ion implantation. In our group the compatibility of such gates with high mobility samples was shown[7]. The upper wire will be gated with a top gate. With this setup the coupling between the wires can be studied and Coulomb drag can be seen.

For stronger spin-orbit interactions, InAs wires would be of interest in the future.

Another project planned after the realisation of a single wire is the creation of a topological superconducting s-

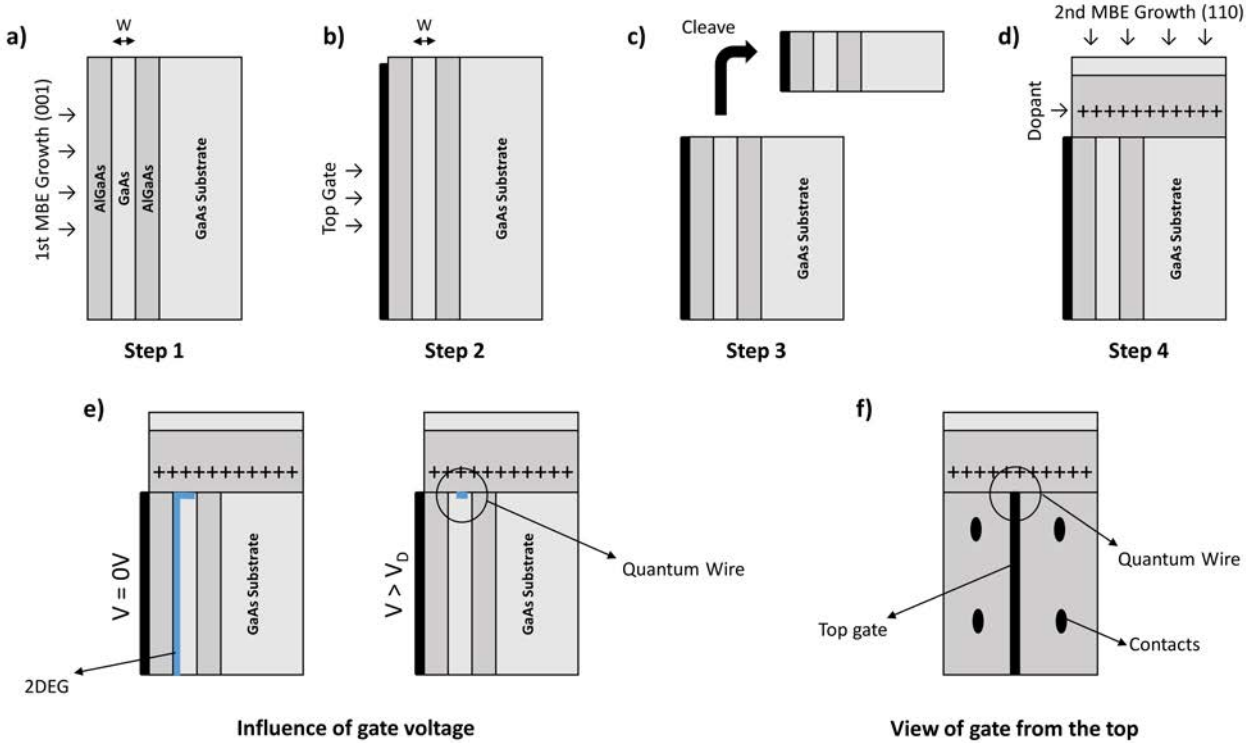

FIG. 1: a): (001) MBE Growth of a 2DEG b): ex-situ fabrication of the top gates c): in-situ cleave d): (110) MBE Growth e): schematic showing the 2DEG and the electron accumulation at the interface f) Top view.

tate. The basic setup needed is a 1D wire with spin-orbit coupling, a s-wave superconductor and an magnetic field to break time-reversal symmetry[8]. The idea is to deposit a superconductor onto the cleaved edge. Due to the proximity of the superconductor and the influence of a magnetic field a topological superconducting state should be induced in the wire[9,10]. Near the ends of the wire at the interface between the topological superconducting state and the trivial state, Majorana Fermions are predicted[9,10]. Majorana Fermions are of great interest regarding the topic of qubits in quantum computing.

Acknowledgments

We would like to thank QSIT and SNF for the financial support.

[1] L. Pfeiffer, K. W. West, H. L. Stormer, J. P. Eisenstein, K. W. Baldwin, D. Gershoni, and J. Spector, *Formation of a high quality two-dimensional electron gas on cleaved GaAs*, Applied Physics Letters **56**, 1697 (1990), ISSN 00036951.

[2] T. B. Laboratories and M. Hill, *Quantum Wires Formed By Cleaved Edge Overgrowth*, **37**, 547 (1994).

[3] A. Yacoby, H. Stormer, N. Wingreen, L. Pfeiffer, K. Baldwin, and K. West, *Nonuniversal Conductance Quantization in Quantum Wires*, Physical Review Letters **77**, 4612 (1996), ISSN 0031-9007.

[4] L. N. Pfeiffer, R. De Picciotto, K. W. West, K. W. Baldwin, and C. H. L. Quay, *Ballistic hole transport in a quantum wire*, Applied Physics Letters **87**, 2005 (2005), ISSN 00036951.

[5] T. Giamarchi, *Quantum physics in one dimension* (Clarendon Press - Oxford, 2003).

[6] L. Pfeiffer, H. L. Störmer, K. West, and K. W. Baldwin, *Quantum wire structures by MBE overgrowth on a cleaved edge*, Journal of Crystal Growth **111**, 333 (1991), ISSN 00220248.

[7] M. Berl, L. Tiemann, W. Dietsche, H. Karl, and W. Wegscheider, *Structured back gates for high-mobility two-dimensional electron systems using oxygen ion implantation*, Applied Physics Letters **108**, 132102 (2016), ISSN 0003-6951.

[8] Y. Oreg, G. Refael, and F. Von Oppen, *Helical liquids and Majorana bound states in quantum wires*, Physical Review Letters **105**, 1 (2010), ISSN 00319007, 1003.1145.

[9] V. Mourik, K. Zuo, S. M. Frolov, S. R. Plissard, E. P. a. M. Bakkers, and L. P. Kouwenhoven, *Signatures of Majorana Fermions in*, Science **336**, 1003 (2012), ISSN 0036-8075, 1204.2792.

[10] J. Alicea, *New directions in the pursuit of Majorana fermions in solid state systems.*, Rep. Prog. Phys. **75**, 076501 (2012), ISSN 1361-6633, arXiv:1202.1293v1.

Towards bang-bang generation of squeezed states of a trapped-ion oscillator

Chi Zhang,[1] Joseba Alonso,[1] Florian Leupold,[1] Maciej Malinowski,[1] and Jonathan Home[1]
[1]*Institute of Quantum Electronics, ETH, CH-8093, Zürich, Switzerland*

We present an experiment to generate squeezed states by bang-bang control of a single ion's motion. The enabling technology is based on cryogenic digital switches placed in vacuum next to the ion trap. These switches can induce fast changes to the trapping potential in the nanosecond timescale. Motional state squeezing can be attained by switching between two potential wells of different curvatures. Overlapping the centers of the two wells is critical in this process, and for that we have developed a method to calibrate the voltage offsets on the two voltage supply lines. Once we can create squeezed states, the same technique can be used to amplify the separation between the two motional wave packets of a Schrödinger-cat state.

I. INTRODUCTION

Fast control of quantum systems is essential to take advantage of their non-classical properties before they are lost to the environment. Among various approaches, the fastest possible is achieved by so-called bang-bang techniques, which make use of instantaneous large changes of the control fields[1]. We have implemented bang-bang control of the trapping electric potentials by means of cryogenic digital switches. With them we have created large coherent states with up to 10,000 quanta of energy[2]. Our technique also allows for fast transport of ions, which could be beneficial for quantum information processing[3]. At a more fundamental level, we are interested in the generation of squeezed states via parametric amplification. We can achieve this by switching between two potential wells with different curvatures[3].

A squeezed state is a Heisenberg-limited state with suppressed uncertainty in one quadrature and enlarged uncertainty in the other. Mathematically, squeezed states can be created by applying the squeezing operator $S(\xi) = e^{(\xi^* \hat{a}^2 - \xi \hat{a}^{\dagger 2})}$ to the motional ground state, where $\xi = re^{i\phi}$ is the complex squeezing parameter, with r denoting the magnitude and ϕ the phase of the squeezing. Squeezed states can be used for quantum-enhanced measurements, allowing for uncertainties below the standard quantum limit[4]. Our bang-bang squeezing scheme can also be used as a parametric Schrödinger-cat amplifier.

II. EXPERIMENT

The setup for this experiment is the same as the one used for generating large coherent states[2]. A surface-electrode Paul trap, as shown in Fig. 1, is used to confine our $^{40}Ca^{+}$ ions. The radio-frequency (RF) field from two RF electrodes provides radial confinement to the ions, while the electrostatic DC fields from the middle and outer segmented electrodes confine the ions axially.

In ion traps, it is common to place strong low-pass filters as close to the trap as possible, to prevent noise on the DC voltages applied to the electrodes from disturbing the trapping potential and leading to heating and decoherence of the ion's motional states. However, these strong filters also suppress the high-frequency components of waveforms applied to the electrodes to manipulate motional states or to transport ions. To induce fast changes on the oscillator states, we implemented cryogenic complementary metal-oxide-semiconductor (CMOS) electronic switches inside our vacuum system. These allow for switching of the voltages applied to the trap electrodes from several heavily filtered voltage supply lines in less than 4.0 ns. Therefore, even though the voltage on each filtered supply line remains unchanged within one experimental sequence, the trapping potential can be changed much faster than the ion oscillation frequency. In our current setup, five DC electrodes are connected to such fast switches, as highlighted in Fig. 1.

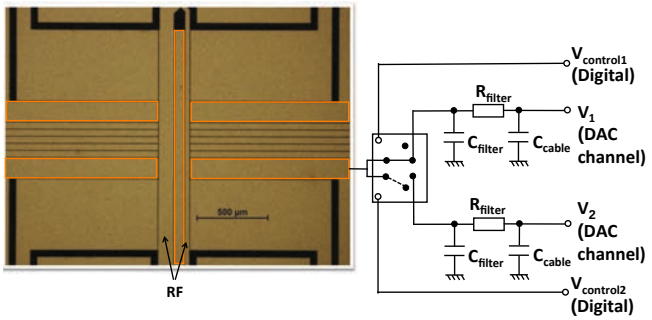

FIG. 1: Surface-electrode trap (left), and cryogenic switching electronics (right). The five DC electrodes connected to the fast switches are highlighted. Digital control signals determine which static voltage supply line is connected to the trap electrode. These digital signals are supplied by a pulse generator, which is synchronized with the experimental sequence with a field-programmable gate array (FPGA). The analog voltages are provided by a low-noise digital-analog-converter (DAC) and are heavily filtered with low-pass filters. The static voltage applied to the other non-switchable electrodes are also provided by DAC channels and then filtered.

To generate squeezed states we need to switch between two potential wells with different frequencies (Fig. 2). We prepare a single ion close to its motional ground state in a potential well with an ion oscillation frequency of ω_1 by electromagnetically induced transparency (EIT) cooling[5]. We then suddenly trigger the switches and change

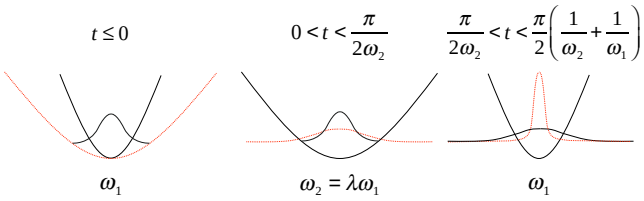

FIG. 2: Parametric amplification scheme for the generation of squeezed states. The ion is initially prepared in the ground state of the first trap with trap frequency ω_1. At $t = 0$ the trap frequency is suddenly changed to ω_2, and the ion is at a squeezed state of the second well. After the ion has evolved in the second well for one quarter of its period, we switch the trap frequency back to ω_1, where we end up with a squeezed state with $r = -\log\lambda$. This process can be in principle concatenated to increase the squeezing magnitude r.

the ion oscillation frequency to $\omega_2 = \lambda\omega_1$ at $t = 0$. After this change, the ion is in a squeezed state of the second well. For $\lambda < 1$, this wave packet will coherently expand until it becomes maximally anti-squeezed after one quarter of the second well's period. At this time, we switch back to the ω_1 trapping well. These operations are equivalent to applying the squeezing operator $S(\xi)$ with $\xi = -\log\lambda$ to the motional ground state. In principle this process can be concatenated to create larger squeezed states. The ultimate limit in our setup could be due to two effects. One is the heating rate due to noise on the electrodes[3], which we have measured to be 1 phonon per 2 ms for the ground state. The other is the drift in ion oscillation frequency due to the slowly-varying stray electrical fields, which is in the order of 100 Hz in 1 hour for our setup.

For this experiment it is critical that the two trapping wells spatially overlap with each other exactly, since switching between two non-overlapping wells would displace the squeezed states[2]. We find that applying the same nominal voltages onto the vacuum feedthroughs corresponding to the V_1 and V_2 lines of the switches (Fig. 1) leads to different trapping potentials. This could be due to different contact potentials along the different lines. In order to ensure that the centers of both wells overlap, we need to counter these voltage offsets. To do that, we trigger one of the five switches individually, while keeping the remaining four connected to their corresponding V_1 lines. We let the ion evolve for half a period and then switch back to V_1. In this way, any residual displacement will be most evident. We scan the voltage V_2 and set it to the value which minimizes the displacement. From these values we determine the offsets between V_1 and V_2 lines for each individual electrode. We can use the same procedure to overlap the ω_1 and ω_2 wells for squeezing.

III. OUTLOOK

With the centers of the ω_1 and ω_2 wells overlapped, we should be able to generate squeezed states. We will study the experimental limit of this technique by concatenating the sequence shown in Fig. 2. In the future we intend to apply this squeezing scheme to Schrödinger-cat states prepared with state-dependent forces[6], to parametrically amplify the separation between the two wave packets of the trapped-ion mechanical oscillator. Besides, the improvements in control which will be necessary for this work will also be required for fast ion transport experiments, which would greatly assist in quantum information processing.

Acknowledgments

We would like to thank Matteo Marinelli, Vlad Negnevitsky and Ben Keitch for the development of the control systems.

[1] S. Damodarakurup, M. Lucamarini, G. Di Giuseppe, D. Vitali, and P. Tombesi, *Experimental inhibition of decoherence on flying qubits via "bang-bang" control*, Physical Review Letters **103**, 040502 (2009).

[2] J. Alonso, F. Leupold, Z. Soler, M. Fadel, M. Marinelli, B. Keitch, V. Negnevitsky, and J. Home, *Generation of large coherent states by bang-bang control of a trapped-ion oscillator*, Nature Communications **7**, 11243 (2016).

[3] J. Alonso, F. M. Leupold, B. Keitch, and J. Home, *Quantum control of the motional states of trapped ions through fast switching of trapping potentials*, New Journal of Physics **15**, 023001 (2013).

[4] V. Giovannetti, S. Lloyd, and L. Maccone, *Quantum-enhanced measurements: Beating the standard quantum limit*, Science **306**, 1330 (2004).

[5] C. Roos, D. Leibfried, A. Mundt, F. Schmidt-Kaler, J. Eschner, and R. Blatt, *Experimental demonstration of ground state laser cooling with electromagnetically induced transparency*, Physical review letters **85**, 5547 (2000).

[6] H.-Y. Lo, D. Kienzler, L. de Clercq, M. Marinelli, V. Negnevitsky, B. C. Keitch, and J. P. Home, *Spin-motion entanglement and state diagnosis with squeezed oscillator wavepackets*, Nature **521**, 336 (2015).

Valleytronics in Strain-Engineered Graphene

Lujun Wang,[1] Peter Makk,[1] and Christian Schönenberger[1]

[1] *Department of Physics, University of Basel, CH-4056, Basel, Switzerland*

Electron valley, analogous to spin, is a good quantum number in graphene due to the large momentum difference in k-space. It has been proposed that the valley degree of freedom can be used for the next generation electronics. Here we aim to address valley by strain engineering in ballistic suspended graphene since gigantic pseudo-magnetic fields can be created by strain, which act on the valley-degree of freedom.

I. INTRODUCTION

Graphene is a one-atom-thick allotrope of carbon in the form of a two-dimensional, hexagonal lattice. Its peculiar band structure gives rise to many extraordinary electronic properties[1]. The valleys are the energetically degenerate but inequivalent local minima of the conduction band sitting at the corners of the Brillouin zone, called K and K'. Since the two valleys are far away from each other in momentum space, intervalley scattering is strongly suppressed, implying the potential use of the valley degree of freedom for electronic applications, referred to as valleytronics, in a way similar to the role of spin in spintronics.

In order to address valley, ultraclean disorder-free graphene is a prerequisite. Secondly, one needs a handle to control valley for generating and detecting the valley current. In this work, ballistic suspended graphene is employed and we aim to control valley by strain engineering.

II. METHOD

Exfoliated natural graphene itself is of high quality. However, the strong impurity scattering largely resulting from interactions with the underlying substrate limits the charge carrier mobility substantially. To circumvent this problem, an effective strategy is to suspend graphene above the substrate. Together with in-situ current annealing which cleans the resist residues from fabrication process, ultraclean suspended graphene has been developed, yielding very high mobilities and ballistic transport over micron distances. On this platform, various electron-optical effects have been observed through transport measurements in ballistic graphene p-n junctions such as Fabry-Perot interferences[2], magneto-conductance oscillations due to snake states[3], electrostatically defined waveguides[4] and gate tuneable beamsplitters[5].

The fabrication process of suspended graphene p-n junctions is schematically shown in Fig. 1a. Figure 1b is the false colored SEM image of the real device from a previous work at our group and Figure 1c shows a two-dimensional colour map of the electrical conductance as a function of the two gate voltages[3]. The regular Fabry-Perot oscillation patterns indicate the coherent ballistic

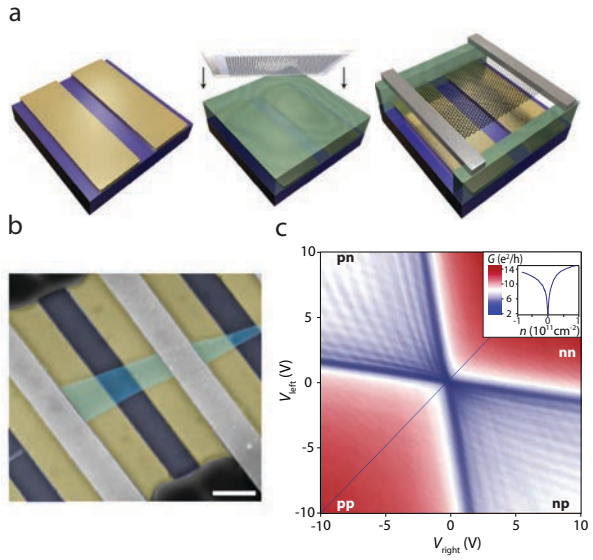

FIG. 1: **Fabrication process of suspended graphene. a**, Bottom gates realized by standard e-beam lithography on a Si substrate. Then a 700-nm-thick LOR (lift-off resist) layer is spin coated and exfoliated graphene is transferred on top with alignment to the bottom gates. After that, contacts to the graphene are realized by standard e-beam lithography and the device is suspended by selectively exposing the LOR and developing it[6]. **b**, The false colored SEM image of the finished device. The scale-bar corresponds to 1 μm. **c**, Two-terminal conductance as a function of left and right gate voltage shows regular Fabry-Perot oscillations at zero magnetic field. The inset reveals the narrow Dirac dip along the pp-nn diagonal (blue dashed line)[3].

electron motion.

It has been predicted that nonuniform strains can generate pseudomagnetic fields that act with opposite signs on the two different valleys in order to preserve time-reversal symmetry[7]. Two possible strain configurations has been proposed. One is to apply stresses with triangular symmetry[7] (see Fig. 2a) and the other is to bend the graphene into a circular arc[8] (see Fig. 2b). For the triangular geometry, we can perform valley Hall effect measurements in analogy to spin Hall effect, in which a Hall voltage will be built up from a valley polarized current. For the arc geometry, deviations from the quantum Hall patterns due to valley effects can be studied when a tunable strain pattern is applied in addition to a con-

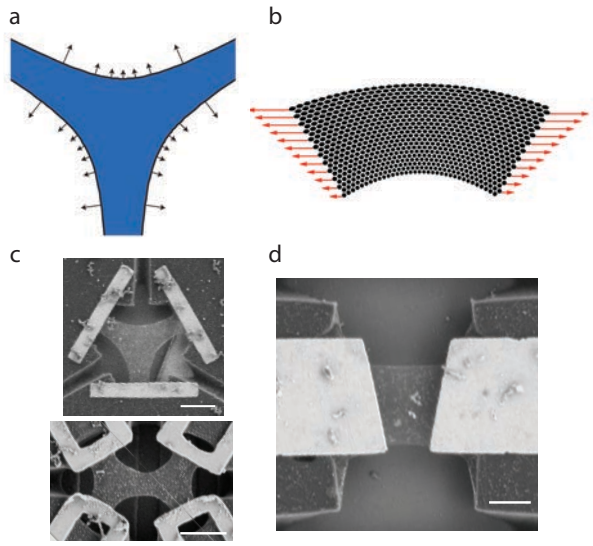

FIG. 2: **Two different strain configurations and corresponding SEM images of modified geometries. a**, A triangular shaped graphene sample with normal forces applied at the perimeter. The arrows indicates the required local stress[7]. **b**, Normal forces are applied at two opposite boundaries of a rectangular graphene sample and the length of the red arrows indicates the magnitude of the forces[8]. **c**, SEM images of a single triangle shaped graphene suspended symmetrically by three contacts (upper) and two triangular graphene connected together (lower). **d** SEM image of rectangular graphene with modified contacts. The scale-bars correspond to 1 μm.

stant magnetic field. However, both geometries are still experimentally challenging due to the complex fabrication process combined with non-trivial force patterns.

Instead of applying stresses perpendicular to the perimeter of the triangular geometry, we start with a simplified variation in which the three arms are fixed on the contacts (see Fig. 2c) and the graphene will be pulled down capacitively by using a global back gate. In order to detect the valley Hall voltage, we connect a second triangular graphene as shown in Fig. 2c. If a current is injected from the bottom-left contact, for example, electrons from one valley will go to the up-left contact while electrons from the other valley will bend to the right triangle going to the bottom-right contact resulting in a potential difference between the right two contacts. This potential difference can be detected by voltage measurements.

For the arc geometry, we design the contacts in a special shape so that an equivalent strain configuration can be achieved by pull the graphene uniaxially along the contact direction instead of bending it into a circular arc (see Fig. 2d). The simplified bending can be realized by break junction technology if we fabricate the device on a flexible substrate.

III. CONCLUSION

So far we have designed the device geometries and have done some fabrication tests. It turns out that the geometries can be well defined and the fabrication is very reproducible. However, the bottleneck of the fabrication process can be the current annealing. Since the doping of graphene is also controlled by the gate voltage, it will be very difficult to tune the doping and the strain separately. Currently we are optimizing the design and will try the first measurement soon.

Acknowledgments

This work is supported by the Swiss Nanoscience Institute (SNI).

[1] A. H. Castro Neto, F. Guinea, N. M. R. Peres, K. S. Novoselov, and A. K. Geim, *The electronic properties of graphene*, Rev. Mod. Phys. **81**, 109 (2009).

[2] P. Rickhaus, R. Maurand, M.-H. Liu, M. Weiss, K. Richter, and C. Schönenberger, *Ballistic interferences in suspended graphene*, Nat Commun **4**, (2013).

[3] P. Rickhaus, P. Makk, M.-H. Liu, E. Tvri, M. Weiss, R. Maurand, K. Richter, and C. Schönenberger, *Snake trajectories in ultraclean graphene p-n junctions*, Nat Commun **6**, (2015).

[4] P. Rickhaus, M.-H. Liu, P. Makk, R. Maurand, S. Hess, S. Zihlmann, M. Weiss, K. Richter, and C. Schönenberger, *Guiding of electrons in a few-mode ballistic graphene channel*, Nano Letters **15**, 5819 (2015).

[5] P. Rickhaus, P. Makk, M.-H. Liu, K. Richter, and C. Schönenberger, *Gate tuneable beamsplitter in ballistic graphene*, Applied Physics Letters **107**, 251901 (2015).

[6] R. Maurand, P. Rickhaus, P. Makk, S. Hess, E. Tvri, C. Handschin, M. Weiss, and C. Schönenberger, *Fabrication of ballistic suspended graphene with local-gating*, Carbon **79**, 486 (2014).

[7] F. Guinea, M. I. Katsnelson, and A. K. Geim, *Energy gaps and a zero-field quantum hall effect in graphene by strain engineering*, Nat Phys **6**, 30 (2010), ISSN 1745-2473.

[8] F. Guinea, A. K. Geim, M. I. Katsnelson, and K. S. Novoselov, *Generating quantizing pseudomagnetic fields by bending graphene ribbons*, Phys. Rev. B **81**, 035408 (2010).

24-Hour Long Relativistic Bit Commitment

Ephanielle Verbanis,[1] Raphal Houlmann,[1] Gianluca Boso,[1] Felix Bussières,[1] Anthony Martin,[1] and Hugo Zbinden[1]

[1] *Group of Applied Physics, University of Geneva, CH-1211 Geneva 4, Switzerland*

We report on the implementation of a 24-hour long relativistic bit commitment protocol using high-speed optical communication and FPGA-based processing between standard computers. The commitment time is more than six orders of magnitude longer than what was previously achieved with relativistic protocols.

I. INTRODUCTION

Bit commitment is a cryptographic task in which a party Alice commits a secret bit to another party Bob, and later reveals it at a time of her choosing. A bit-commitment protocol is secure against a cheating Alice if it guarantees that she cannot reveal, without being caught, another bit than the one she initially committed to an honest Bob. The protocol is also secure against a cheating Bob if it guarantees that no information about the committed bit can be obtained before Alice reveals her commitment. Perfectly secure bit commitment between two mistrustful parties is known to be impossible through the asynchronous exchange of classical or quantum messages[1]. Alternatively, a scheme in which each party is split in two agents was shown to be secure against classical attacks under the assumption that no communication was possible between agents of the same party[2]. To enforce the no-communication assumptions, relativistic constraints were proposed[3] and implemented in several classical and quantum protocols[4,5]. Proven secure against classical and quantum attacks, these protocols are however greatly limited by the time scale of the relativistic constraints for a single round of communication, i.e the commitment time is at most 21 ms if the agents are all located on Earth.

To overcome this limitation, a new scheme using multiple rounds of classical communication was proposed and shown to be secure against classical attacks[6]. This scheme can in principle allow an arbitrary long commitment time by periodically sustaining the carefully timed classical communication between the two parties. The security analysis in Ref.[6] derives the following bound on the probability ϵ of a successful cheating attempt:

$$\epsilon \lesssim 2^{-n/2^{(m-1)}}, \tag{1}$$

where n is the length of the bit string communicated between the agents of Bob and Alice at each round of the protocol, and $m+1$ is the number of rounds[6]. To keep $\epsilon \ll 1$, the length of the messages n has to grow exponentially with the number of rounds. Therefore, an arbitrarily long commitment is in practice impossible to achieve. The implementation in Ref.[6] was limited to 6 rounds, yielding a 2 ms bit-commitment with agents separated by 131 km, i.e. between Geneva and Bern. This could have been extended to a maximal value of 212 ms using antipodal locations on earth.

Interestingly, the security bound (1) was later improved significantly in two independent proofs considering classical attacks[7,8]. In both cases, the bound is linear in the number of rounds. For instance, the bound in[7] is

$$\epsilon \leq m\, 2^{(-n+3)/2}. \tag{2}$$

These results open the way towards the implementation of much longer commitments.

II. PROTOCOL

The multi-round protocol contains a *commit*, *sustain* and *reveal* phases. In the commit phase, the first agent of Bob B_1 sends a random n-bit string x_1 to the first agent of Alice A_1, who replies with the string $y_1 = a_1$ to commit the bit 0, or $y_1 = x_1 \oplus a_1$ to commit the bit 1. Here, "$\oplus$" is the bitwise XOR operation. The second agent B_2 starts the sustain phase by sending x_2 to agent A_2, who then returns $y_2 = (x_2 \cdot a_1) \oplus a_2$, where "$\cdot$" is the multiplication in the Galois field $\mathbb{F}_{2^n}$. The third round is again between B_1 and A_1, the fourth one between B_2 and A_2, and so on. At the k^{th} round, the agent B_i sends x_k and A_i replies $y_k = (x_k \cdot a_{k-1}) \oplus a_k$, for $2 \leq k \leq m$. Finally, to open the commitment, the following A_i sends her commitment and $y_{m+1} = a_m$ to the corresponding B_i. With the set of questions x_i, the set of answers y_i and the last string a_m, Bob can compute all the previous a_k and verify that the bit he received during the reveal phase is the one committed by the first answer y_1 of agent A_1.

The distance L between the agents of Bob is chosen such that by carefully timing the communication between A_i and B_i, the security can be guaranteed. For our analysis, we consider a situation where Alice is allowed to place her agent A_i at a maximum distance l_i from their corresponding B_i, as shown in Fig. 1(a). To ensure that no communication is possible between the two agents of Alice, we must impose the two following constraints: A_i should answer before a time τ_i from the start of the corresponding round, or the protocol is aborted, and agent B_i should start the round $t_L - (\tau_i + t_M)$ time after the start of the previous round, where t_L is the time taken by light to travel the distance L and t_M is a chosen time margin. The security is guaranteed if t_M is much greater than the timing uncertainties. Fig. 1(b) shows the relativistic constraints in the case where the agents of Alice are

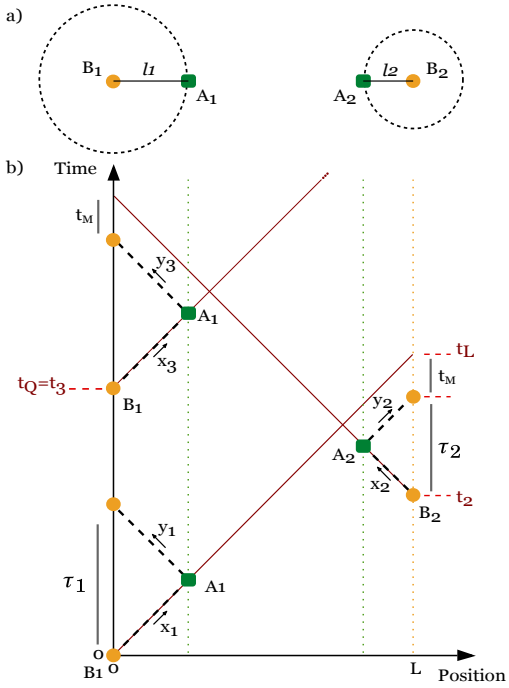

FIG. 1: (a) Positioning of the agents of Bob and Alice. (b) Space-time diagram of the multi-round protocol showing the relativistic constraints for the spatial configuration where A_i is placed at the distance limit l_i.

placed at the maximum allowed distance l_i. The number of rounds is then set by the spatial configuration, the chosen time margin t_M and the time of commitment T.

III. EXPERIMENT

Each agent has a computer with a field-programmable gate array (FPGA) card installed to perform the computing tasks of the multi-round protocol. To ensure an accurate timing of exchange between A_i and B_i, the FPGAs of Bob's agents are synchronized using local clocks disciplined by a Global Positioning System (GPS) receiver. The uncertainty of this system is sufficiently small to ensure that the relativistic constraints are satisfied. The agents A_1 and B_1 are located at the Group of Applied Physics (GAP) of the University of Geneva, while agents A_2 and B_2 are placed 7.0 km away from the GAP. An optical signal in straight line would take 23.3 μs to cover this distance. With the various latencies in our system and the time needed to compute y_k, we can complete a round in 1.8 μs (for $n = 128$). To account for possible fluctuations in the duration and timing of the rounds, we impose that the agents of Alice answer within 3 μs from the start of the round and take a margin t_M of 3.3 μs, such that each round starts 6.3 μs before the earliest arrival time of the information from the previous round. We performed a 24 h bit commitment with a security parameter ϵ of 7.8×10^{-10}, which required 5×10^9 rounds, a total of 162 GB of data and an average transfer rate of 0.5 MBps.

IV. CONCLUSION

A 24-hours long bit commitment protocol was performed over a 7 km distance between the two locations of the agents. It could in practice be achieved for a large range of spatial configurations and longer commitment times, notably for situations with large L, which require less resources. The new bound (2) allows the implementation of long bit commitments without the need of large computing power and for realistic situations. This is an important step towards applications such as secure voting[9].

Acknowledgments

We thank Jedrzej Kaniewski for helpful discussions. This work was supported financially by the Swiss NCCR-QSIT.

[1] D. Mayers, *Unconditionally secure quantum bit commitment is impossible*, Phys. Rev. Lett. **78**, 3414 (1997).
[2] M. Ben-Or, S. Goldwasser, J. Kilian, and A. Wigderson, in *Proceedings of the Twentieth Annual ACM Symposium on Theory of Computing* (1988), STOC '88, pp. 113–131, ISBN 0-89791-264-0.
[3] A. Kent, *Unconditionally secure bit commitment*, Phys. Rev. Lett. **83**, 1447 (1999).
[4] T. Lunghi, J. Kaniewski, F. Bussières, R. Houlmann, M. Tomamichel, A. Kent, N. Gisin, S. Wehner, and H. Zbinden, *Experimental bit commitment based on quantum communication and special relativity*, Phys. Rev. Lett. **111**, 180504 (2013).
[5] Y. Liu, Y. Cao, M. Curty, S.-K. Liao, J. Wang, K. Cui, Y.-H. Li, Z.-H. Lin, Q.-C. Sun, D.-D. Li, et al., *Experimental unconditionally secure bit commitment*, Phys. Rev. Lett. **112**, 010504 (2014).
[6] T. Lunghi, J. Kaniewski, F. Bussières, R. Houlmann, M. Tomamichel, S. Wehner, and H. Zbinden, *Practical relativistic bit commitment*, Phys. Rev. Lett. **115**, 030502 (2015).
[7] K. Chakraborty, A. Chailloux, and A. Leverrier, *Arbitrarily long relativistic bit commitment*, Phys. Rev. Lett. **115**, 250501 (2015).
[8] S. Fehr and M. Fillinger, *On the composition of two-prover commitments, and applications to multi-round relativistic commitments*, arXiv preprint arXiv:1507.00240 (2015).
[9] A. Broadbent and A. Tapp, in *Proceedings of the IAVoSS Workshop On Trustworthy Elections* (2008).

A stabilised in-vacuum transfer cavity system

Kilian Sandholzer,[1] Andrea Morales,[1] Julian Léonard,[1] Philip Zupancic,[1] Tilman Esslinger,[1] and Tobias Donner[1]

[1]*Institute of Quantum Electronics, Otto-Stern-Weg 1, HPF D4, 8093 Zurich, Switzerland*

The IMPACT experiment explores the field of cavity quantum electrodynamic and ultra-cold atoms by coupling a ^{87}Rb Bose-Einstein condensate to two crossed modes of high finesse optical resonators. The atoms and resonators are manipulated by a 785 nm and a 830 nm laser which are both locked on a transfer cavity to stabilise the relative frequency. We built a new in-vacuum transfer cavity system to ensure relative frequency stability below 100 kHz. It is shown that a laser locked onto the new transfer cavity achieves a linewidth below 20 kHz for timescales 130 μs to 1 ms and 86 kHz for 8 ms by a heterodyne measurement of three comparably cavity-narrowed lasers.

I. INTRODUCTION

The combination of ultra-cold atomic gases and optical potentials has opened up a new way to study condensed matter problems, and allowed for example the exploration of the Hubbard model[1]. In these experiments, static optical lattices are employed to create a periodic potential for the atoms.
Solid state systems differ with respect to this case in the sense that the transition to a new phase usually implies a rearrangement of the atoms to a new potential landscape that is created dynamically, and is not imposed from the outside. This type of transitions can be realised with cold gases by coupling a BEC to the mode of an high-finesse optical resonator via a transverse pump laser beam[2]. The transverse pump is far detuned from atomic resonances but closely detuned to a cavity resonance. For strong enough powers of the transverse pump, a superradiant scattering of light off the atoms into the cavity mode occurs, creating an emergent potential landscape with effective long-range interactions in which the cloud can organise spatially.
The addition of static lattice beams to this setup has allowed to study the competition between short and long-range interactions[3], extending further the concept of the Hubbard model to account for dynamical ordering of the atoms.

II. THE IMPACT EXPERIMENT

In the IMPACT experiment, an ultra-cold cloud of ^{87}Rb atoms is cooled to degeneracy and the BEC is coupled to the fundamental modes of two high-finesse optical resonators (Science cavities), crossing under an angle of 60 degrees. The cavity lengths are stabilised with 830 nm laser light. A transverse pump standing wave laser beam at 785 nm pumps the BEC transversally to the cavity axes. The emerging interference pattern of the cavity light fields and the transverse pump can be shifted by changing the position of the retro-reflecting mirror. In this way different lattice geometries for the self-organised phases of the atoms can be realised. In order to perform these experiments we need to ensure good relative stability between the 830 nm and 785 nm lasers well below the cavity linewidths. For the current Science cavities this means a stability well below 100 kHz.

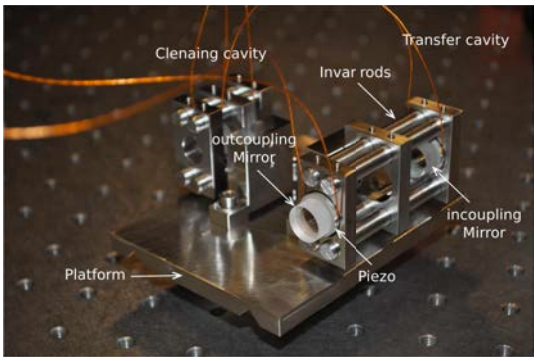

FIG. 1: Picture of the cavities on the platform. The transfer cavity is at the front, the cleaning cavity at the back. The mirror spacer is made of Invar which has a very low thermal expansion coefficient.

III. DESIGN OF THE NEW TRANSFER CAVITY SYSTEM

The system shown in figure 1 consists of a cleaning cavity acting as a filter for the 785 nm light and the transfer cavity hosted in a vacuum chamber. The mirrors of the transfer cavity are glued on piezoelectric elements to tune the length.
The laser stabilisation setup of the IMPACT lab uses a transfer cavity concept, adopted from the previous cavity experiment. Both, the 830 nm and the 785 nm laser are locked to this transfer cavity to fix their relative frequency. The science cavities are then stabilised in length with the 830 nm light allowing both lasers to be resonant with the Science cavities at the same time. Nevertheless, since the linewidth of our Science cavities is roughly one order of magnitude smaller than the previous experiment, the transfer cavity concept is more susceptible to fluctuations of environmental parameters. Indeed any change in temperature, pressure or relative humidity of the air contributes with a small correction to the change of the index of refraction of air. This in return creates a differential drift in the frequen-

cies of the 830 nm and 785 nm lasers that can be estimated to $\delta\nu = -113$ kHz/mbar, 370 kHz/°C and -7 kHz/% humidity[4]. These fluctuations can be prevented by putting the transfer cavity in an evacuated chamber. Thus, we achieved a pressure of $5 \cdot 10^{-7}$ mbar reached by using an ion pump. The space between the mirrors is kept fixed by Invar rods which have a very low thermal expansion coefficient to further decouple from fluctuations.

IV. CAVITY-NARROWED LASER LINEWIDTH

A free running laser optimally operates at one frequency but several noise processes will induce fluctuations on this frequency broadening the spectral peak. Nevertheless, the frequency of a laser can be controlled and a feedback technique like the Pound-Drever-Hall-lock[5] allows to stabilise the laser frequency onto an optical cavity. The natural way of measuring frequencies of light is to mix down the signal to frequencies on the order of MHz where they can be conveniently detected and processed via electronic devices. This mix down can

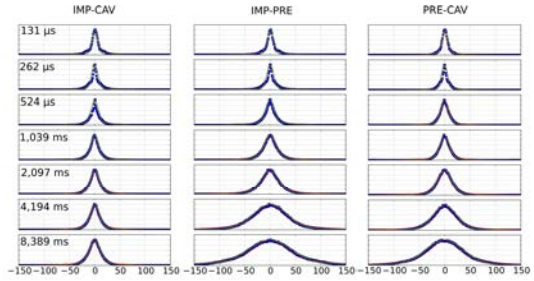

FIG. 2: The normalised spectral peaks of the beat notes between the laser IMP, CAV and PRE are shown for different recording times t_{gate}. The left column shows the IMP-CAV beating, the middle one the IMP-PRE and the right one the PRE-CAV. The shown spectra are averaged over 1000 to 2000 single spectra simulating an effective offset lock between the two beating lasers.

be achieved by a heterodyne measurement. Two laser beams are overlapped using a beam splitter and their beat note is recorded on a fast photodiode (PD).

If we beat three different lasers, all with each other, we can write down a linear system of equations for the three unknown linewidths assuming they are not correlated[6]. Although the linewidths do not have to be known a priori they should be of the same order of magnitude such that the frequency jittering of the broadest laser does not completely wash out the other narrower linewidths. What we have to assume is a certain line shape of the lasers that we then fit to the beat spectra to obtain the linewidth. We fit a Voigt profile to the beat note spectra shown in figure 2. An averaging process simulating an offset-lock between the two lasers is used to exclude relative frequency fluctuations due to cavity drifts on timescales longer than the recording time of the spectra. In figure 3 the single laser linewidths are shown. The laser labelled PRE is the one locked on the new transfer cavity system, the one labelled IMP is locked on the current transfer cavity setup of the IMPACT lab and the one labelled CAV is locked on the transfer cavity of the CAVITY lab. Below 1 ms, all three lasers have a linewidth below 20 kHz whereas for 8 ms the PRE-laser linewidth rises to 86 kHz. We attribute this to the lower bandwidth of the feedback system of the PRE-laser compared to IMP and CAV and are confident that the linewidth is further reduced if the new system is integrated in the IMPACT experiment.

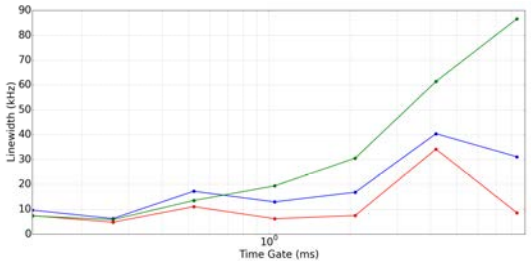

FIG. 3: The linewidth of the single lasers IMP (blue), CAV (red) and PRE (gree) are extracted applying the three-cornered-hat method to the linewidths obtain from a beat measurement between the single lasers. A Voigt profile was fitted to the averaged PSD of the beat note spectra to extract the beat linewidths. The linewidths are calculated for different recording times t_{gate} of the spectrum.

[1] M. Greiner, O. Mandel, T. Esslinger, T. W. Hänsch, and I. Bloch, *Quantum phase transition from a superfluid to a mott insulator in a gas of ultracold atoms*, Nature **415**, 39 (2002).

[2] K. Baumann, C. Guerlin, F. Brennecke, and T. Esslinger, *Dicke quantum phase transition with a superfluid gas in an optical cavity*, Nature **464**, 1301 (2010).

[3] R. Landig, L. Hruby, N. Dogra, M. Landini, R. Mottl, T. Donner, and T. Esslinger, *Quantum phases from competing short- and long-range interactions in an optical lattice*, Nature **532**, 476 (2016).

[4] S. Uetake, K. Matsubara, H. Ito, K. Hayasaka, and M. Hosokawa, *Frequency stability measurement of a transfer-cavity-stabilized diode laser by using an optical frequency comb*, Appl. Phys. B **97**, 413 (2009).

[5] E. D. Black, *An introduction to pound-drever-hall laser frequency stabilization*, American Journal of Physics **69**, 79 (2001).

[6] J. E. Gray and D. W. Allan, in *Proceedings of the 28th Annual Symposium on Frequency Control* (1974), pp. 243–246.

Superconducting nanowire single photon detectors based on amorphous superconductors

Misael Caloz,[1] Boris Korzh,[1] Félix Bussières,[1] Nuala Timoney,[1]
Markus Weiss,[2] Richard Warburton,[2] and Hugo Zbinden[1]
[1]*GAP Quantum Technologies, University of Geneva, Switzerland*
[2]*Nano-photonics group, University of Basel, Switzerland*

We present progress on the development of single photon detectors based on superconducting nanowires made from amorphous MoSi. We also experimentally investigate the nanoscale detection mechanism in MoSi nanowires.

I. INTRODUCTION

Superconducting nanowire single photon detectors (SNSPDs) constitute a key technology for the development of quantum communication and computation. Their low dead time and dark count rate, combined with a high efficiency and small jitter favour the use of this technology in applications such as Quantum Key Distribution (QKD), quantum optics and communication[1], and long-distance ground-to-space optical communications[2].

Amorphous materials such as WSi and MoSi are particularly desirable for the fabrication of SNSPDs due to their high degree of homogeneity and uniformity over large areas. Due to the lack of a well-defined crystal structure, amorphous superconductors can be deposited on virtually any substrate without significant degradation in material properties. Thus, SNSPDs fabricated from these materials can easily be embedded inside of a dielectric optical stack to enhance absorption at a particular wavelength. High efficiencies have been reported with WSi (90%)[3] and MoSi (87%)[4].

In this work, we present the progress on the development of single photon detectors based on superconducting nanowires made from amorphous MoSi as well as the investigation of the nanoscale detection mechanism in MoSi nanowire SNSPDs.

II. EXPERIMENT

A. Nanofabrication

The nanofabrication of the SNSPDs is performed in the clean room facility in Ecole polytechnique fédérale de Lausanne (EPFL).

The fabrication process begins with the deposition of aluminium mirrors on a 4 inch Si wafer. Then a deposition of 200 nm of SiO_2. The 6.5 nm-thick $Mo_{0.8}Si_{0.2}$ film is then deposited in University of Basel by sputtering and capped with 2 nm of amorphous Si to prevent oxidation. After etching a 20 μm-wide strip between the gold contact pads, electron beam lithography and etching plasma are used to define the nanowire meanders. A keyhole shape is then etched through the Si wafer around each SNSPD, which can then be removed from the wafer and self-aligned to a single-mode optical fiber to within $\pm$ 3 μm. Each nanowire meander covers an active area of 16 μm $\times$ 16 μm which is larger than the 10 μm mode-field diameter of a standard single-mode fiber to allow for misalignment.

B. Setup

A 1550 nm CW laser attenuated down to a mean photon number of $\sim$ 100,000 photons/s is used for the measurements at 0.75 K. The calibration of the input power to the SNSPD is performed using power meter calibrated at the Swiss Federal Institute of Metrology (METAS). The system detection efficiency (SDE) is measured after maximizing the detector counts as a function of the polarization of the incident light.

The investigation of the nanoscale detection mechanism in the nanowire is carried out by measuring the count rate response of the detector as a function of the wavelength of the incident photons. This measurement is realized by using a well calibrated monochromator as the photon source. The grating range goes from $\lambda = 600$ nm to 2100 nm. Other devices with different nanowire width and fill factor have also been examined. Thus, the energy-current relation obtained is then confronted with different theoretical models.

III. RESULTS

Second generation devices have achieved a saturated internal efficiency from visible to near-infrared wavelengths, which is the first requirement for high overall system efficiency. So far, at 1550 nm a system detection efficiency of 65% has been achieved at 0.75 K. The Figure 1 shows the SDE and dark count rate (DCR) as a function of bias current.

The Figure 2 shows the count rate response of the detector as a function of the wavelength of the incident photons. The energy-current relation can then be extracted from this graphic.

IV. DISCUSSION

Subsequent generations are aimed at increasing the overall absorption efficiency by embedding the nanowires within an optical stack, optimized for a specific wavelength. In addition, we are optimizing the superconducting film thickness to increase the operating temperature up to 2.5 K. Other device designs, different to simple nanowire meanders, are also being studied with the aim of increasing the maximum count rate of the detectors as well as improving temporal jitter.

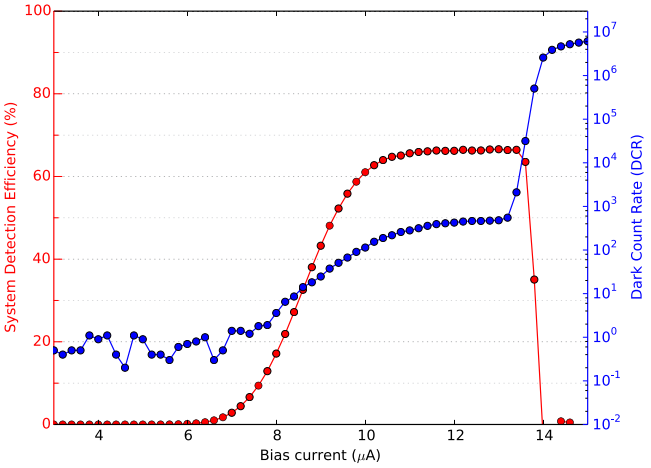

FIG. 1: Efficiency measurement with a detector with half cavity, 150 nm wide nanowire and 1/2 fill factor. SDE (red/left side) and DCR (blue/right side) are plotted as a function of the bias current in μA.

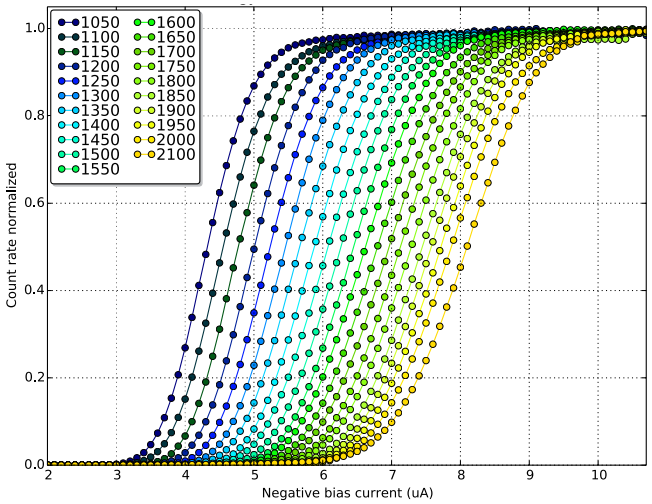

FIG. 2: Normalized count rate response of a SNSPD as a function of the bias current for different incident photon wavelengths in nanometers. (The wavelength increases from left to right of the graphic.)

Acknowledgments

We acknowledge Stefano Gariglio and Claudio Barreiro for useful discussions. The Swiss Federal Institute of Metrology (METAS) for the calibration of the power meters. And finally the Swiss National Science Foundation.

[1] C. Zinoni, B. Alloing, L. Li, F. Marsili, A. Fiore, L. Lunghi, A. Gerardino, Y. B. Vakhtomin, K. Smirnov, and G. Goltsman, *Single-photon experiments at telecommunication wavelengths using nanowire superconducting detectors*, Appl. Phys. Lett. **91**, 031106 (2007).

[2] M. E. Grein, A. J. Kerman, E. A. Dauler, O. Shatrovoy, R. J. Molnar, D. Rosenberg, J. Yoon, C. E. DeVoe, D. V. Murphy, B. S. Robinson, et al., *Design of a ground-based optical receiver for the lunar laser communications demonstration*, Int. Conf. Sp. Opt. Syst. Appl. **78** (2011).

[3] F. Marsili, V. B. Verma, J. A. Stern, S. Harrington, A. E. Lita, T. Gerrits, I. Vayshenker, B. Baek, M. D. Shaw, R. P. Mirin, et al., *Detecting single infrared photons with 93% system efficiency*, Nat. Photonics **7**, 210 (2013).

[4] V. B. Verma, B. Korzh, F. Bussières, R. D. Horansky, S. D. Dyer, A. E. Lita, I. Vayshenker, F. Marsili, M. D. Shaw, H. Zbinden, et al., *High-efficiency superconducting nanowire single-photon detectors fabricated from MoSi thin-films*, Opt. Express **23**, 33792 (2015).

Electronic Transport in the 2D Topological Insulator Candidate InAs/GaSb

Christopher Mittag,[1] Susanne Müller,[1] Matija Karalic,[1] Thomas Tschirky,[1] Werner Wegscheider,[1] Thomas Ihn,[1] and Klaus Ensslin[1]

[1]*Solid State Physics Laboratory, ETH Zürich, 8093 Zürich, Switzerland*

We study the electronic transport in InAs/GaSb double quantum wells, a predicted 2D topological insulator. Nonlocal measurements are conducted in order to probe gapless edge modes at zero magnetic field. Plateau values do not coincide with theoretical expectations, reinforcing the current debate about the nature of edge conduction in the experimental community. In magnetotransport measurements, anomalies in the Landau level spectrum are observed, possibly originating from the nontrivial band structure and thereby serving as a new approach of determining the topological phase.

I. INTRODUCTION

A topological insulator is a state of matter that insulates in the bulk and contains gapless edge modes, which are protected from disorder and small perturbations. This protection can be described by a topological invariant corresponding to a certain symmetry of the system. The origin is related to an inverted band structure. When these bands hybridize, they open a topological band gap. In two dimensions, a topological insulator is known as quantum spin Hall insulator and is characterized by two one-dimensional, counterpropagating, spin-momentum-locked (helical) edge modes. Energetically the edge modes exist in the band gap of the bulk. Shortly after theoretical prediction[1] and experimental realization[2] of this effect in HgTe/CdTe quantum wells, InAs/GaSb double quantum wells have been proposed as an alternative material[3]. The advantage of this platform is electrical tunablity between topologically insulating and trivially insulating phases through the application of voltages to a top and a back gate. Therefore, this material has recently attracted the interest of numerous research groups[4–6]. However, thus far it remains unclear whether the effects observed and published actually correspond to a topological insulator or whether remaining trivial edge conduction effects dominate in the experiment[7]. Our current work therefore focuses on investigating the nature of edge conduction and on isolating the signatures of a topological phase in InAs/GaSb double quantum wells.

II. FABRICATION AND EXPERIMENTAL METHODS

Our devices containing an InAs and GaSb quantum well of varying thicknesses sandwiched by two AlGaSb barriers are grown on a Te-doped GaSb substrate by molecular beam epitaxy. A Hall bar mesa is defined by wet etching, covered by a SiN_x dielectric layer and a metal top gate. For ohmic contacts, holes are lithographically defined, etched, and filled with metal as a last step in order to avoid a short with the back gate during elevated deposition temperatures. Measurements

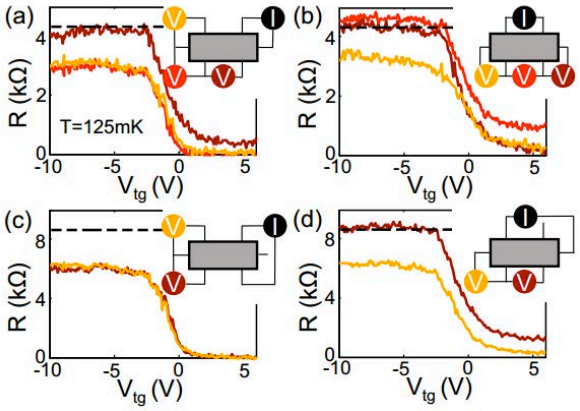

FIG. 1: Nonlocal measurements in varying four-terminal configurations (a)-(d) as schematically depicted in the upper right corner of each plot. The dashed line indicates theoretically expected plateau values from the Landauer-Büttiker formalism.

were performed with standard a.c. lock-in techniques in a He^4 cryostat at $T = 1.3\,K$ and a He^3/He^4 dilution refrigerator at $T = 125\,mK$.

III. RESULTS

In order to investigate edge conduction, it is important to introduce the concepts of local and nonlocal transport. In the case of diffusive bulk conduction, current flows only between the biased and grounded contacts. Voltage signals on contacts that are not lined up along the current path are exponentially suppressed with distance. This situation can be described with a local resistivity and is therefore called "local transport". In contrast, when the bulk is insulating and current flows along the edges in two dimensions, voltages can be picked up at any contacts along the edges of the sample. The resistance cannot be described by a local resistivity, but the theoretically expected values of four-terminal resistances can be calculated within the non-local Landauer-Büttiker theory assuming helical one-dimensional edge channels.

This is shown in Fig. 1 for a number of different mea-

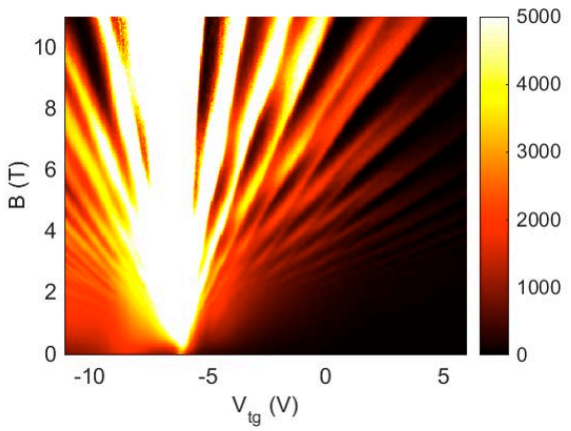

FIG. 2: Landau fan of an inverted InAs/GaSb double quantum well sample. The color scale shows the longitudinal resistance in units Ω. Regions of high and low resistance as a function of top gate voltage and applied magnetic field can be identified and differ from a regular Landau fan in the clearly visible periodic opening and closing of gaps.

surement configurations. One can clearly see that for $V_{tg} > 0.5\,\mathrm{V}$, which corresponds to the region where the Fermi level is in the conduction band above the topological gap, the nonlocal signal is vanishingly small. When the gate voltage is used to tune the Fermi level in this gap, the nonlocal signal increases and saturates at a plateau value, which indicates conductive edge states. The dashed line in each plot shows the theoretically expected plateau value, which does usually not coincide with the experimental data. The reasons for this mismatch could be residual bulk conductivity or trivial edge conduction leading to alternative conductive paths and backscattering between the helical edge channels.

When applying a perpendicular magnetic field and measuring the quantum Hall effect in a sample of higher mobility and with AlGaSb barriers, we find Landau levels of even and odd filling factors. The resulting Landau fan, measured by sweeping the top gate voltage and different magnetic field values, can be seen in Fig. 2.

It exhibits an unusual modulation of energy gaps between Landau levels, akin to a periodic opening and closing of gaps. An exact theoretical understanding of this phenomenon has yet to be achieved. Preliminary discussions and experiments suggest that it is directly connected to the inverted band structure of our material, and thereby its topological properties. This assumption is supported by data of the same measurements on samples that have a non-inverted band structure. These samples contain either slightly wider InAs quantum wells or only a single InAs and no GaSb quantum well, for all of which these conspicuous features in the Landau level structure was not observed. Measurements of temperature dependence and behavior in a parallel magnetic field of the resistance peak for the different samples as well as collaboration with theoreticians are undertaken in order to thoroughly understand these data and possibly use Landau level spectroscopy as a direct experimental characterization of topological band structure.

IV. OUTLOOK

The quantum spin Hall effect and thereby the topologically insulating nature of InAs/GaSb double quantum wells remain to be unambiguously shown. Our future work will focus on determining more precisely the exact nature of edge conduction and eliminating trivial edge conduction as far as possible. Additionally, the origin of the unusual Landau level spectrum and its implications on the topology of the system shall be investigated. Spin-sensitive measurements could at a later stage resolve the helical edge channels and thereby open possible further applications within the fields of topological quantum computation or spintronics.

Acknowledgments

We acknowledge the Swiss National Science Foundation for financial support via NCCR QSIT (Quantum Science and Technology) and technical support by P. Märki.

[1] B. A. Bernevig, T. L. Hughes, and S.-C. Zhang, *Quantum Spin Hall Effect and Topological Phase Transition in HgTe Quantum Wells*, Science **314** (2006).

[2] M. König, S. Wiedemann, C. Brüne, A. Roth, H. Buhmann, L. W. Molenkamp, X.-L. Qi, and S.-C. Zhang, *Quantum Spin Hall Insulator State in HgTe Quantum Wells*, Science **318** (2007).

[3] C. Liu, T. L. Hughes, X.-L. Qi, K. Wang, and S.-C. Zhang, *Quantum Spin Hall Effect in Inverted Type-II Semiconductors*, Phys. Rev. Lett. **100** (2008).

[4] I. Knez, R.-R. Du, and G. Sullivan, *Evidence for Helical Edge Modes in Inverted InAs/GaSb Quantum Wells*, Phys. Rev. Lett. **107** (2011).

[5] K. Suzuki, Y. Harada, K. Onomitsu, and K. Muraki, *Edge Channel Transport in the InAs/GaSb Topological Insulating Phase*, Phys. Rev. B **87** (2013).

[6] S. Müller, A. N. Pal, M. Karalic, T. Tschirky, C. Charpentier, W. Wegscheider, K. Ensslin, and T. Ihn, *Nonlocal Transport via Edge States in InAs/GaSb Coupled Quantum Wells*, Phys. Rev. B **92** (2015).

[7] F. Nichele, H. J. Suominen, M. Kjaergaard, C. M. Marcus, E. Sajadi, J. A. Folk, F. Qu, A. J. A. Beukman, F. K. de Vries, J. van Veen, et al., *Edge Transport in the Trivial Phase of InAs/GaSb* (2015), arXiv:1511.01728.

Quantum phases emerging from competing short- and long-range interactions in an optical lattice.

K.E. Roux,[1] L. Hruby,[1] N. Dogra,[1] M. Landini,[1] R. Landig,[1] Tobias Donner,[1] and Tilman Esslinger[1]

[1] *Quantum optics group, Institute of Quantum Electronics, ETH-Hönggerberg, CH-8093, Zürich, Switzerland*

We experimentally realize a two dimensional bosonic lattice model with competing short- and infinite-range interactions. We map out the phase diagram consisting of a superfluid, a supersolid, a Mott insulator and a charge density wave phase. When probing the phase transition between the Mott insulator and the charge density wave in real-time, we discover a behavior characteristic of a first order phase transition. Short-range interactions in our system are controlled via an optical square lattice, while the infinite-range interaction potential stems from the coupling of the external degree of freedom of the atoms to the single mode of an optical cavity.

I. INTRODUCTION

Since the end of the 20th century the field of ultracold atomic physics has developed a large number of techniques in order to get perfect control of all the experimental parameters like temperature, atom numbers or interactions. The field of ultracold atoms has proven to be a versatile and well-suited platform for the simulation and exploration of complex many-body phenomena. The studied systems are highly pure with a large degree of control on the various parameters and a nearly perfect decoupling from the environment. As a paramount example, the imposition of optical lattice potentials on ultracold atoms has enabled the simulation of condensed matter systems with both Bosonic and Fermionic analogues, contributing to our understanding of the quantum many-body physics as it was proposed by R. Feynman in 1982.

The competition between interactions acting on different length scales lies at the core of a variety of processes leading to structure formation in nature from the folding mechanisms of proteins to the appearance of stripe phases in quantum matter Theoretical characterization of such emerging structures is often exceedingly challenging even if simple toy models are used. A complementary approach to gain insights into complex phenomena has been advanced for quantum matter, where simulation experiments with ultracold atoms are carried out.

With the achievement of Bose-Einstein condensation in 1995[12], which was made possible by the invention of efficient ways to cool dilute atomic gases - above all laser cooling in the 1980s and evaporative cooling in the 1990s[3], the foundation for the Bose-Hubbard model was laid. Its first experimental realization alongside with the observation of the superfluid to Mott insulator phase transition in 2001[4] presented an impressive benchmark result. In particular, it was the first experiment reaching the strongly correlated regime, where the physics is dominated by interaction induced correlations. By cooling bosonic atoms to ultralow temperatures, where they condense into a macroscopically occupied ground state, and loading them into optical lattices, a nearly perfect Hubbard model can be realized where kinetic energy and short-range interactions are the dominant interactions.

II. EXPERIMENT AND RESULTS

Our system is based on an atomic quantum gas trapped in an optical lattice inside a high finesse optical cavity. The cavity mediates an infinite range interaction between atoms induced by the photons scattered into the cavity by the atomic cloud. Our setup allows us to chose the strength of the different interactions. The ratio between the three kinds of interactions: one-site interaction, kinetic and long-range interaction is controlled by means of the optical lattice depth and the detuning of the transverse optical lattice. This competition between the different interaction length scales leads to structural phase transitions characterized by the spatial coherence of the atomic cloud and the light emitted by atoms through the cavity.

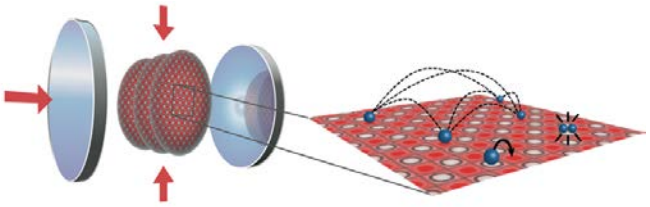

FIG. 1: Illustrations of the experimental scheme realising a lattice model with on-site and infinite-range interactions. A stack of 2D systems along the y-axis is loaded into a 2D optical lattice (red arrows). The cavity induces atom-atom interactions of infinite range[5]. Illustration of the competing energy scales: Tunneling t, on-site interactions U_s and long-range interactions U_l.

Ultracold atoms are mostly limited to short-range collisional interactions, while longer ranged interactions have proven to be difficult to implement so far. Here we experimentally realize a bosonic lattice model with competing short- and infinite-range interactions, and observe

the appearance of four distinct phases - a superfluid, a supersolid, a Mott insulator and a charge density wave[6] as shown in Fig. 2.

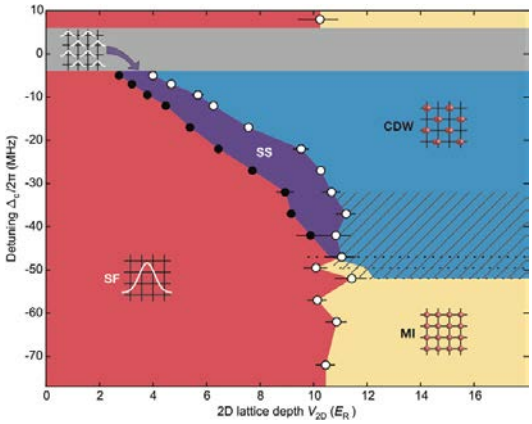

FIG. 2: The four phases are indicated by different colors: SF (red), SS (violet), CDW (blue), MI (yellow). Their density distributions are schematically illustrated.

The phase coherence as observed in time of flight pictures and the even-odd imbalance obtained from the light field leaking out of the cavity allow us to map out the different phases and study the according phase transitions between them. When probing the transition between the Mott insulator and the charge density wave, we discovered a behavior characteristic of a first order phase transition.

III. OUTLOOK

Our current interest is focused on the study and characterization of the transition from the Mott insulator regime to the charge density wave phase. We perform a frequency scan of the transverse lattice and study the light field building up. This transition shows a very interesting feature which could be related to a first order phase transition due to the presence of metastable states. The study of this transition dynamics requires to trap atoms in the lattice for several tens of milliseconds without increasing losses or heating the cloud. In order to observe this transition we have improved technical features to achieve the required heating rates to characterize this phase transition.

Acknowledgments

We thank U. Bissbort, G. Graf, S. Huber, G. Morigi, L. Pollet and H. Ritsch for discussions and F. Brennecke for contributions in the early design phase of the experiment. Financial funding from Synthetic Quantum Many-Body Systems (European Research Council advanced grant), the EU Collaborative Project TherMiQ (Grant Agreement 618074) and the DACH project 'Quantum Crystals of Matter and Light'.

[1] K. B. Davis, M. O. Mewes, M. R. Andrews, N. J. van Druten, D. S. Durfee, D. M. Kurn, and W. Ketterle, *Bose-einstein condensation in a gas of sodium atoms.*, Physical Review Letters **75**, 3969 (1995).

[2] M. H. Anderson, J. R. Ensher, M. R. Matthews, C. E. Wieman, and E. A. Cornell, *Observation of bose-einstein condensation in a dilute atomic vapor.*, Science **269**, 198 (1995).

[3] C. S. Adams, H. J. Lee, N. Davidson, M. Kasevich, and S. Chu, *Evaporative cooling in a crossed dipole trap*, Physical Review Letters **74**, 3577 (1995).

[4] M. Greiner, I. Bloch, O. Mandel, T. W. Hansch, and T. Esslinger, *Exploring phase coherence in a 2d lattice of bose-einstein condensates.*, Physical Review Letters **87**, 160405 (2001).

[5] R. Landig, F. Brennecke, R. Mottl, T. Donner, and T. Esslinger, *Measuring the dynamic structure factor of a quantum gas undergoing a structural phase transition.*, Nature Communications **6**, 7046 (2015).

[6] R. Landig, L. Hruby, N. Dogra, M. Landini, T. Donner, and T. Esslinger, *Quantum phases from competing short- and long-range interactions in an optical lattice.*, Nature **532**, 476 (2016).

Macroscopic quantum measurements: In what direction does a magnet point?

Marc-Olivier Renou,[1] Tomer Jack Barnea,[1] Florian Fröwis,[1] and Nicolas Gisin[1]

[1] *Group of Applied Physics, University of Geneva, 1211 Geneva 4, Switzerland*

We introduce the concept of macroscopic quantum measurement, that is, a quantum formalism describing the measurements we perform continuously in our everyday life; for example, when looking at a magnet. We idealize the problem by considering parallel spins whose direction has to be estimated. We first review the results about the optimality of different global or local measurement of such a system. We then present a physical measurement model weak enough to almost not disturb the quantum state, but strong enough to provide almost the maximal amount of information in a single shot.

I. INTRODUCTION

In everyday life we continuously perform measurements. For instance, to locate our friends we perform some kind of position measurements; similarly to read this text. Presumably all this can be described with the quantum formalism. But, obviously, these measurements are not standard von Neumann Projective Measurement. They are highly noninvasive while still collecting a large amount of information in a global, single shot. Additionally, from a physical point of view, we expect a fairly simple coupling between system and observer. We call measurements that fulfill these requirements "macroscopic quantum measurements". Our goal is to see if and how macroscopic quantum measurement can be realized. To this end, we consider the specific problem of estimating the direction of a large ensemble of N parallel spin 1/2 particles. This is a simple model for a magnet whose field orientation we would like to measure. We will focus on the small N. The full study for large N will be published soon[3].

Different schemes of optimally guessing the direction of parallel spins have already been discussed in the literature[1,2,4]. For concreteness, we are given an unknown state $|\vec{u}\rangle^{\otimes N}$, where $|\vec{u}\rangle$ is the quantum state of a spin 1/2 particle represented by the Bloch vector in the direction of $\vec{u} \in \mathbb{R}^3$, uniformly distributed. By measuring the state we estimate the direction to be $\vec{w}$. The score is given by the fidelity[4] $|\langle\vec{w}|\ \vec{u}\rangle|^2 = \cos^2\theta/2$, where θ is the angle between $\vec{u}$ and $\vec{w}$.

With this figure of merit, the optimal average guessing fidelity is $\mathcal{F}_{\text{opt}} = (N+1)/(N+2)^4$. For $N > 1$, the optimal measurement cannot be realized by separate measurements on the individual particles[4]. Optimal projective measurements are hence necessarily entangling. Alternatively continuous optimal measurement have been discussed[4,5], but its physical implementation are not straightforward. On the other hand, access to single spins offers asymptotic optimality by measuring each particle in a random direction[1]. All these and other optimal strategies do not realize the idea of macroscopic quantum measurements.

Here, we discuss a physical coupling between the spin ensemble and a measurement device in the spirit of macroscopic quantum measurements. The basic idea is to approximately measure three orthogonal components of the collective spin (e.g., x, y and z direction) simultaneously in a single shot[2]. Surprisingly, we find an intermediate regime of some coupling parameter where, on the one hand, the coupling is strong enough to extract almost maximal information about the system.

II. GENERAL MEASUREMENT MODEL AND AVERAGE FIDELITY

Generally, we consider a scheme where the system state $|\vec{u}\rangle^{\otimes N}$ is coupled to a measurement apparatus $|\phi\rangle$ –called pointer– through virtue of an interaction Hamiltonian H_{int}, during a unite time. Afterwards, the pointer is measured by a projective measurement. The subsequent measurement of the pointer is modelled by a projective measurement with outcome $\vec{r}$ for the eigenvectors $|\vec{r}\rangle$. This outcome is then classically post-processed. Knowledge about the initial pointer state, the coupling and the final measurement allows one to calculate the optimal guess state $|\vec{w}_{\vec{r}}\rangle$.

A typical instance is a pointer with one spatial degree of freedom where the initial spatial wave function of the pointer is a Gaussian function with spread Δ. In order to measure an observable A, one then defines $H_{\text{int}} = p \otimes A$, where p represents the displacement operator in the pointer space, which is formally equivalent to the momentum operator. Thus, the coupling induces a momentum kick on the pointer whose strength depends on the initial system state. Finally, a position measurement of the pointer allows some inference about the system. Information gain of this procedure manifest themselves in the relationship between the spread of the Gaussian, Δ, and the spectrum of the eigenvalues of the operators A. A Δ small compared to the spectral gap of A corresponds to a strong coupling that resolves the individual eigenvalues. On the other side, a Δ large compared to the spectral gap of A means that system states prepared in neighbouring eigenstates cannot be well distinguished.

III. MACROSCOPIC QUANTUM MEASUREMENTS

We now attempt to model our idea of macroscopic quantum measurement. We consider a three dimension rotationally invariant Gaussian pointer with spread Δ. The direction of $|\vec{u}\rangle^{\otimes N}$ is determined by the three expectation values of the collective spin operators $S_k = \frac{1}{2}\sum_i \sigma_k^{(i)}$, where $\sigma_k^{(i)}$ are the Pauli operators acting on the ith qubit for $k = x, y, z$. Thus, a classically inspired interaction Hamiltonian reads

$$H_{\text{int}} = p_x \otimes S_x + p_y \otimes S_y + p_z \otimes S_z = \vec{p} \cdot \vec{S} \qquad (1)$$

The p_k for $k = x, y, z$ represent the displacement operators in the three dimension of the space in which evolves the pointer. As we will see, the three spatial dimensions of the pointer combined with noncommuting operators involve a rich behaviour for nonvanishing Δ. In contrast to the one-dimensional pointer, information gain is not monotonically related to the coupling strength.

IV. RESULTS FOR A FEW SPINS

We calculate the average fidelity $\mathcal{F}_{\text{av}}$ for one to four spins as a function of the spread Δ of the Gaussian pointer. The results are shown in Fig. 1. For two or more spins the optimal Δ is clearly distinct from zero and $\mathcal{F}_{\text{opt}}$ can almost be reached.

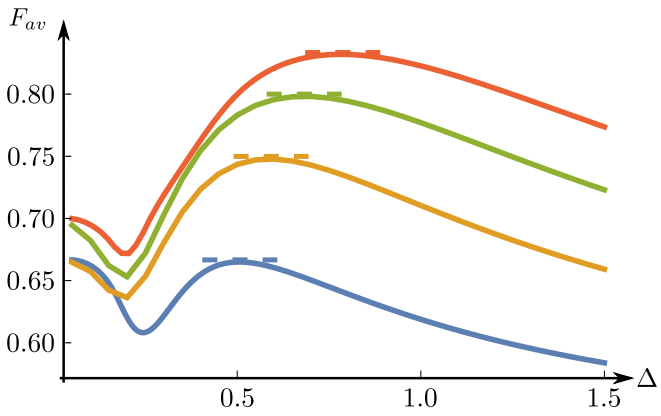

FIG. 1: Average fidelities $\mathcal{F}_{\text{av}}$ for guessing the unknown state as a function of Δ for one to four spins (from bottom to top). The dashed lines correspond to optimal value $\mathcal{F}_{\text{opt}}$. For $N \geq 2$, they are almost reached by some nonzero Δ.

Analyzing the graph shown in Fig. 1 in more detail reveals three distinct regions. For very small values of Δ (i.e., in the strong coupling regime) the predicted limits[2] are recovered, yielding an average fidelity of 2/3 for $N = 1$ and 2 and $\mathcal{F}_{av} = 7/10$ for $N = 3$ and $N = 4$, respectively. On the other extreme, for $\Delta \gg 1$, we see that the average fidelity starts to decline rapidly. This can be understood if one notices that after a certain value of Δ the coupling is so weak that the procedure is essentially equivalent to randomly guessing, therefore yielding an average fidelity of 1/2. The intermediate region is particularly intriguing because in the case of two and more spins the average fidelity is superior to what can be achieved when $\Delta \to 0$. This means that in this case a lesser coupling strength can achieve better results than a strong coupling.

V. DISCUSSION AND OPEN QUESTIONS.

The idea of a macroscopic quantum measurements that behaves "classically" (i.e., physical model with high information gain and low disturbance) within the framework of quantum mechanics is well reflected by the introduced model and pointers with a well chosen spread Δ, for one to four spins. This result seems to hold for large number of spins[3]. More realistic scenarios like with nonmaximally polarized states or the influence of temperature are interesting to study.

Acknowledgments

We thank Pavel Sekatski and Serge Massar for stimulating discussions. This work was supported by the National Swiss Science Foundation (SNSF), the Austrian Science Fund (FWF), grant number J3462, the COST Action No. MP1006 and the European Research Council (ERC MEC).

[1] E. Bagan, A. Monras, and R. Muñoz Tapia. Comprehensive analysis of quantum pure-state estimation for two-level systems. *Phys. Rev. A*, 71:062318, Jun 2005.

[2] G.M. D'Ariano, P. Lo Presti, and M.F. Sacchi. A quantum measurement of the spin direction. *Physics Letters A*, 292(45):233 – 237, 2002.

[3] Tomer J.Barnea, Marc-Olivier Renou, Florian Fröwis, and Nicolas Gisin. Macroscopic quantum measurements: In what direction does a magnet point? *to be published*.

[4] S. Massar and S. Popescu. Optimal extraction of information from finite quantum ensembles. *Phys. Rev. Lett.*, 74:1259–1263, Feb 1995.

[5] Asher Peres. *Quantum Theory: Concepts and Methods*. Kluwer Academic Publishers, New York, 2002.

Experimental setup for combined cavity optomechanics and QED

Thibaud Ruelle,[1] Martino Poggio,[1] and Floris Braakman[1]

[1]*Department of Physics, University of Basel, Klingelbergstrasse 82, 4056 Basel, Switzerland*

Hybrid quantum systems which combine cavity optomechanics (COM) and cavity quantum electrodynamics (CQED) have recently emerged as promising devices in which to observe unique quantum phenomena. We are building an experimental setup to study such systems, in the form of a fiber Fabry-Perot cavity[1,2] (FFPC) in the middle of which a nanomechanical resonator and a two-level system (TLS) can be precisely positioned. We plan on using this setup to investigate three-body interaction effects arising from the simultaneous photon-phonon, phonon-TLS and photon-TLS couplings[3–8]. We expect the combination of these effects to boost our system into the strong single-photon optomechanical coupling regime[7,9], which should in turn make the experimental observation of much sought after nonlinear quantum cavity optomechanical phenomena possible[8,10].

I. MOTIVATION

In recent years, the rapid development of advanced nanofabrication techniques has made increasingly small and high quality nanomechanical resonators available, thus opening up a new regime of size and mass for the exploration of the boundary between quantum and classical physics. By efficiently coupling such a mechanical resonator to light in a high-finesse optical cavity, the field of cavity optomechanics has made tremendous experimental progress towards this objective, and has additionally emerged as an ideal platform for quantum information processing applications[10].

Solid-state cavity optomechanics has up to now relied on strongly driving the optical cavity to enhance the weak dispersive single-photon optomechanical coupling rate so that optomechanical effects overcome dissipation phenomena. While this allowed for groundbreaking experiments such as ground-state cooling of a nanomechanical oscillator[11], squeezing of the light escaping the cavity[12], or optomechanically-induced transparency[13]; the resulting optomechanical interaction is effectively linear, which prevents the observation of single photon and single phonon nonlinear effects inherent to optomechanics[14,15].

In parallel, hybrid mechanical systems in which a nanomechanical resonator is coupled to a two-level system (TLS) have emerged as an alternative route to ground state cooling and quantum control of a mechanical resonator[16,17], but are limited by the short lifetime of the TLS. Since optical control of the TLS is also greatly improved by embedding it in a high finesse cavity, a natural step up is to insert both a mechanical resonator and a TLS in an optical cavity, effectively bridging the gap between cavity OM (COM) and cavity QED (CQED)[3,18]. One thus realizes a tripartite hybrid quantum system in which true three-body interaction effects are expected to occur[4–7,9]; in particular an increase in the effective optomechanical coupling rate by several orders of magnitude was demonstrated in an early circuit cavity electromechanical experimental implementation[7]. Such a system takes full advantage of the intrinsic capacity of a mechanical oscillator to simultaneously couple to a broad range of physically disparate quantum systems, and thus constitutes a promising platform for hybrid quantum information processing[19].

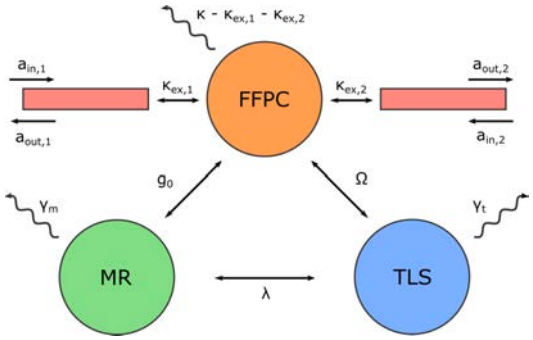

FIG. 1: Coupling scheme for a hybrid tripartite system comprising a FFPC, a mechanical resonator (MR) and a TLS..

In this work we will focus on building an experimental setup in which we can implement tripartite hybrid mechanical systems and explore their rich physics.

II. EXPERIMENTAL SETUP

Our setup will be based on a fiber-based Fabry-Perot optical cavity[2] (FFPC) within which a coupled nanomechanical resonator and TLS system can be precisely positioned, forming a membrane-in-the-middle (MIM) system[20]. The fiber cavity will be operated in vacuum at cryogenic temperatures, and pumped by a laser through one of the fibers. The interaction between the different subsystems will be studied through the reflected and transmitted signals, as depicted in fig. 1.

The MIM geometry was chosen for its flexibility. It allows to independently choose and modify the optical cavity and the mechanical resonator and TLS system, making it possible to explore a broad range of experimental parameters.

The fiber-based optical cavity was chosen for its small mode volume and for its direct compatibility with fiber-coupled instrumentation, which makes it ideally suited to cryogenic operation. Additionally, FFPCs exhibit high finesses and small mode volumes, allowing for

large optomechanical coupling with sub-wavelength sized nanomechanical resonators[20]. Finally, the mechanical resonator can be precisely positioned within the cavity by mounting it on a 3D translation stage.

An example of nanomechanical system and TLS system that can be coupled to the FFPC is the GaAs/AlGaAs nanowire with self-assembled quantum dots (QDs) system, in which strain-mediated coupling between the nanowire and the QDs was previously demonstrated[21]. The coupling between the cavity and the QD exciton can be described by the standard Jaynes-Cummings model[4].

III. OUTLOOK

We expect the combination of the interactions between each subsystems to boost the effective optomechanical coupling rate in our tripartite hybrid system and allow us to reach the strong single-photon coupling regime. We then intend to consider a number of different nanomechanical resonator and TLS systems in order to explore a broader range of experimental parameters and study the three-body interaction physics specific to this system in different regimes.

Acknowledgments

This work is funded by the Swiss National Science Foundation (Ambizione Grant No. PZOOP2161284/1).

[1] T. Steinmetz, Y. Colombe, D. Hunger, T. W. Hnsch, A. Balocchi, R. J. Warburton, and J. Reichel, *Stable fiber-based Fabry-Prot cavity*, Applied Physics Letters **89**, 111110 (2006).

[2] D. Hunger, T. Steinmetz, Y. Colombe, C. Deutsch, T. W. Hnsch, and J. Reichel, *A fiber FabryPerot cavity with high finesse*, New Journal of Physics **12**, 065038 (2010).

[3] M. Wallquist, K. Hammerer, P. Zoller, C. Genes, M. Ludwig, F. Marquardt, P. Treutlein, J. Ye, and H. J. Kimble, *Single-atom cavity QED and optomicromechanics*, Physical Review A **81**, 023816 (2010).

[4] J. Restrepo, C. Ciuti, and I. Favero, *Single-Polariton Optomechanics*, Physical Review Letters **112**, 013601 (2014).

[5] O. Kyriienko, T. Liew, and I. Shelykh, *Optomechanics with Cavity Polaritons: Dissipative Coupling and Unconventional Bistability*, Physical Review Letters **112**, 076402 (2014).

[6] M. Abdi, M. Pernpeintner, R. Gross, H. Huebl, and M. J. Hartmann, *Quantum State Engineering with Circuit Electromechanical Three-Body Interactions*, Physical Review Letters **114**, 173602 (2015).

[7] J.-M. Pirkkalainen, S. U. Cho, F. Massel, J. Tuorila, T. T. Heikkil, P. J. Hakonen, and M. A. Sillanp, *Cavity optomechanics mediated by a quantum two-level system*, Nature Communications **6**, 6981 (2015).

[8] F. Lecocq, J. D. Teufel, J. Aumentado, and R. W. Simmonds, *Resolving the vacuum fluctuations of an optomechanical system using an artificial atom*, Nature Physics **11**, 635 (2015).

[9] B. Sarma and A. K. Sarma, *Ground-state cooling of micromechanical oscillators in the unresolved-sideband regime induced by a quantum well*, Physical Review A **93**, 033845 (2016).

[10] M. Aspelmeyer, T. J. Kippenberg, and F. Marquardt, *Cavity optomechanics*, Reviews of Modern Physics **86**, 1391 (2014).

[11] J. Chan, T. P. M. Alegre, A. H. Safavi-Naeini, J. T. Hill, A. Krause, S. Grblacher, M. Aspelmeyer, and O. Painter, *Laser cooling of a nanomechanical oscillator into its quantum ground state*, Nature **478**, 89 (2011).

[12] A. H. Safavi-Naeini, S. Grblacher, J. T. Hill, J. Chan, M. Aspelmeyer, and O. Painter, *Squeezed light from a silicon micromechanical resonator*, Nature **500**, 185 (2013).

[13] S. Weis, R. Rivire, S. Delglise, E. Gavartin, O. Arcizet, A. Schliesser, and T. J. Kippenberg, *Optomechanically Induced Transparency*, Science **330**, 1520 (2010).

[14] A. Nunnenkamp, K. Brkje, and S. M. Girvin, *Single-Photon Optomechanics*, Physical Review Letters **107**, 063602 (2011).

[15] P. Rabl, *Photon Blockade Effect in Optomechanical Systems*, Physical Review Letters **107**, 063601 (2011).

[16] A. D. OConnell, M. Hofheinz, M. Ansmann, R. C. Bialczak, M. Lenander, E. Lucero, M. Neeley, D. Sank, H. Wang, M. Weides, et al., *Quantum ground state and single-phonon control of a mechanical resonator*, Nature **464**, 697 (2010).

[17] P. Treutlein, C. Genes, K. Hammerer, M. Poggio, and P. Rabl, *Hybrid Mechanical Systems*, in *Cavity Optomechanics*, edited by M. Aspelmeyer, T. J. Kippenberg, and F. Marquardt (Springer Berlin Heidelberg, 2014), Quantum Science and Technology, pp. 327–351.

[18] T. Ramos, V. Sudhir, K. Stannigel, P. Zoller, and T. J. Kippenberg, *Nonlinear Quantum Optomechanics via Individual Intrinsic Two-Level Defects*, Physical Review Letters **110**, 193602 (2013).

[19] M. Wallquist, K. Hammerer, P. Rabl, M. Lukin, and P. Zoller, *Hybrid quantum devices and quantum engineering*, Physica Scripta **2009**, 014001 (2009).

[20] I. Favero, J. Sankey, and E. M. Weig, *Mechanical Resonators in the Middle of an Optical Cavity*, in *Cavity Optomechanics*, edited by M. Aspelmeyer, T. J. Kippenberg, and F. Marquardt (Springer Berlin Heidelberg, 2014), Quantum Science and Technology, pp. 83–119.

[21] M. Montinaro, G. Wst, M. Munsch, Y. Fontana, E. Russo-Averchi, M. Heiss, A. Fontcuberta i Morral, R. J. Warburton, and M. Poggio, *Quantum Dot Opto-Mechanics in a Fully Self-Assembled Nanowire*, Nano Letters **14**, 4454 (2014).

Velocity Control of Trapped Ions during Transport

Robin Oswald,[1] Ludwig E. de Clercq,[1] Matteo Marinelli,[1] David Nadlinger,[1] Vlad Negnevitsky,[1] and Jonathan Home[1]

[1]*Institute of Quantum Electronics, ETH-Hönggerberg, CH-8093, Zürich, Switzerland*

Transport is a key ingredient of the proposed QCCD architecture. By transporting ions through laser beams one can also implement logic gates. However, this requires good control over the transport velocity, because it determines the time the ion interacts with the laser and because of potential Doppler shifts. Here, we measure the velocity of a single $^{40}Ca^{+}$ ion during transport across a linear Paul trap. We then use iterative learning control to reduce velocity fluctuations from 0.1 m/s down to 0.01 m/s. This is an important step on the path to two-qubit transport gates. Furthermore, we find ILC to be well suited for optimizing the time-varying feedforward control inputs driving repetitive quantum processes.

I. INTRODUCTION

Trapped atomic ions are currently one of the most advanced platforms for quantum information experiments. Qubits encoded in the electronic states of ions can reliably be initialized, manipulated and read out. While this works well for a few qubits, scaling to a large number of them is a formidable challenge. To that end, the quantum-charge coupled device architecture proposes interconnecting many small traps and transporting ions between them in order to then perform logic gates between different qubits locally with short laser pulses[1]. To reduce the optical requirements transport gates were later proposed[2] and demonstrated[3]. These gates are implemented by transporting an ion through a static laser beam, thus eliminating the requirement to pulse the laser. Control of the transport velocity then becomes crucial because it determines the time the ion spends in the laser beam, and because of possible Doppler shifts between the laser frequency in the lab frame and the one experienced by the ion. Here, we demonstrate the use of iterative learning control (ILC) to keep the velocity constant during transport.

II. EXPERIMENT

We trap a single $^{40}Ca^{+}$ ion in a linear Paul trap with segmented dc electrodes as illustrated in Fig. 1a). The oscillating voltages applied to the rf electrodes result in an effective trapping potential along the radial direction. Because of the strong confinement along the radial direction, we will not consider it further. The segmented dc electrodes labelled 1-15 are used to confine and transport the ion along the axial direction. The potentials $\phi^e(z)$ due to these individual electrodes are shown in Fig. 1b). Ideally, we aim to confine the ion in a harmonic well resulting from a superposition of the voltages $u^e(t)$ applied to the various segmented dc electrodes, as illustrated in Fig. 1c). For transport, the applied voltages are changed over time such that the center position of the harmonic well is displaced adiabatically.

We calculate the time-varying voltages (hereafter referred to as waveforms) using optimal control. We construct a cost function that captures how accurately the desired potential well is realized and add several regularization terms reflecting the capabilities of our underlying control electronics. Furthermore, we enforce constraints on the absolute voltage and the slew rate. The waveforms are then obtained by minimizing the cost function subject to these constraints.

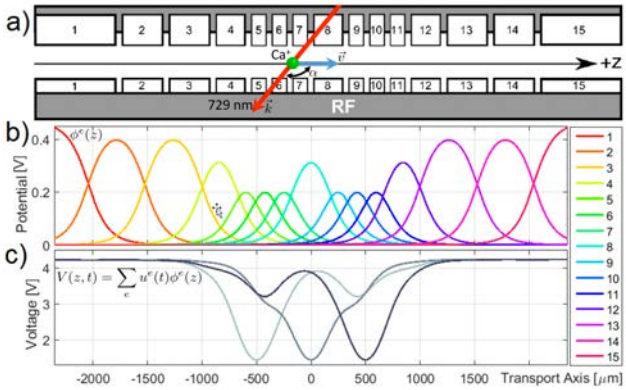

FIG. 1: a) Schematic drawing of the trap electrodes. b) Potentials along the transport axis z due to a unit voltage on the individual electrodes. c) Sample of three harmonic trapping wells generated by superpositions of the electrodes.

In order to control the velocity, we first need to be able to measure it. To do so, we measure the evolution of the optical qubit encoded in the electronic states of the ion. In an appropriately chosen rotating frame, the Hamiltonian governing the evolution of the qubit is given by

$$\hat{H}(t) = \frac{\hbar}{2}\left(-\Omega(t)\hat{\sigma}_x + \delta(t)\hat{\sigma}_z\right) \tag{1}$$

where $\delta(t)$ and $\Omega(t)$ are the time-varying detuning and Rabi frequency experienced by the ion as it moves through the static laser beam. The detuning $\delta(t)$ is composed of the laser detuning δ_L from resonance and an additional Doppler shift. In the case of motion along the z-axis and planar wavefronts, we have

$$\delta(t) = \delta_L - \left|\vec{k}\right|\left|\vec{v}(t)\right|\cos(\alpha) \tag{2}$$

where $\vec{k}$ is the laser wavevector, $\vec{v}$ the velocity and α the angle between $\vec{k}$ and $\vec{v}$. By measuring the evolution of

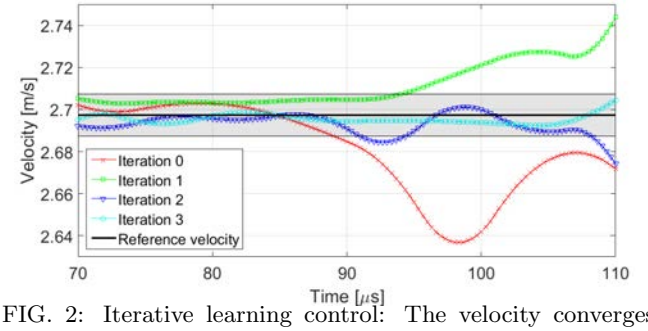

FIG. 2: Iterative learning control: The velocity converges within a few iterations to the desired reference velocity.

the qubit over time for various laser detunings δ_L, we can recover the time-dependent Hamiltonian $\hat{H}(t)$ and consequently also the velocity of the ion[4].

Finally, we control the velocity of the ion using iterative learning control, which is a technique to optimize feedforward control inputs driving repetitive processes between different trials. We first generate a waveform $u_i^e(t)$, use it to transport the ion and measure the resulting velocity $v_i^{\text{meas}}(t)$. Based on the control inputs $u_i^e(t)$, the measured velocity error $e_i^{\text{meas}}(t) = v^{\text{ref}}(t) - v_i^{\text{meas}}(t)$ and our model of the system, we generate a new waveform $u_{i+1}^e(t) = u_i^e(t) + \Delta u_i^e(t)$ where $\Delta u_i^e(t)$ is designed to counteract the previously measured velocity error. These steps are repeated until the velocity error converges to within a set tolerance. Specifically, to calculate the small adjustments $\Delta u_i^e(t)$ to the control inputs $u_i^e(t)$, we again optimize a cost function consisting of the predicted error at the next iteration $i+1$ and various regularization terms that ensure that the overall changes are small (which is important for this procedure to be valid in the first place, as we linearize the full nonlinear process model around the expected trajectory to predict the changes).

III. RESULTS AND DISCUSSION

The velocity profiles measured at various stages of the learning process are shown in Fig. 2. Here, we aimed to keep the velocity constant over time. The procedure quickly converged and reduced the velocity fluctuations to within the measurement uncertainty of roughly $\pm$ 0.01 m/s indicated by the are shaded in grey (more elaborate error estimates would be desirable, but are currently not available). Once we can not confidently measure an error signal anymore, we terminate the procedure. It reliably reduced initial velocity fluctuations of around 0.1 m/s down to 0.01 m/s within a few iterations for various test cases. The corrections that ILC applied to the initial waveforms were of the order of a few tens of millivolts at most, which is tiny compared to the overall range of roughly 10 Volts that the electrodes go through during transport. This validates our approach of linearizing around the original trajectory. It also shows that the velocity is very sensitive with respect to the waveforms. Without performing ILC, we would need an extremely accurate model of our system in order to calculate the required waveforms exactly. The main benefit of using ILC is thus that we can use a reasonably accurate model in conjunction with several trials in order to obtain optimized waveforms verified on the actual system.

IV. CONCLUSIONS

We demonstrated the use of ILC to control the velocity of a single ion during transport. We reduced velocity fluctuations from around 0.1 m/s down to 0.01 m/s corresponding to the measurement uncertainty. This is useful for the implementation of transport quantum logic gates, which shift some of the technical burden from the optical to the electrical domain which has a proven scaling track record. In a next step, it would be interesting to see if we can also perform two-qubit transport gates, e.g. a transport version of the Mølmer-Sørensen gate.

ILC appears to be well suited for optimizing non-trivial time-varying feedforward control inputs used to drive quantum mechanical systems, especially because the destructive nature of measurements in quantum mechanics often prohibits the use of real-time feedback. Further adapting ILC to the way measurements are obtained to improve the efficiency would therefore seem worthwhile.

Acknowledgments

We thank Amin Rezaeizadeh and Roy Smith for helpful discussions about ILC. We gratefully acknowledge financial support through the NCCR QSIT and through the Swiss SNF.

[1] D. Kielpinski, C. Monroe, and D. J. Wineland, *Architecture for a large-scale ion-trap quantum computer*, Nature **417**, 709 (2002).

[2] D. Leibfried, E. Knill, C. Ospelkaus, and D. J. Wineland, *Transport quantum logic gates for trapped ions*, Phys. Rev. A **76**, 032324 (2007).

[3] L. E. de Clercq, H.-Y. Lo, M. Marinelli, D. Nadlinger, R. Oswald, V. Negnevitsky, D. Kienzler, B. Keitch, and J. P. Home, *Parallel transport quantum logic gates with trapped ions*, Phys. Rev. Lett. **116**, 080502 (2016).

[4] L. de Clercq, R. Oswald, C. Flühmann, B. Keitch, D. Kienzler, H.-Y. Lo, M. Marinelli, D. Nadlinger, V. Negnevitsky, and J. Home, *Estimation of a general time-dependent hamiltonian for a single qubit*, Nature Communications **7** (2016).

Photonics of the transition metal dichalcogenides

Jonas Roch,[1] Mathieu Munsch,[1] Péter Makk,[2] Christian Schönenberger,[2] and Richard Warburton[1]

[1]*Department of Physics, Nano-photonics group, University of Basel, CH-4056, Basel, Switzerland*
[2]*Department of Physics, Nanoelectronics group, University of Basel, CH-4056, Basel, Switzerland*

Since the first experimental realisation and isolation of a graphite monolayer ten years ago through mechanical exfoliation[1], isolation of monolayers of various van der Waals crystals has been achieved. Among these materials, transition metal dichalcogenides (TMDCs) is a class of materials including optically active monolayer semiconductors with a bandgap lying in the visible part of the electromagnetic spectrum[2]. The large spin-orbit coupling make these materials interesting for spintronics, while their large excitonic binding energy ensures that room temperature physics is dominated by the excitons[2]. Moreover, TMDCs monolayers exhibit a broken inversion symetry leading to an interesting band structure, thus opening the way to valley-tronics[3].

I. INTRODUCTION

The transition metal dichalcogenides is a class of elements with the MX_2 stoichiometry formed by an hexagonal plane of a transition metal element M placed between two hexagonal planes of chalcogen atoms X, as depicted in Fig. 1[2].

The bulk material consists of multiple layers TX_2 bound by van der Waals interaction. This enables micromechanical cleavage (scotch tape method) of the crystal for isolating monolayer crystal flakes and transferring them onto any substrate[4]. Monolayer flakes can be distinguished from thicker flakes by mean of Raman spectroscopy, optical contrast measurement, photoluminescence analysis or atomic force microscopy[2].

In monolayers TMDCs, the crystal structure breaks the inversion symmetry leading to a band structure with a direct bandgap not occuring at the center of the Brillouin zone. The bandstructure indeed consists of two valleys at wavevector K and $K' = -K$, in which the electrons carry opposite spins[2]. It was shown that it is possible to selectively excite carriers in only one valley by exciting with circularly polarized light, leading to the so-called valley polarization[5], as depicted in Fig. 2.

Optical properties of the TMDCs are strongly influenced by the substrate on which the monolayer is lying[6]. A way to circumvent this problem is to study suspended monolayers, which constitutes an excellent realization of the infinite boundary two dimensional quantum well. Another option consists in transfering the TMDC flake via

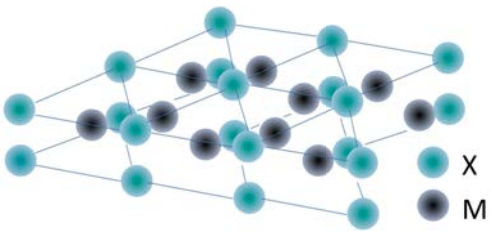

FIG. 1: Crystalline structure of a TMDC monolayer formed by a transition metal M atom plane between two planes of chalcogen atoms X.

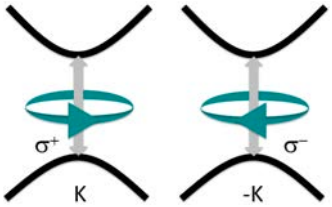

FIG. 2: Optical valley selection rules and schematic bandstructure of TMDCs.

wet or dry transfer techniques to another atomically thin layer of a different van der Waals crystal, thus ensuring a very smooth substrate for the flake and leading to interesting van der Waals heterostructures[7].

II. PHOTONICS OF MOLYBDENUM DISULFIDE

Molybdenum disulfide MoS_2 is one of the optically active TMDC materials and exhibits a photoluminescence dominated by the lowest energy neutral exciton (A-exciton) contribution up to room temperature. However, its quantum yield is low, of the order of 10^{-6} at room temperature when placed on silicon dioxide. Hexagonal boron nitride (h-BN), which was seen to significantly improve the electrical caracteristics of graphene[8], has been reported to improve the photoluminescence of monolayers TMDCs[5] and this can be seen in Fig. 3, where a significant increase in integrated photoluminescence is seen on the area where MoS_2 lies on h-BN.

Using a polarization resolved confocal microscope, the valley properties of monolayer MoS_2 have been verified at a temperature of 4 K, as shown in Fig. 4 (left). The large feature at 1.8 eV stems from unpolarized defects-related luminescence,while the peak truncated at 1.93 eV is the A-exciton excited with a σ^+ polarized HeNe laser[5]. The polarization contrast, defined as[5]

$$\rho = \frac{I(\sigma^+) - I(\sigma^-)}{I(\sigma^+) + I(\sigma^-)}, \tag{1}$$

is represented in Fig. 4 (right). The valley polarization peaks at a 60%, a slightly lower value than those reported

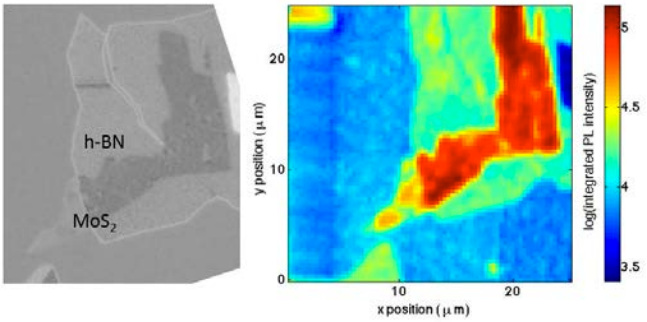

FIG. 3: Optical image (left) and micro-photoluminescence mapping (right) of a monolayer MoS_2 flake on an h-BN flake. Both images have the same scale.

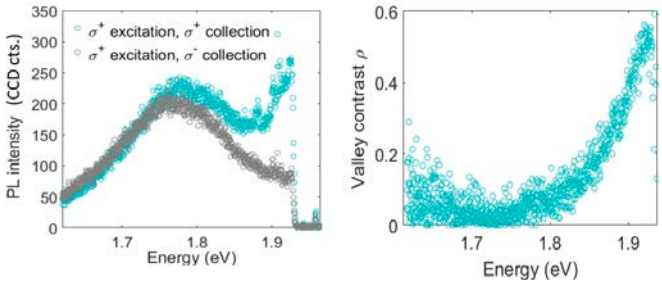

FIG. 4: Photoluminescence spectrum of a MoS_2 monolayer on a h-BN substrate at a temperature of 4 K with a circularly polarized HeNe excitation (left). The valley contrast peaks at 60% for the A-exciton.

in the litterature for MoS_2 on h-BN[5].

III. OUTLOOK

In order to improve the photoluminescence of MoS_2 and to glean a better understanding of the carrier recombination dynamics in this material, a study of gated samples can bring fruitful informations: it is possible to access the charged excitons states by tuning the Fermi energy with the help of an out-of-plane electric field[9]. The graphene community demonstrated that h-BN encapsulated samples exhibit high mobility[10]. Encapsulation of MoS_2 might also be interesting for optics, as the h-BN on both sides should protect the MoS_2 flake and allow for a better environment stability. Investigation of substrate-free MoS_2 suspended monolayers should also be considered, as it allows to probe the inherent recombination mechanisms and obviously opens a way toward optomechanics.

[1] K. Novoselov, *Electric field effect in atomically thin carbon films.*, Science **306**, 666 (2004).

[2] S. Butler, *Progress, challenge, and opportunities in two-dimensional materials beyond graphene*, ACSnano **10**, 2898 (2013).

[3] X. Xu, W. Yao, D. Xiao, and T. Heinz, *Progress, challenge, and opportunities in two-dimensional materials beyond graphene*, nature physics **7**, 343 (2014).

[4] K. Novoselov, D. Jiang, F. Schedin, T. J. Booth, V. Khotkevich, S. Morozov, and A. Geim, *Progress, challenge, and opportunities in two-dimensional materials beyond graphene*, nature physics **7**, 343 (2014).

[5] K. Mak, K. He, J. Shan, and T. Heiz, *Control of valley polarization in monolayer mos2 by optical helicity*, nature nanotechnology **7**, 494 (2012).

[6] M. Buscema, G. Steele, H. van der Zant, and A. Castellanos-Gomez, *The effect of the substrate on the raman and photoluminescence emission of single layer mos2.*, eprint arXiv:1311.3869 (2013).

[7] A. Geim and I. Grigorieva, *Van der waals heterosturctures*, nature **499**, 419 (2013).

[8] C. Dean, A. Young, I. Meric, C. Lee, L. Wang, S. Sorgenfrei, K. Watanabe, T. Taniguchi, P. Kim, K. Shepard, et al., *Boron nitride substrates for high-quality graphene electronics*, nature nanotechnology **5**, 722 (2010).

[9] K. Mak, K. He, L. C., G. Lee, J. Hone, and T. Heinz, *Tightly bound trions in monolayer mos2*, nature materials **12**, 207 (2013).

[10] A. Mayorov, R. Gorbachev, A. Morozov, L. Britnell, R. Jalil, L. Ponomarenko, P. Blake, K. Novoselov, K. Watanabe, T. Taniguchi, et al., *Micrometer-scale ballistic transport in encapsulated graphene at room temperature*, Nano Letter **11**, 2396 (2011).

Coherent strain–mediated coupling of a single spin to a mechanical resonator

Johannes Kölbl,[1] Arne Barfuss,[1] Jean Tessier,[1] and Patrick Maletinsky[1]

[1] *Department of Physics, University of Basel, CH-4056, Basel, Switzerland*

The nitrogen–vacancy (NV) center, a lattice defect in diamond, offers a highly coherent and optically addressable electronic spin system, which make it particularly amenable to applications in spin–based quantum sensing and quantum information processing. Besides the conventional manipulation of the NV center's spin using external time–varying magnetic fields' major progress on coherently control these quantum systems with crystal strain was achieved in the last years. Here, we present results on a hybrid spin–oscillator device, in which the coupling between the motion of a diamond mechanical oscillator and single embedded NV centers is mediated by intrinsic crystal strain. Employing mechanical driving and microwave field manipulation we observe a dependance of the NV center's ground state's evolution on the phase of the driving fields. This enables the realization of a cyclic three–level system, on which all three transitions can be coherently addressed.

I. INTRODUCTION

Hybrid quantum–mechanical systems have attracted ever–increasing attention during the last years, since these devices are outstanding candidates for applications in quantum information processing[1] and quantum–assisted nanoscale sensing[2]. In this context the spin–dynamics in hybrid spin–oscillator devices consisting of nitrogen–vacancy (NV) center spins coupled to the degrees of freedom of diamond nanomechanical resonators led to significant interest[3]. Here, the NV center offers a variety of particular optical and electronic spin features, that renders it an attractive quantum system.

II. EXPERIMENTAL SYSTEM

The negatively charged NV center in diamond is a solid-state, atom–like impurity. It comprises a nitrogen atom, which substitutes for a carbon atom in the diamond crystal lattice, and an adjacent lattice vacancy (Fig. 1a). The NV's electronic ground state on which our experiments focus consists of a spin triplet ($S = 1$). The basis states of the three spin levels correspond to the eigenstates $|m_s\rangle$ of the spin operator S_z along the NV's symmetry axis, i. e. $\{|-1\rangle, |0\rangle, |+1\rangle\}$. The $|\pm1\rangle$ states are shifted from the $|0\rangle$ state by a zero–field splitting of 2.87 GHz induced by spin–spin interactions[4]. An external magnetic field applied along the NV axis leads to a Zeeman splitting of the $|\pm1\rangle$ levels and therefore lifts their degeneracy. Moreover, hyperfine interactions between the NV's electronic spin and the nuclear spin of the ^{14}N ($I = 1$) split the $|\pm1\rangle$ spin levels into three sublevels each, corresponding to $m_I = -1, 0, +1$ (Fig. 1c).

In general, studies on NV centers are based on convenient optical methods to initiate and read–out the NV spin. Each spin level of the NV's ground state triplet is linked to an excited state sublevel via a spin preserving optical transition (Fig. 1b). Moreover, the excited $|\pm1\rangle$ states have a non–zero probability to decay non–radiatively into metastable singlet states, which lie energetically between the ground and excited states. These

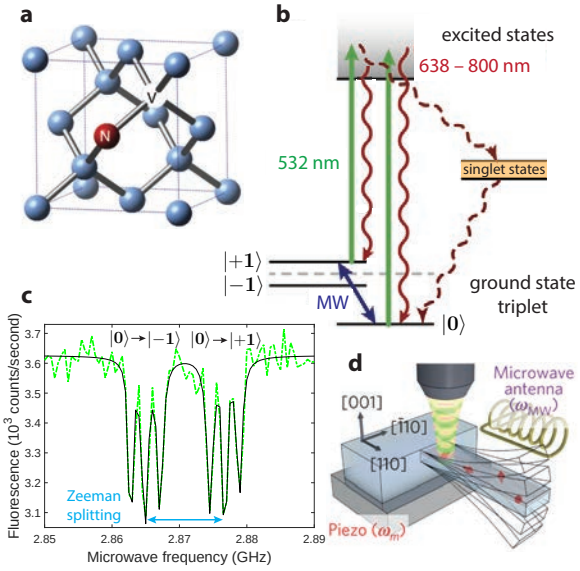

FIG. 1: **NV center and experimental setup. a** Atomic structure of the NV defect in the diamond lattice with symmetry axis defined by the nitrogen and vacancy sites[5]. **b** Diagram of the electronic energy level structure with ground state triplet split by the zero–field splitting, excited states and metastable singlet states. Spin polarization and read–out is achieved by optical excitation at 532 nm (green) and fluorescence detection (red). Decay via the metastable states is non–radiative (red dashes). Resonant MW excitation allows for ground state spin manipulation (blue arrow)[5]. **c** Optically detected ESR of the NV's $|\pm1\rangle$ hyperfine sublevels (green) for a finite magnetic field applied along the NV axis with fit (black). **d** Single NV spins (red) are embedded in a diamond cantilever resonantly actuated at frequency ω_{m} via a piezo–element. The NV spin is initialized and read out by green laser light and manipulated by MW magnetic fields with frequencies ω_{MW} generated by a nearby antenna[3].

metastable states selectively decay into the $|0\rangle$ ground state at a rate much smaller than the excited state radiative decay rate. Thus, initialization or polarization of the NV's spin into the $|0\rangle$ ground state can be realized by continuous optical excitation with green laser light. In

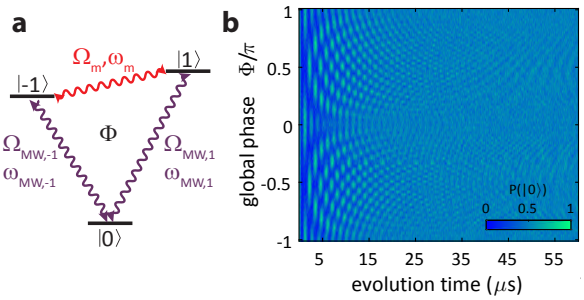

FIG. 2: **Closed–contour interaction. a** Three–level system and closed–contour interaction of a single NV spin with transition and Rabi frequencies ω and Ω, respectively. The global phase of the three driving fields is denoted by Φ. **b** The spin dynamics of the system offers a phase–dependent damping of the Rabi oscillations.

addition, and as a result of the same decay dynamics, the decay into the metastable singlets yields less fluorescence of the $|\pm1\rangle$ levels compared to the $|0\rangle$ state. This mechanism therefore allows for efficient detection and read–out of the NV's spin state via the fluorescence contrast.

Together, these two properties enable the performance of optically detected electron spin resonance (ESR), where microwave (MW) magnetic fields drive transitions from $|0\rangle \rightarrow |\pm1\rangle$ and thereby populate less fluorescent states yielding an observable ESR contrast (Fig. 1c). Such MW fields can be also used to drive the spin–transitions coherently and prepare the NV in arbitrary coherent superpositions of spin states.

Besides their coupling to an external magnetic field, the NV spin states respond sensitively to strain in the diamond host lattice[6]. In particular, strain applied perpendicular to the NV axis mixes the $|\pm1\rangle$ states and leads to direct coupling between them. On that account, near–resonant, time–varying strain, e. g. evoked by periodic oscillations of a mechanical resonator, can coherently drive the $|-1\rangle \leftrightarrow |+1\rangle$ transition for a fixed nuclear spin sublevel[3]. This $\Delta m_s = 2$ transition is magnetically dipole–forbidden and therefore difficult to access with MW fields. Furthermore, crystal strain fields are intrinsic to the system, so this mechanism is immune to drifts in the coupling strength and does not generate spurious electromagnetic stray fields.

To combine the discussed aspects we use our hybrid spin–oscillator system comprising electronic spins in individual NV centers embedded in a single–crystalline diamond mechanical cantilever with dimensions in the micron–scale (Fig. 1d). The cantilever, whose fundamental flexural mode typically lies within the 10 MHz regime, is resonantly actuated by means of a piezoelectric transducer. This motion induces a strain coupling to the embedded NV center spins. We use optical excitation with green laser light and fluorescence detection to initialize and read out the NV spin with a home–built confocal optical microscope. A nearby antenna generates a MW magnetic field, which is employed to manipulate the NV spin state.

III. RESULTS

The unique combination of the NV spin structure and its coherent coupling to strain allows for a study of a three–level system[7], on which all three spin transitions can be coherently addressed – a situation which is usually not encountered in quantum optics or spin systems and whose dynamics remains unexplored. In particular, we investigate the spin dynamics of the NV center's ground state under the influence of three driving fields – two MW and one strain field resonant with the three possible spin transitions in the system. By addressing these transitions coherently we realize a "closed–contour interaction scheme" (Fig. 2a). This system can be understood in complete analogy to a model of an electron hopping on a ring consisting of three lattice sites yielding as new eigenstates linear combinations of the NV's ground state spin triplet (corresponding to electronic orbits on the ring). Initializing the system in $|0\rangle$ we measure the final population in the same state after the system evolves for a veriable amount of time.

First results of this experiment clearly demonstrate, that the spin dynamics of the cyclic system strongly depend on the driving fields phases (Fig. 2b). Therefore our findings present an interesting situation, where the NV center might serve as an atomic interferometer to exactly determine the phase of our mechanical resonator.

IV. OUTLOOK

The implemented three–level system comprising a single, highly coherent spin forms a resource for the study of unconventional spin dynamics. The phase–dependent time evolution of the closed–contour scheme enables the preparation of long–living, highly–coherent spin eigenstates within our spin–oscillator device. Thereby our results emphasize the attractiveness of our hybrid system as a platform for future sensing devices and applications in the quantum regime.

[1] S. Prawer and I. Aharonovich, eds., *Quantum Information Processing with Diamond* (Elsevier Science Limited, 2014).
[2] P. Maletinsky et al., Nat. Nano. **7**, 320 (2012).
[3] A. Barfuss et al., Nat. Phys. **11**, 820 (2015).
[4] M. W. Doherty et al., Phys. Rev. B **85**, 205203 (2012).
[5] N. Bar-Gill et al., Nat. Comm. **3**, 858 (2012).
[6] J. Teissier et al., Phys. Rev. Lett. **113**, 020503 (2014).
[7] S. Buckle et al., Optica Acta: Int. J. Opt. **33**, 1129 (1986).

Traveling wave Zeeman deceleration of molecules

Tomislav Damjanović,[1] Dongdong Zhang,[1] and Stefan Willtsch[1]

[1] *Department of Chemistry, University of Basel, Klingelbergstrasse 80, CH-4056 Basel, Switzerland*

Cold and controlled molecules have a great potential for new experiments in the realm of quantum technologies. For that purpose, in our laboratory, a new type of Zeeman decelerator for slowing atoms and molecules possessing magnetic dipole moments in so-called low-field-seeking states (LFS) is being developed. The decelerator produces a traveling magnetic trap with tunable longitudinal velocity and transverse orientation. Atoms and molecules are trapped around a node of a propagating trap provided that the initial velocity of the trap matches the velocity of the supersonic molecular beam package. In addition, three-dimensional confinement is achieved independently from the longitudinal motion of the trap. The decelerated molecules exhibit an exquisite quantum-state purity and can be trapped for subsequent experiments.

I. INTRODUCTION

In recent years, significant efforts have been invested to develop methods for the production of samples of atoms and molecules at cold ($< 1K$) and ultra-cold temperatures ($< 1mK$). Due to the lack of closed cycling transitions suitable for laser cooling of molecules, different methods have been developed to cool molecules based on the interactions with electric, magnetic and radiation fields. Two methods have been proven to be especially effective in achieving cold samples of atoms and molecules starting from a supersonic beam, namely Stark deceleration and Zeeman deceleration[1]. The developments in achieving samples of molecules at very low temperatures have been motivated by the prospect of studying atomic collisions and chemical reaction with controllable collision energies, performing high resolution spectroscopy and precision measurements for fundamental physics, quantum information processing and quantum simulation[2].

The Zeeman deceleration method relies on the state-dependent interaction of neutral paramagnetic atoms or molecules with a time-dependent inhomogeneous magnetic field. For this reason the Zeeman deceleration technique is especially effective for open-shell systems such as molecular radicals or metastable atoms and molecules.

II. TRAVELING WAVE MAGNETIC TRAP

The decelerator under construction in our laboratory is based on a helical wire geometry as an extension of the setup of Trimeche et al[3]. It produces a traveling wave of magnetic field with tunable longitudinal velocity. Atoms and molecules possessing magnetic dipole moment in so-called low-field-seeking (LFS) states are trapped around the node of the propagating magnetic wave provided that the initial longitudinal velocity of the traveling trap matches the velocity of the molecular beam package. In addition, three-dimensional confinement is achieved by rotating the trap transversely. The time-varying inhomogeneous magnetic fields are produced by coils in a helical wire geometry, as shown in figure 1.They

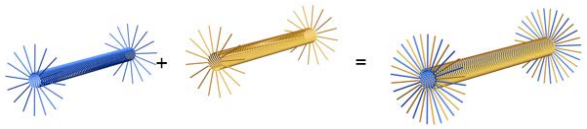

FIG. 1: Helical wire geometry consists of 16 wires of right-handed orientation and 16 wires of left-handed orientation.

consist of 16 wires of right-handed orientation which produces static magnetic field $\mathbf{B}_i^{Right}$ $(i = 0, ..., 15)$ and 16 wires of left-hand orientation which produces static magnetic field $\mathbf{B}_i^{Left}$ $(i = 0, ..., 15)$ for an applied constant current through the wires. By introducing explicit time dependence of the current, one readily obtains a moving 1D trap along beam direction as show in fig 2. The requirement of a sinusoidal time dependence of the current involves two independently controllable parameters ϕ_z and ϕ_θ, such that the total magnetic field produced by the helix geometry at a given time reads:

$$\mathbf{B}(\mathbf{x},\mathbf{y},\mathbf{z},\mathbf{t})_{total}^{Right} = \sum_{i=0}^{15} cos(i\pi/8+\phi_z(t)+\phi_\theta(t))\mathbf{B}(\mathbf{x},\mathbf{y},\mathbf{z})_i^{Right}$$

,

$$\mathbf{B}(\mathbf{x},\mathbf{y},\mathbf{z},\mathbf{t})_{total}^{Left} = \sum_{i=0}^{15} cos(i\pi/8+\phi_z(t)-\phi_\theta(t))\mathbf{B}(\mathbf{x},\mathbf{y},\mathbf{z})_i^{Left}$$

.

Initially, the longitudinal velocity of the moving trap matches the beam velocity. The longitudinal velocity of the trap is then linearly reduced, corresponding to a constant deceleration of the magnetic trap in the laboratory frame, such that molecules that are initially trapped in the traveling trap will be decelerated. In conventional Zeeman decelerators the transverse focusing force is usually small and thus transverse motion of molecules significantly reduces phase-space acceptance of the decelerator[4]. Our traveling trap has good confinement over all transverse directions as shown in figure 3 and figure 4, while having the longitudinal and transverse motion of molecules inside the trap decoupled from each other.

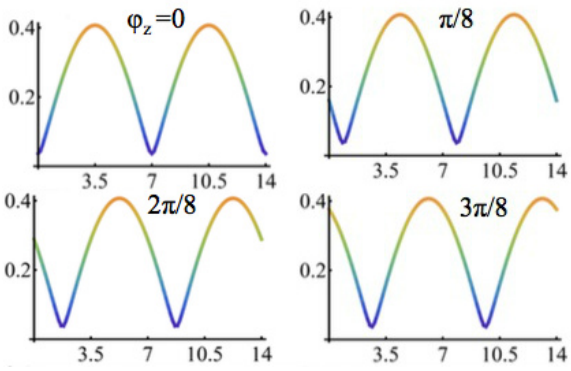

FIG. 2: Magnetic field profile for different values of time dependent parameter ϕ_z. Minimum of the magnetic field propagates in positive z direction with increasing parameter ϕ_z.

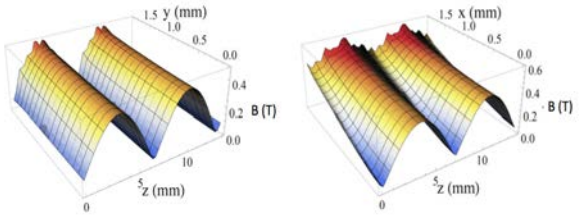

FIG. 3: Magnetic field strength profiles for $\phi_\theta = 0$

Moreover using a non-cylindrical symmetry allows us to produce a local minimum of the magnetic field strength on the molecular beam axis with a tunable non-zero offset field, thereby efficiently preventing Majorana (spin flip) transitions in the moving trap.

III. DRIVING ELECTRONICS

Traveling wave Zeeman deceleration of paramagnetic atoms and molecules requires time-dependent gradients in magnetic fields on the order of one Tesla over distances of a few millimeters. For this purpose, a high-power arbitrary waveform current generator was developed at the laboratoire Aime Cotton in Orsay, France. The generator produces bipolar currents of more than 300 A amplitude, with frequencies ranging from DC to 40 kHz. The generator is based on a full H-bridge with parallelized IGBT switches controlled by microchips to deliver arbitrary waveform bipolar currents.

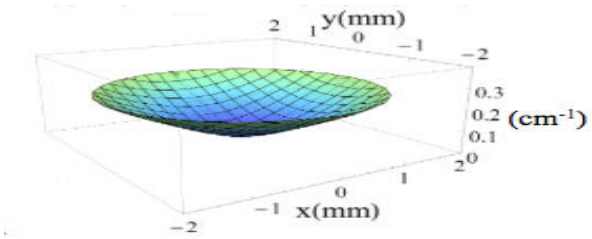

FIG. 4: Time-averaged transverse magnetic potential experienced by OH molecules

IV. OUTLOOK

OH radicals in $X^2\Pi_{3/2}$ state will be the first candidate molecule suitable for Zeeman deceleration in our experiment and we already have developed methods of production of OH molecular beam source in a specific quantum state, with characterized beam parameters. Our goal is to produce molecular beams with high particle density at any desired longitudinal velocity below initial velocity of the beam for scattering, spectroscopic and coherent experiments. In future, many molecular species could be addressed with a Zeeman decelerator, such as H_2 in $c^3\Pi_u$ state, O_2, NO, NH, CrH and so on. Based on the real trap nature of the decelerator, and effective suppressing of the Majorana transitions, this Zeeman decelerator will avoid losses of molecules at all velocities and will be ideally suited for coupling with a static trap.

[1] S. Y. T. van de Meerakker, H. L. Bethlem, N. Vanhaecke, and G. Meijer, *Manipulation and control of molecular beams*, Chemical Reviews **112**, 4828 (2012).

[2] L. D. Carr, D. DeMille, R. V. Krems, and J. Ye, *Cold and ultracold molecules: science, technology and applications*, New Journal of Physics **11**, 055049 (2009).

[3] A. Trimeche, M. N. Bera, J. P. Cromières, J. Robert, and N. Vanhaecke, *Trapping of a supersonic beam in a traveling magnetic wave*, The European Physical Journal D **65**, 263 (2011).

[4] A. W. Wiederkehr, S. D. Hogan, and F. Merkt, *Phase stability in a multistage zeeman decelerator*, Phys. Rev. A **82** (2010).

Single Trapped ^{40}Ca-Ion as Wave-Front Sensor

S. Ragg,[1] F. Lindenfelser,[1] and J. P. Home[1]

[1] *Institute of Quantum Electronics, ETH-Hönggerberg, CH-8093, Zürich, Switzerland*

Trapped ions are a promising system for realizing quantum computation. For cooling and controlling ions, high intensity laser fields are required. In this work we present a scheme to reduce optical aberrations to create a diffraction limited spot and increase the laser intensity. Optical aberrations are encoded in the phase of a laser beam ans usually measured with a wave front sensor. In this study we use the trapped ion to get an estimate of the phase.

I. INTRODUCTION

A major current goal in the control of experimental quantum systems is quantum information processing. Atomic ions trapped in radio frequency traps are a leading candidate for realizing a quantum information processor. There have been several experiments in which the required components for quantum conputation where realized both in single devices[1] and at high fidelity[2]. Laser cooling is one prerequisite for a quantum information processor based on trapped ions. The traditional scheme for cooling and controlling $^{40}Ca^{+}$ relies on the dipole transition $4^2S_{1/2} - 4^2P_{1/2}$ at a wavelength of 397 nm in combination with repumping the metastable $3^2D_{3/2}$-state back to $4^2P_{1/2}$ (see FIG. 1). The qubit is encoded in the two states $4^2S_{1/2}$ and $3^2D_{5/2}$ connected by a laser at 729 nm and readout is realized by driving the $4^2S_{1/2} - 4^2P_{1/2}$ transition checking if the ion is bright $|0\rangle$ or dark $|1\rangle$. The fact that cooling and detection is at roughly the same frequency, limits the sensitivity of fluorescence detection and qubit state readout. One can get around this by using only IR- and red lasers to cool and control the ion. This has been done for $^{40}Ca^{+3,4}$. One key component that needs to be implemented is doppler cooling on the narrow and weak dipole forbidden transition $S - D$ which requires very high intensity. In the following we will present a scheme to increase the intensity of 729 nm laser at the ion's position that is based on adaptive optics wave front correction using the ion its self at wave front sensor. This will make Doppler cooling on the $4^2S_{1/2} - 3^2D_{5/2}$ more efficient.

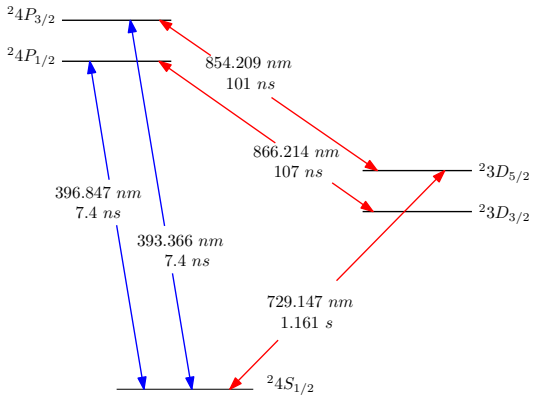

FIG. 1: Energy levels of $^{40}Ca^{+}$ with important laser transitions and lifetimes.

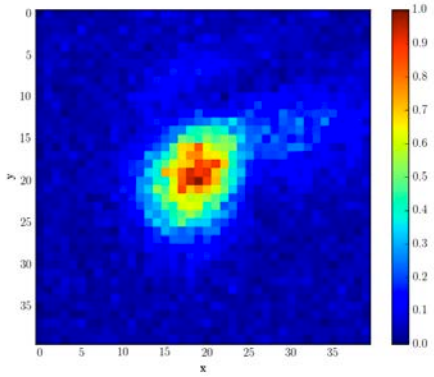

FIG. 2: Detected fluorescence as function of laser position.

II. EXPERIMENTAL SET-UP

The ion trap that we are using in this study is a homemade ion trap based on photonic crystal fibre (PCF) technologies[5]. It is driven by a RF voltage of 70V and a frequency of $2\pi \times 40$MHz providing a potential with a depth of 100meV. The trap is located inside a vacuum chamber providing ultra high vacuum. The 729 nm laser can be scanned over the ion through a piezo controlled mirror. While detecting fluorescence this allows us to image the 729 nm beam directly at the ion's position, see FIG. 2. The obtained intensity profile indicates optical aberrations. These aberrations emerge in a spatially non-uniform phase. The traditional scheme for correcting aberrations would be to use a wave front sensor that directly returns the phase of teh laser beam and a wave front modulator (phase only spatial light modulator) to correct the present aberrations. In our study we want to use the 2D-scans to estimate the aberrations and a deformable mirror[8] outside the vacuum chamber to correct them. The wave front we reconstruct from the intensity profile using a phase retrieval algorithm.

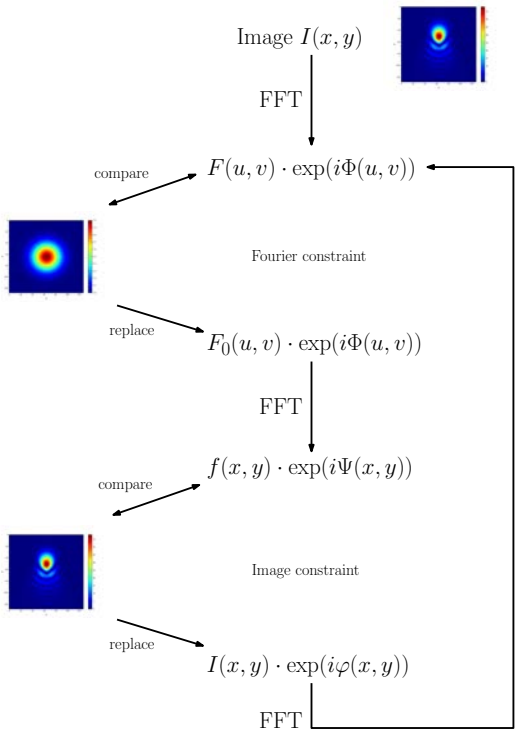

FIG. 3: Diagrammatic Gerchberg-Saxton phase retrieval algorithm cycle. FFT denotes the Fast Fourier transform.

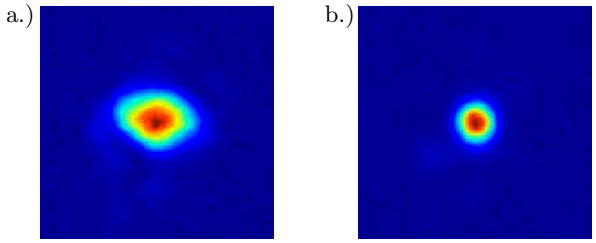

FIG. 4: Experimental test of aberration correction scheme in a simple test set-up consisting of a He-Ne-laser, a tilted lens to introduce astigmatism, the deformable mirror and a CCD-camera to image the beam. a.) before and b.) after correcting the estimated wave front.

III. PHASE RECONSTRUCTION FROM INTENSITY DATA

The problem of reconstructing the full complex amplitude from given intensity data has struggled scientists from astronomy over optical microscopy to high power laser applications. The tremendous effort that has been invested in this fields has brought out a whole collection of phase retrieval algorithms[6]. In this study we use the Gerchberg-Saxton phase retrieval algorithm that takes as inputs the intensity profile showing aberrations and in addition as a second constraint the intensity profile of a ideal Gaussian, see Fig. 3. The resulting phase represents the aberrations present in the intensity data $I(x,y)$. As a prove of principle we have applied the algorithm and the adaptive optics set-up to a simple test experiment, see Fig. 4. We where able to fully correct the designed astigmatism and decrease the spot size significantly.

IV. FUTURE APPLICATION

The presented algorithm in combination with the deformable mirror can not only be used to correct optical aberrations but also for designing and shaping a laser beam[7]. For trapped ion quantum information experiments this could be of interest to realize single ion addressing.

Acknowledgments

We like to acknowledge support from QSIT NCCR and furthermore the Swiss National Fond.

[1] J. P. Home, D. Hanneke, J. D. Jost, J. M. Amini, D. Leibfried, and D. J. Wineland, *Complete methods set for scalable ion trap quantum information processing*, Science **325**, 1227 (2009).
[2] J. Benhelm, G. Kirchmair, C. Roos, and R. Blatt, *Experimental quantum-information processing with c 43 a+ ions*, Physical Review A **77**, 062306 (2008).
[3] Z. Fei, X. Yi, C. Liang, W. Wei, W. Hao-Yu, and F. Mang, *Background-free doppler cooling of trapped ions using quadrupole transition*, Chinese Physics Letters **30**, 033701 (2013).
[4] R. J. Hendricks, J. L. Sørensen, C. Champenois, M. Knoop, and M. Drewsen, *Doppler cooling of calcium ions using a dipole-forbidden transition*, Physical Review A **77**, 021401 (2008).
[5] F. Lindenfelser, B. Keitch, D. Kienzler, D. Bykov, P. Uebel, M. Schmidt, P. S. J. Russell, and J. Home, *An ion trap built with photonic crystal fibre technology*, Review of Scientific Instruments **86**, 033107 (2015).
[6] H. Stark, *Image recovery: theory and application* (Elsevier, 1987).
[7] P. Zupancic, P. M. Preiss, R. Ma, A. Lukin, M. E. Tai, M. Rispoli, R. Islam, and M. Greiner, *Ultra-precise holographic beam shaping for microscopic quantum control*, arXiv preprint arXiv:1604.07653 (2016).
[8] Iris AO PTT111 DM segmented deformable mirror, http://www.irisao.com/product.ptt111.html

Spatial Distribution of Noise in Semiconductor Heterostructures

Matthias C. Löbl, Immo Söllner, Andreas V. Kuhlmann, Richard. J. Warburton[1]

[1]*Department of Physics, University of Basel, Klingelbergstrasse 82, CH-4056 Basel, Switzerland*

Here we propose a scheme to measure the spatial distribution of noise in semiconductor heterostructures. Spectra of charge and spin noise can be obtained by measuring the resonance fluorescence of a self-assembled InGaAs quantum dot. By measuring two independent dots at the same time, a correlation in the noise spectra can be obtained. Especially charge noise is expected to be correlated for different quantum dots due to the long range Coulomb interaction.

I. INTRODUCTION

Quantum dots in semiconductor heterostructures are promising candidates for spin qubits as well as high quality single photon sources[1,2]. However, the semiconductor environment inevitably induces noise, thus reducing the coherence of the qubit. Spin dephasing can be caused by a fluctuating Overhauser field[3,4], and also by charge noise which leads to spin dephasing via the spin-orbit interaction. While spin dephasing due to a fluctuating Overhauser field can be suppressed for hole spin qubits, charge noise remains an issue due to the strong g-factor dependence on the electric field[5,6]. For the goal of creating entanglement between quantum dots or quantum repeater networks, dephasing should be as small as possible. Understanding its origin and finding ways to reduce the noise are crucial.

A self-assembled InGaAs quantum dot in GaAs can serve as a qubit but also provides a very sensitive sensor for the noise of its own environment. It has been shown that charge and spin noise can be distinguished[7]. In these experiments noise spectra of both components have been derived from noise in resonance fluorescence of the self-assembled quantum dot. Part of the charge noise can be assigned to fluctuating charge traps close to the quantum dots[8]. However, the origin of an 1/f-component in the noise spectrum is still unknown.

Measuring noise of two quantum dots at the same time can give an insight into the spatial distribution of noise. Spin noise is expected to be local as it is mediated by the short range contact hyperfine interaction. In contrast charge noise may be spatially correlated due to the long range Coulomb interaction.

II. EXPERIMENT

In order to observe two independent quantum dots in close proximity of one another at the same time a four-port dark field microscope has been built. The self-assembled InGaAs quantum dots are embedded in a GaAs n-i-Schottky structure. In such a structure different quantum dot charge states can be initialized by applying a voltage between top- and backgate, as illustrated in Fig. 1. Quantum dots can be tuned into resonance with a laser line by using the Stark shift of the quantum dot energy levels when a bias voltage is applied. Fluctuations in resonance fluorescence intensity of self-assembled quantum dots can be used to reconstruct the noise spectra for charge and spin noise in the environment of the observed emitter[7]. For measuring resonance fluorescence the laser background is suppressed with a cross polarization technique[9]. Charge noise leads to a Stark shift in the quantum dot emission line whereas spin noise, fluctuations in the magnetic Overhauser field, leads to a varying Zeeman splitting. The difference in how the two types of noise affect the resonance fluorescence makes it possible to distinguish them and derive independent noise spectra for both[7].

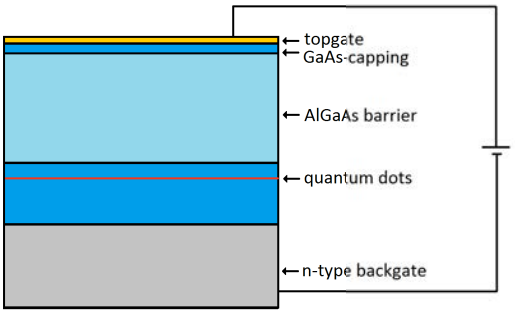

FIG. 1: A schematic heterostructure for charge tuning of quantum dots. A bias voltage between top- and backgate leads to charging of quantum dots with electrons from the backgate as well as a Stark shift of the corresponding emission lines.

The intention of our experiment is to measure a spatial distribution of charge and spin noise by investigating the correlation of the noise spectra of quantum dots at varying distances. Therefore two darkfield microscopes are combined. A 4f-setup inside the cryostat in combination with a tip-tilt mirror enables changing the x-y-position of the focus of one microscope while the other microscope is kept at a fixed position. This way one microscope can be focused at a certain quantum dot whereas the second microscope is focused at a different emitter. This setup makes it possible to probe the semiconductor environment at different spatial positions at the same time.

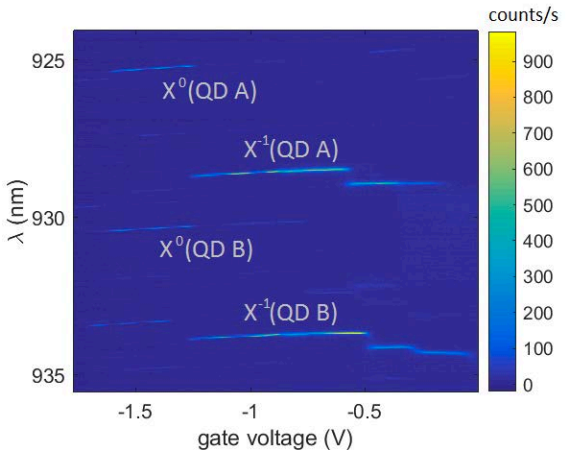

FIG. 2: Photoluminescence of two quantum dots (QDA, QDB) as function of the applied bias voltage. The distance between both dots is 500nm.

III. RESULTS

Photoluminescence is measured as function of the xy-position on the sample and two quantum dots with promising properties for noise correlation measurements are selected. Fig. 2 shows the photoluminescence for a pair of two spatially close quantum dots. The distance in the x-y-plane between the dots is 500nm such that a single charge event close to one of the dots may be seen in the resonance fluorescence signal of both dots. Photoluminescence is measured as function of the applied gate voltage. Both quantum dots show a very similar charging behaviour making it possible to measure resonance fluorescence of the same charge state of both dots at the same time. Resonance fluorescence measurements show a linewidth of 1.6μeV for quantum dot A.

IV. OUTLOOK

For both quantum dots shown in Fig. 2 the correlation of their noise spectra will be determined by simultaneous resonance fluorescence. Quantum dot pairs with different distances can be used for determination of a correlation length for different types of noise in the semiconductor device. Especially the spatial distribution of 1/f-noise will be investigated and might give a hint to its actual physical origin. The used combination of two dark-field microscopes could furthermore be used for other experiments where two positions on one device are intended to be considered at the same time. Possible applications could be photonic crystal waveguide structures as well as entanglement schemes.

[1] D. Loss and D. P. DiVincenzo, *Quantum computation with quantum dots*, Phys. Rev. A **57**, 120 (1998).

[2] A. J. Shields, *Semiconductor quantum light sources*, Nat Photonics **1**, 215 (2007).

[3] I. A. Merkulov, A. L. Efros, and M. Rosen, *Electron spin relaxation by nuclei in semiconductor quantum dots*, Phys. Rev. B **65**, 205309 (2002).

[4] A. V. Khaetskii, D. Loss, and L. Glazman, *Electron spin decoherence in quantum dots due to interaction with nuclei*, Phys. Rev. Lett. **88**, 186802 (2002).

[5] J. Pingenot, E. P. Pryor, and M. E. Flatt, *Electric-field manipulation of the landé g tensor of a hole in an ingaas-gaas self-assembled quantum dot*, Phys. Rev. B **84**, 195403 (2011).

[6] F. Klotz, V. Jovanov, J. Kierig, E. C. Clark, D. Rudolph, D. Heiss, M. Bichler, G. Abstreiter, M. S. Brandt, , et al., *Observation of an electrically tunable exciton g factor in ingaas/gaas quantum dots*, Appl. Phys. Lett. **96**, 053113 (2010).

[7] A. V. Kuhlmann, J. Houel, A. Ludwig, L. Greuter, D. Reuter, A. D. Wieck, M. Poggio, and R. J. Warburton, *Charge noise and spin noise in a semiconductor quantum device*, Nat. Phys. **9**, 570 (2013).

[8] S. Machlup, *Noise in semiconductors-spectrum of a 2-parameter random signal*, J. Appl. Phys. **25**, 341 (1954).

[9] A. V. Kuhlmann, J. Houel, D. Brunner, A. Ludwig, D. Reuter, A. D. Wieck, and R. J. Warburton, *A dark-field microscope for background-free detection of resonance fluorescence from single semiconductor quantum dots operating in a set-and-forget mode*, Rev. Sci. Instrum. **84**, 073905 (2013).

Vacuum levitated nanoparticles coupled to a silicon nitride waveguiding structure

Rozenn Diehl,[1] Erik Hebestreit,[1] Vijay Jain,[1] Rene Reimann,[1] and Lukas Novotny[1]

[1]*Photonics Laboratory, ETH-Hönggerberg, CH-8093, Zürich, Switzerland*

We study the coupling of levitated nanoparticles in vacuum to the evanescent light field of a waveguiding structure. Our aim is to couple the center-of-mass motions of two particles over long distances via the waveguide. First, we try to optimize the particle-waveguide coupling by minimizing the distance between a single, optically tweezed nanoparticle and the waveguide. The optical trap for the nanoparticle is formed by retro-reflecting a strongly focused light beam from the planar waveguide surface, thereby forming a 1D optical standing wave. Measurements of the particle center-of-mass oscillation frequencies, which depend on the particle's position in the 1D standing wave, are used to deduce the particle-waveguide distance.

I. INTRODUCTION

Spatially separated synchronized oscillators have interested scientists for a long time as they have high relevance in chemical, biological, physical and even social systems. Coupled oscillators can also be used at the nanoscale for the information sciences[1]. Controlling the coupling between two oscillators is a prerequisite for any application of such a system in information science.

Optically levitated nanoparticles in vacuum are well suited to study quantum optomechanics because, contrary to micro-fabricated devices, the system is mostly decoupled from the environment. Without clamping losses, only the remaining random forces due to collisions with air molecules and recoil heating from scattered photons disturb the particle dynamics. Because these random forces are weak, we can get oscillators with large quality factors ($Q > 10^8$). Q characterizes the damping of the system and is defined by $Q = \frac{\Omega_m}{\gamma_m}$ with Ω_m the mechanical center-of-mass frequency of the oscillator and γ_m the damping[2]. A large Q means that the system is under-damped. Experiments addressing atoms require very low pressures ($\approx 10^{-10}$ mbar) to avoid the atom being ejected from the trap by residual air molecules because their mass is much smaller than the mass of a nanoparticle. On contrast,a nanoparticle is more massive and is thus stably trapped over a broad range of pressures and experiences over 10^9 photon scattering events each second.

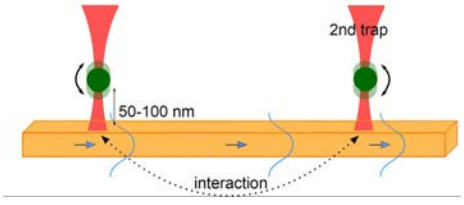

FIG. 1: Schematic of the two laser trapped particles connected through the waveguided field. The first particle influences the guided field. The perturbed guided mode interacts then with the second trapped particle, also coupled to the waveguiding structure.

A waveguiding or photonic crystal structure in the vicinity of levitated nanoparticles can be used to couple an oscillator to the electromagnetic field propagating in the waveguiding structure. This coupling is mediated by the evanescent field leaking out of the structure. With this coupling, optical trapping, transport, and manipulation of the nanoparticle can be done without external trapping lasers[3]. As recently demonstrated with trapped atoms[4], large light-matter coupling enabled by a confined field will create interesting prospects for integrated nano-optical circuits.

Our main objective is to couple the center-of-mass motion of two levitated nanoparticles through a light field that is optomechanically coupled to both oscillators and confined by a waveguiding structure (see Fig. 1).

II. EXPERIMENT : TRAPPING CLOSE TO A SURFACE

Dielectric particles can be trapped through the gradient force of a focused laser beam (λ=1064nm), which pushes the particle towards regions of higher intensity[5,6]. For sub-wavelength dielectric particles, the scattering force can be neglected and we can define a potential $U = -\frac{\alpha\prime}{\epsilon_0 c} I(r)$, where $I(r)$ is a Gaussian intensity distribution, $\alpha\prime$ the real part of the particle's polarisability, ϵ_0 the permittivity of vacuum and c the speed of light.

The particle scatters photons from the trapping laser impinging on it. A back-scattered light detection system was implemented for the particle motion detection. A schematic of the experimental setup is shown in Fig. 2. An interference measurement of the oscillator's motion is performed using the back-scattered light from the particle. The experiment is performed in a vacuum chamber under low pressures (down to 10^{-8} mbar). Thereby we enter the underdamped regime which allows the particle to oscillate with a mechanical Q-factor of up to 10^{10}. The motion of the nanoparticle is detected along all three spatial axes, and its oscillation frequencies are then deduced by applying a Fourier transform to the measured time dependent particle positions, as shown in Fig. 3(**a**,**b**).

The introduction of a dielectric surface close to the trapped nanoparticle modifies the trapping potential by

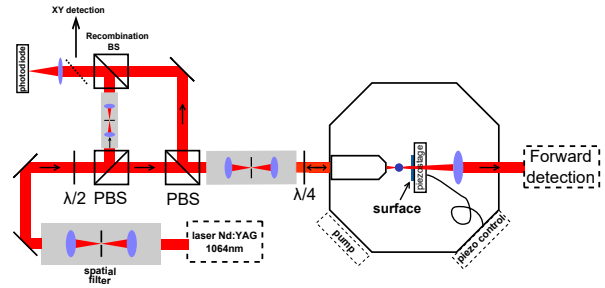

FIG. 2: Schematic of the setup, with the forward and back-scattered detection and a piezostage in the vacuum chamber to control the waveguiding structure position relative to the trapped particle.

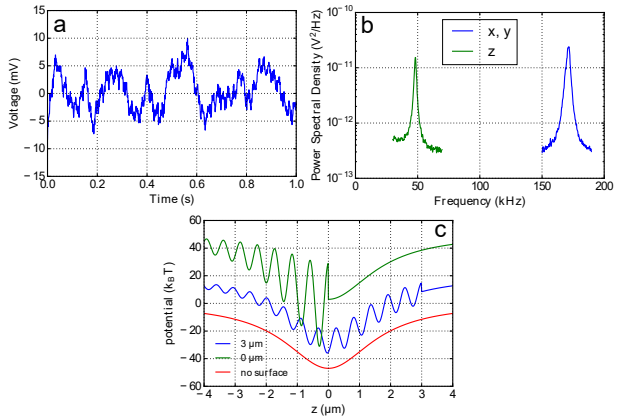

FIG. 3: (**a**) Measured position of a silica particle (diameter = 136nm) as a function of time, trapped with a Gaussian beam of power 100mW focused to a waist = $\lambda/2$, at a pressure of 1.5mbar.**b**) Fourier transform of (**a**) from which we can deduce the oscillation frequencies of the particle, along the three axes x, y and z. (**c**) Simulation of the distortion of the trapping field due to reflection of the trapping laser light onto the surface of the waveguide, for several distances surface-focus (4μm, 0μm and without surface), just considering the gradient force and offsetting the potentials for more clarity. The surface of the waveguide has a reflectivity of 33% for silicon nitride.

creating a standing wave from the reflection from the surface, as simulated in Fig. 3(**c**). The proximity of the surface also introduces near-field forces, such as van der Waals forces, which might then displace the equilibrium position of the nanoparticle. The comparable strength of optical and van der Waals forces near the surface presents a challenge as the particle must be loser than $\approx$ 100nm (evanescent field decay length) from the waveguide for efficient coupling.

III. EXPERIMENT : COUPLING THE PARTICLE MOTION TO THE WAVEGUIDING STRUCTURE

Once the particle is stably trapped close to the waveguiding structure, it can interact with the confined electromagnetic field. Based on a simple cavity optomechanical model[7], the presence of the nanoparticle in the evanescent field of the waveguiding structure induces a phase shift in the propagating field, by locally changing the effective refractive index of the mode. Using optical interferometry, we measure the phase shift due to the particle's motion. We estimate a phase shift around one degree which would require a highly stable interferometer. Therefore, we will implement an intrinsically stable, on-chip Mach-Zehnder interferometer[8] with the particle trapped close to only one arm.

IV. CONCLUSION

We presented how we try to couple the motion of a levitated nanoparticle to the electromagnetic field confined by a waveguiding structure. The proximity of the trapped particle to the waveguide would allow a coupling to the evanescent field. A phase shift of the confined field would result from this coupling, detected by an on-chip Mach-Zehnder interferometer. This light-matter coupling would then provide the first step towards the synchronization of two trapped particles through the waveguided field.

Acknowledgments

We acknowledge support from QSIT (SNF grant 51NF40-160591).

[1] J. Eisert, M. B. Plenio, S. Bose, and J. Hartley, *Towards quantum entanglement in nanoelectromechanical devices*, Physical Review Letters **93**, 1 (2004), 0311113.
[2] J. Gieseler, *Dynamics of optically levitated nanoparticles in high vacuum*, TDX (Tesis Doctorals en Xarxa) (2014).
[3] S. Mandal, X. Serey, and D. Erickson, *Nanomanipulation Using Silicon Photonic Crystal Resonators*, Nano Letters **10**, 99 (2010).
[4] J. D. Thompson, T. G. Tiecke, N. P. de Leon, J. Feist, and M. D. Lukin, *Coupling a Single Trapped Atom to a Nanoscale Optical Cavity*, Science **340**, 1202 (2013).
[5] L. Novotny and B. Hecht, *Principles of Nano-Optics* (Cambridge University Press, 2006), 2nd ed.
[6] J. Gieseler, B. Deutsch, R. Quidant, and L. Novotny, *Subkelvin Parametric Feedback Cooling of a Laser-Trapped Nanoparticle*, Physical Review Letters **109**, 103603 (2012).
[7] G. Anetsberger, O. Arcizet, Q. P. Unterreithmeier, E. M. Weig, J. P. Kotthaus, and T. J. Kippenberg, *Near-field cavity optomechanics with nanomechanical oscillators*, Nature Physics **5**, 909 (2009).
[8] W. H. P. Pernice, *Circuit Optomechanics : Concepts and Materials*, **61** (2014).